**NUREG/CR–4667, Vol. 32**
**ANL–02/33**

# Environmentally Assisted Cracking in Light Water Reactors

## Annual Report
## January—December 2001

Manuscript Completed: August 2002
Date Published: December 2002

Prepared by
O. K. Chopra, H. M. Chung, R. W. Clark, E. E. Gruber,
R. W. Hiller, W. J. Shack, W. K. Soppet, R. V. Strain

Argonne National Laboratory
9700 South Cass Avenue
Argonne, IL 60439

W. H. Cullen, Jr., and C. E. Moyer, NRC Project Managers

Prepared for
Division of Engineering Technology
Office of Nuclear Regulatory Research
U.S. Nuclear Regulatory Commission
Washington, DC 20555–0001
NRC Job Code Y6388

## Previous Documents in Series

Environmentally Assisted Cracking in Light Water Reactors Semiannual Report
April—September 1985, NUREG/CR–4667 Vol. I, ANL–86–31 (June 1986).
October 1985—March 1986, NUREG/CR–4667 Vol. II, ANL–86–37 (September 1987).
April—September 1986, NUREG/CR–4667 Vol. III, ANL–87–37 (September 1987).
October 1986—March 1987, NUREG/CR–4667 Vol. IV, ANL–87–41 (December 1987).
April—September 1987, NUREG/CR–4667 Vol. V, ANL–88–32 (June 1988).
October 1987—March 1988, NUREG/CR–4667 Vol. 6, ANL–89/10 (August 1989).
April—September 1988, NUREG/CR–4667 Vol. 7, ANL–89/40 (March 1990).
October 1988—March 1989, NUREG/CR–4667 Vol. 8, ANL–90/4 (June 1990).
April—September 1989, NUREG/CR–4667 Vol. 9, ANL–90/48 (March 1991).
October 1989—March 1990, NUREG/CR–4667 Vol. 10, ANL–91/5 (March 1991).
April—September 1990, NUREG/CR–4667 Vol. 11, ANL–91/9 (May 1991).
October 1990—March 1991, NUREG/CR–4667 Vol. 12, ANL–91/24 (August 1991).
April—September 1991, NUREG/CR–4667 Vol. 13, ANL–92/6 (March 1992).
October 1991—March 1992, NUREG/CR–4667 Vol. 14, ANL–92/30 (August 1992).
April—September 1992, NUREG/CR–4667 Vol. 15, ANL–93/2 (June 1993).
October 1992—March 1993, NUREG/CR–4667 Vol. 16, ANL–93/27 (September 1993).
April—September 1993, NUREG/CR–4667 Vol. 17, ANL–94/26 (June 1994).
October 1993—March 1994, NUREG/CR–4667 Vol. 18, ANL–95/2 (March 1995).
April—September 1994, NUREG/CR–4667 Vol. 19, ANL–95/25 (September 1995).
October 1994—March 1995, NUREG/CR–4667 Vol. 20, ANL–95/41 (January 1996).
April—December 1995, NUREG/CR–4667 Vol. 21, ANL–96/1 (July 1996).
January 1996—June 1996, NUREG/CR–4667 Vol. 22, ANL–97/9 (June 1997).
July 1996—December 1996, NUREG/CR–4667 Vol. 23, ANL–97/10 (October 1997).
January 1997—June 1997, NUREG/CR–4667 Vol. 24, ANL–98/6 (April 1998).
July 1997—December 1997, NUREG/CR–4667 Vol. 25, ANL–98/18 (September 1998).
January 1998—June 1998, NUREG/CR–4667 Vol. 26, ANL–98/30 (December 1998).
July 1998—December 1998, NUREG/CR–4667 Vol. 27, ANL–99/11 (October 1999).
January 1999—June 1999, NUREG/CR–4667 Vol. 28, ANL–00/7 (July 2000).
July 1999—December 1999, NUREG/CR–4667 Vol. 29, ANL–00/23 (November 2000).
January 2000—June 2000, NUREG/CR–4667 Vol. 30, ANL–01/08 (June 2001).
July 2000—December 2000, NUREG/CR–4667 Vol. 31, ANL–01/09 (April 2002).

# Environmentally Assisted Cracking in Light Water Reactors
# Annual Report January–December 2001

by

O. K. Chopra, H. M. Chung, R. W. Clark, E. E. Gruber,
R. W. Hiller, W. J. Shack, W. K. Soppet, R. V. Strain

## Abstract

This report summarizes work performed by Argonne National Laboratory on fatigue and environmentally assisted cracking (EAC) in light water reactors (LWRs) from January to December 2001. Topics that have been investigated include (a) environmental effects on fatigue S–N behavior of austenitic stainless steels (SSs), (b) irradiation–assisted stress corrosion cracking (IASCC) of austenitic SSs, and (c) EAC of Alloy 600.

The effects of key material and loading variables, such as strain amplitude, strain rate, temperature, dissolved oxygen (DO) level in water, and material heat treatment, on the fatigue lives of wrought and cast austenitic SSs in air and LWR environments have been evaluated. The mechanism of fatigue crack initiation in austenitic SSs in LWR environments has also been examined. The results indicate that the presence of a surface oxide film or difference in the characteristics of the oxide film has no effect on fatigue crack initiation in austenitic SSs in LWR environments.

Slow-strain-rate tensile tests and post–test fractographic analyses were conducted on several model SS alloys irradiated to ≈2 x $10^{21}$ n·$cm^{-2}$ (E > 1 MeV) (≈3 dpa) in He at 289°C in the Halden reactor. The results were used to determine the influence of alloying and impurity elements on the susceptibility of these steels to IASCC. Corrosion fatigue tests were conducted on nonirradiated austenitic SSs in high–purity water at 289°C to establish the test procedure and conditions that will be used for the tests on irradiated materials. A comprehensive irradiation experiment was initiated to obtain many tensile and disk specimens irradiated under simulated pressurized water reactor conditions at ≈325°C to 5, 10, 20, and 40 dpa.

Crack growth tests were completed on 30% cold–worked Alloy 600 in high–purity water under various environmental and loading conditions. The results are compared with data obtained earlier on several heats of Alloy 600 tested in high–DO water under several heat treatment conditions.

# Contents

## Figures

## Tables

## Executive Summary

The ASME Boiler and Pressure Vessel Code provides rules for the construction of nuclear power plant components. Appendix I to Section III of the Code specifies fatigue design curves for structural materials. However, the effects of light water reactor (LWR) coolant environments are not explicitly addressed by the Code design curves. Test data illustrate potentially significant effects of LWR environments on the fatigue resistance of carbon and low–alloy steels and austenitic stainless steels (SSs). The effects of key material and loading variables, such as strain amplitude, strain rate, temperature, dissolved oxygen (DO) level in water, and material heat treatment, on the fatigue lives of wrought and cast austenitic SSs in air and LWR environments have been evaluated. Unlike carbon and low–alloy steels, environmental effects on the fatigue life of austenitic SSs are significant in low–DO water; effects on life in high–DO water are either comparable or, for some steels, less pronounced than those in low–DO water.

The mechanism of fatigue crack initiation in austenitic SSs in LWR environments has also been examined. Crack lengths as a function of fatigue cycles have been determined in air and LWR environments. The decreases in the fatigue lives of these steels are caused primarily by the effects of environment on the growth of microstructurally small cracks and, to a lesser extent, on enhanced growth rates of mechanically small cracks. Exploratory fatigue tests were conducted to gain an understanding of the effects of surface micropits or minor differences in the surface oxide on fatigue crack initiation. The results indicate that the presence of a surface oxide film or any difference in the characteristics of the oxide film has no effect on fatigue crack initiation in austenitic SSs in LWR environments.

Hot-cell tests are being conducted to determine the susceptibility to irradiation-assisted stress corrosion cracking (IASCC) of model austenitic SSs that were irradiated in the Halden boiling heavy water reactor in simulation of irradiation-induced degradation of boiling water reactor (BWR) core internal components. Slow-strain-rate tensile tests in BWR-like water were conducted on 23 model austenitic SS alloys irradiated at 288°C in He in the Halden reactor to a fluence of $\approx 2 \times 10^{21}$ n·cm$^{-2}$ (E > 1 MeV) (≈3 dpa). Fractographic analysis by scanning electron microscopy was conducted to determine the influence of alloying and impurity elements on the susceptibility of these steels to IASCC. The results were compared with similar data obtained for 16 alloys irradiated to a fluence of $\approx 0.3 \times 10^{21}$ n·cm$^{-2}$ (≈0.43 dpa).

As fluence was increased from $\approx 0.3 \times 10^{21}$ n cm$^{-2}$ (E > 1 MeV) to $\approx 2.0 \times 10^{21}$ n cm$^{-2}$, the effect of S on the susceptibility of Type 304 and 304L SSs to IASCC became more pronounced. Heats that contain very low concentrations of S of ≤0.002 wt.% were not susceptible to IASCC, whereas heats that contain higher concentrations of S were susceptible. In spite of high S content, a model austenitic SS alloy that contained a high concentration of Cr (≈21 wt.%) and ≈3 vol.% delta ferrite exhibited excellent resistance to IASCC after irradiation up to $\approx 2.0 \times 10^{21}$ n cm$^{-2}$ (E > 1 MeV). This behavior has been explained on the basis of the effect of delta ferrite on the distribution of S in the alloy. The solubility limit of S is several times higher in delta ferrite than in the austenitic phase. Therefore, the delta ferrite globules act as trapping sites of S atoms. As a consequence, the tendency of S to concentrate on austenite grain boundaries is greatly reduced, and the susceptibility to IASCC may be suppressed in irradiated steels that contain small volume fractions of delta ferrite. However, if the volume fraction of delta ferrite is too great, embrittlement of the ferrite phase could lead to unacceptable degradation of the fracture toughness of the irradiated steel.

Fracture toughness J–R curve tests and stress corrosion crack growth tests are also being conducted on commercial heats of austenitic SSs irradiated to fluence levels up to $2 \times 10^{21}$ n $cm^{-2}$ (E >1 MeV) at 288°C. During the current reporting period, corrosion fatigue tests were conducted on nonirradiated austenitic SSs in high–purity water at 289°C to establish the test procedure and conditions that will be used for the tests on irradiated materials. Crack growth tests have been completed on 1/4–T compact tension (CT) specimens of two heats of thermally aged CF8M cast SS and a 50% cold–worked Type 316LN SS in high–purity water at 289°C. The results show good agreement with the data obtained on 1–T CT specimens.

The resistance of Ni alloys to EAC in simulated LWR environments is being evaluated. Existing crack growth rate (CGR) data for Alloys 600 and 690 under cyclic loads have been analyzed to establish the effects of alloy chemistry, material heat treatment, cold work, temperature, load ratio R, stress intensity K, and DO level. To obtain a qualitative understanding of the degree and range of conditions that are necessary for significant environmental enhancement in growth rates, the experimental CGRs in high–temperature, high–purity water are compared with CGRs that would be expected in air under the same mechanical loading conditions. The fatigue CGRs of Alloy 600 are enhanced in high–DO water; the environmental enhancement of growth rates does not appear to depend on either the C content or heat treatment of the material. Also, in high–DO water, the CGRs at 320°C are comparable to those at 289°C. In low–DO water, environmental enhancement of CGRs of Alloy 600 seems to depend on material conditions such as yield strength and grain boundary coverage of carbides. The data suggest that materials with high yield strength and/or low grain boundary coverage of carbides exhibit enhanced CGRs. Correlations have been developed for estimating the enhancement of CGRs of Alloy 600 in LWR environments relative to the CGRs in air under the same loading conditions.

During the current reporting period, CGR tests were completed on 30% CW Alloy 600 (Heat NX131031) specimen in high–purity water under various environmental and loading conditions. The growth rates from these tests are compared with data obtained earlier on several heats of Alloy 600 tested in high–DO water under several heat treatment conditions. The environmental enhancement of CGRs of 30% CW Alloy 600 in high–DO water appears to be a factor of 2–3 lower than that observed earlier for the mill–annealed material. Part of this difference may be due to a change in the CGRs in air for the CW material.

## Acknowledgments

The authors thank T. M. Galvin, R. W. Clark, and J. Tezak for their contributions to the experimental effort. This work is sponsored by the Office of Nuclear Regulatory Research, U.S. Nuclear Regulatory Commission, under Job Code W6610; Program Manager: William H. Cullen, Jr.; Tasks 2 and 3 Manager: Carol E. Moyer.

# 1 Introduction

Since 1967, the Nuclear Regulatory Commission (NRC) and its predecessor the Atomic Energy Commission (AEC) have conducted research programs that address aging of reactor components. The results of this research have been used to evaluate and establish regulatory guidelines to ensure acceptable levels of reliability for light water reactor (LWR) components. The products of this program, i.e., technical reports, methodologies for evaluating licensee submittals, and other inputs to the regulatory process, have led to the resolution of regulatory issues, as well as the development, validation, and improvement of regulations and regulatory guides. The research on the effects of the environment on component cracking, was initiated in response to the determination that environmental effects were critical to several important cracking phenomena in LWR components. A major research program at Argonne National Laboratory (ANL) was initiated in 1979 to address pipe cracking problems in boiling water reactors (BWRs). Since that time, in response to needs for additional research to support the Office of Nuclear Reactor Regulation (NRR) in dealing with developing cracking problems in aging reactors, the focus of the project has shifted to address other problems in environmental cracking of LWR components. In recent years this activity has been supplemented by NRC participation in the Cooperative Irradiation Assisted Stress Corrosion Cracking Research (CIR) Program, a proprietary activity in which groups in several countries contribute money that is used to support research on irradiation–assisted stress corrosion cracking (IASCC) problems of common interest.

This project consists of several tasks with differing objectives, so the objectives are best described on a task–by–task basis:

Task 1: Environmental Effects on Fatigue Crack Initiation.

The objective of this task is to provide information on such topics as fatigue crack initiation in stainless steel (SS), and the synergistic effects of surface finish or loading sequence and environment on fatigue life. A comprehensive evaluation of SS fatigue test specimens will be performed to explain why environmental effects are more pronounced in low–dissolved oxygen (DO) than high–DO water. The contractor will review and evaluate issues related to environmental effects on fatigue as required by the NRC, and participate in ASME Code committees to incorporate the effects of LWR environments in fatigue life analyses.

Task 2: Evaluation of the Causes and Mechanisms of IASCC in BWRs.

This task will evaluate the susceptibility of austenitic SSs and their welds to IASCC as a function of fluence level, water chemistry, material chemistry, welding process, and fabrication history. It will provide data and technical support required for determination of inspection interval, to help NRC address various issues that arise in license renewal or other licensee submittals. Crack growth rate (CGR) tests and slow strain rate tests (SSRTs) will be conducted on high–fluence model SSs from Halden Phase–I irradiations (carried out under NRC FIN W6610) to investigate the effects of material chemistry and irradiation level on the susceptibility of SSs to IASCC. CGR tests will be conducted on submerged arc (SA) and shielded metal arc (SMA) welds of Types 304 and 304L SS irradiated to $1.2 \times 10^{21}$ n/cm$^2$ in the Halden reactor to

establish the effects of fluence level, material chemistry, and welding process on IASCC. Also, SSRTs and CGR tests will be carried out on grain boundary optimized (GBO) model SS alloys to study the effect of grain boundary geometry on IASCC and investigate the prospect of using grain boundary optimization as a mitigative measure. Models and codes developed under CIR and from industry sources will be benchmarked and used in conjunction with this work.

Industry developed crack growth models will be analyzed and assessed. Also, the effectiveness of mitigative water chemistry measures, e.g., hydrogen water chemistry or noble metal additions, will be assessed. Much of this assessment will depend on data provided by industry, data available in the literature, and data developed as part of this task. However, for CGR models for irradiated materials, it is anticipated that relatively few data will be available because of the expense and difficulty of testing. Additional testing on nonirradiated materials will be performed to provide "limiting cases" against which the models can be tested. These tests will seek to determine the effects of Cr level in the steel and cold work on CGRs in austenitic SSs in LWR environments. This will be accomplished by procuring material and fabricating and testing compact–tension (CT) specimens from model SS alloys with lower Cr content and cold–worked (CW) Types 304L and 304 SS.

Task 3: Evaluation of Causes and Mechanisms of IASCC of Austenitic SS in PWRs.

The task will focus on (a) evaluation of the effects of very high fluence on CGRs, (b) neutron irradiation embrittlement, e.g., loss of fracture toughness, and (c) void swelling behavior in austenitic SSs. Tests will be conducted on material procured from EBR–II reactor hex cans or irradiated in the BOR–60 reactor in Russia.

Task 4: Cracking of Nickel Alloys and Weldments.

The objective of this task is to provide the NRC with technical data on the implications of cracks in Ni-alloy components and weldments for residual life, inspection, and repair. Many reactor vessel internal components are made of alloys such as Alloy 600, Alloy X750, and Alloy 182, which are susceptible to intergranular stress corrosion cracking (IGSCC). The causes and mechanisms of this cracking and the implications of microstructure, microchemistry, and surface finish for component life are also not understood, and thus lead to greater uncertainty in licensee submissions that address issues such as damage accumulation and inspection intervals. The NRC research program will address these issues and provide data required to support staff assessment of industry CGR models, and potential detection and mitigation measures.

Task 5: Investigation of Other Modes of Degradation in High–Fluence Materials in PWR Environments.

Research at Saclay has shown that gas generation in high fluence materials can produce unexpected changes in material behavior. Because studies on materials at high fluences and at temperatures of interest to LWRs are relatively limited, it is possible that additional degradation phenomena beyond those studied in detail in the other tasks could occur. The work in this task would seek to study, in cooperation with staff at Saclay and others in CIR, the potential for other degradation phenomena.

# 2 Environmental Effects on Fatigue Crack Initiation in Austenitic Stainless Steels (O. K. Chopra)

## 2.1 Introduction

Cyclic loadings on a structural component occur because of changes in mechanical and thermal loadings as the system goes from one load set (e.g., pressure, temperature, moment, and force loading) to any other load set. For each load set, an individual fatigue usage factor is determined by the ratio of the number of cycles anticipated during the lifetime of the component to the allowable cycles. Figures I–9.1 through I–9.6 of Appendix I to Section III of the ASME Boiler and Pressure Vessel Code specify design fatigue curves that define the allowable number of cycles as a function of applied stress amplitude. The cumulative usage factor (CUF) is the sum of the individual usage factors, and ASME Code Section III requires that the CUF at each location must not exceed 1.

The ASME Code fatigue design curves, given in Appendix I of Section III, are based on strain–controlled tests of small polished specimens at room temperature in air. The design curves have been developed from the best–fit curves to the experimental fatigue–strain–vs.–life (ε–N) data that are expressed in terms of the Langer equation[1] of the form

$$\varepsilon_a = B(N)^{-b} + A, \quad (1)$$

where $\varepsilon_a$ is the applied strain amplitude, N is the fatigue life, and A, B, and b are parameters of the model. Equation 1 may be written in terms of stress amplitude $S_a$ instead of $\varepsilon_a$, in which case stress amplitude is the product of $\varepsilon_a$ and elastic modulus E, i.e., $S_a = E\,\varepsilon_a$. The fatigue design curves were developed from the best–fit experimental curves by first adjusting for the effects of mean stress on fatigue life and then reducing the fatigue life at each point on the adjusted curve by a factor of 2 on strain or 20 on cycles. However, because the Code mean fatigue curve for austenitic SSs does not accurately represent the available experimental data,[2,3] the current Code design curve for SSs includes a reduction of only ≈1.5 and 15 from the mean curve for the SS data, not the 2 and 20 originally intended.

The factors of 2 and 20 are not safety margins but rather conversion factors that must be applied to the experimental data to obtain reasonable estimates of the lives of actual reactor components. Although the Section III criteria document[4] states that these factors were intended to cover such effects as environment, size, and scatter of data, Subsection NB–3121 of Section III of the Code explicitly notes that the data used to develop the fatigue design curves in Section III did not include tests subjected to corrosive environments that might accelerate fatigue failure. Article B–2131 in Appendix B to Section III states that the owner's design specifications should provide information about any reduction to fatigue design curves that has been necessitated by environmental conditions.

Existing fatigue ε–N data illustrate potentially significant effects of LWR coolant environments on the fatigue resistance of carbon and low–alloy steels,[5-11] as well as of austenitic SS[3,12–18] (Fig. 1). The key parameters that influence fatigue life in LWR environments are temperature; DO level in water; strain rate; strain (or stress) amplitude; and, for carbon and low–alloy steels, S content in the steel. Under certain environmental and loading conditions, fatigue lives of carbon steels can be a factor of 70 lower in coolant environments than in air.[7–9]

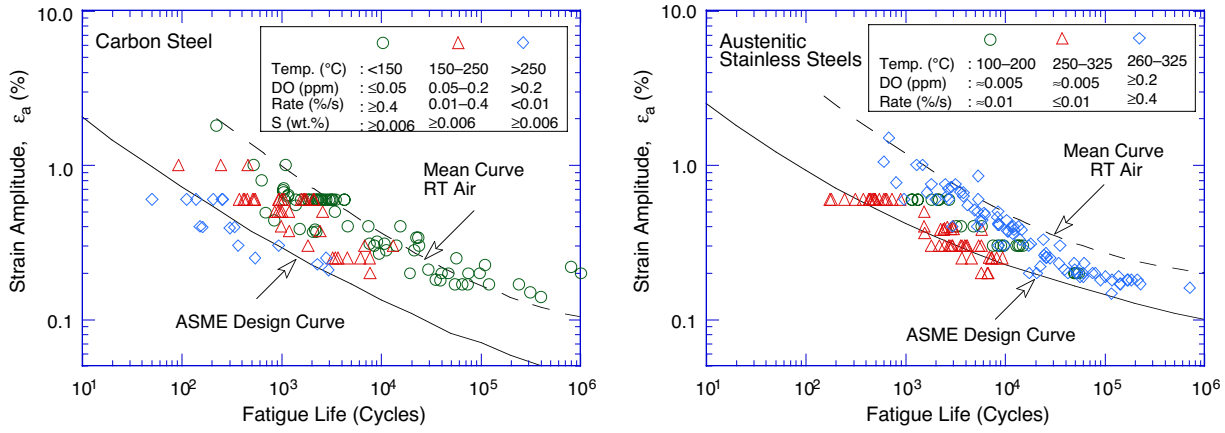


(a) (b)

Figure 1. ε–N data for (a) carbon steels and (b) austenitic stainless steels in water; RT = room temperature.

For carbon and low–alloy steels, environmental effects on fatigue life are significant in high–DO water (>0.04 ppm DO) and only moderate (less than a factor of 2 decrease in life) in low–DO water. The reduction in fatigue life of carbon and low–alloy steels in LWR environments has been explained by the slip oxidation/dissolution mechanism for crack advance.[19] The requirements for the model are that a strain increment occur to rupture the protective surface oxide film and thereby expose the underlying matrix to the environment; once the passive oxide film is ruptured, crack extension is controlled by dissolution of freshly exposed surfaces and their oxidation characteristics. Unlike the case of carbon and low–alloy steels, environmental effects on the fatigue lives of austenitic SSs are significant in low–DO (i.e., <0.01 ppm DO) water; in high–DO water, environmental effects appear to be either comparable[15,16] or, in some cases, smaller[3] than those in low–DO water. These results are difficult to reconcile in terms of the slip oxidation/dissolution model.

This report examines the mechanism of fatigue crack initiation in austenitic SSs in LWR coolant environments. The effects of key material and loading variables on the fatigue lives of wrought and cast austenitic SSs in air and LWR environments have been evaluated. The influence of reactor coolant environments on the formation and growth of fatigue cracks in polished smooth specimens is discussed. Crack length as a function of fatigue cycles was determined in water by block loading that leaves beach marks on the fracture surface. Fatigue test specimens were examined to characterize the fracture morphology. Exploratory fatigue tests were conducted on austenitic SS specimens that were preexposed to either low– or high–DO water and then tested in air or water environments in an effort to understand the effects of surface micropits or minor differences in the surface oxide on fatigue crack initiation.

## 2.2 Fatigue ε–N Behavior

### 2.2.1 Air Environment

The existing fatigue data indicate that, in air, the fatigue lives of Types 304 and 316 SS are comparable; lives of Type 316NG are slightly higher at high strain amplitudes.[3,12,13] The fatigue ε–N behavior of cast CF-8 and CF–8M SS is similar to that of wrought austenitic SSs.

Also, the fatigue life of austenitic SSs in air is independent of temperature in the range from room temperature to 427°C.[3,20] Although the effect of strain rate on fatigue life seems to be significant at temperatures above 400°C, variation in strain rate in the range of 0.4–0.008%/s has no effect on the fatigue lives of SSs at temperatures up to 400°C.[21] The cyclic stress–vs.–strain curves for Types 304, 316, and 316NG SS at room temperature and 288°C have been presented elsewhere.[3] During cyclic loading, austenitic SSs exhibit rapid hardening within the first 50–100 cycles; the extent of hardening increases with increasing strain amplitude, and decreasing temperature and strain rate.[3,21] The initial hardening is followed by softening and a saturation stage at high temperatures, e.g., 288°C, and by continuous softening at room temperature.

### 2.2.2 LWR Environments

The fatigue lives of austenitic SSs are decreased in LWR environments; the reduction in life depends on strain amplitude, strain rate, temperature, and DO level in the water.[3,12–18] The effects of LWR environments on fatigue lives of wrought materials are comparable for Types 304, 316, and 316NG SS, whereas the effects on cast materials differ somewhat. The critical parameters that influence fatigue life and the threshold values that are required for environmental effects to be significant are summarized below.

Strain Amplitude: A minimum threshold strain is required for an environmentally assisted decrease in fatigue lives of SSs. The threshold strain is the minimum total applied strain above which environmental effects are significant. Even within a given loading cycle, environmental effects are significant at strain levels greater than the threshold value. The threshold strain appears to be independent of material type (weld or base metal) and temperature in the range of 250–325°C, but it tends to decrease as the total applied strain is decreased.[17] Also, the threshold strain does not correspond to rupture strain of the surface oxide film. The fatigue life of Type 304 SS tested in low–DO water at 288°C with a 2–min hold period at zero strain during the tensile–rise portion of the cycle was identical with that of tests conducted under similar loading conditions but without the hold period.[22] If this threshold strain corresponds to the rupture strain of the surface oxide film, a hold period at the middle of each cycle should allow repassivation of the oxide film, and environmental effects on fatigue life should diminish.

Loading Cycle: Environmental effects on fatigue life occur primarily during the tensile–loading cycle and at strain levels greater than the threshold value. Consequently, loading and environmental conditions, e.g., strain rate, temperature, and DO level, during the tensile–loading cycle are important for environmentally assisted reduction of fatigue lives of these steels. Limited data indicate that hold periods during peak tensile or compressive strain have no effect on the fatigue life of austenitic SSs in high–DO water. The fatigue lives of Type 304 SS tested with a trapezoidal waveform[23] are comparable to those tested with a triangular waveform.[3,18]

Strain Rate: Fatigue life decreases with decreasing strain rate. In low–DO pressurized water reactor (PWR) environments, fatigue life decreases logarithmically with decreasing strain rate below ≈0.4%/s; the effect of environment on life saturates at ≈0.0004%/s (Fig. 2).[3,12–18] A decrease in strain rate from 0.4 to 0.0004%/s decreases the fatigue life of austenitic SSs by a factor of ≈10. For some SSs, the effect of strain rate may be less pronounced in high–DO water than in low–DO water. For cast SSs, the effect of strain rate on life is the same in low– and high–DO water and comparable to that observed for the wrought SSs in low–DO water.[15,16]

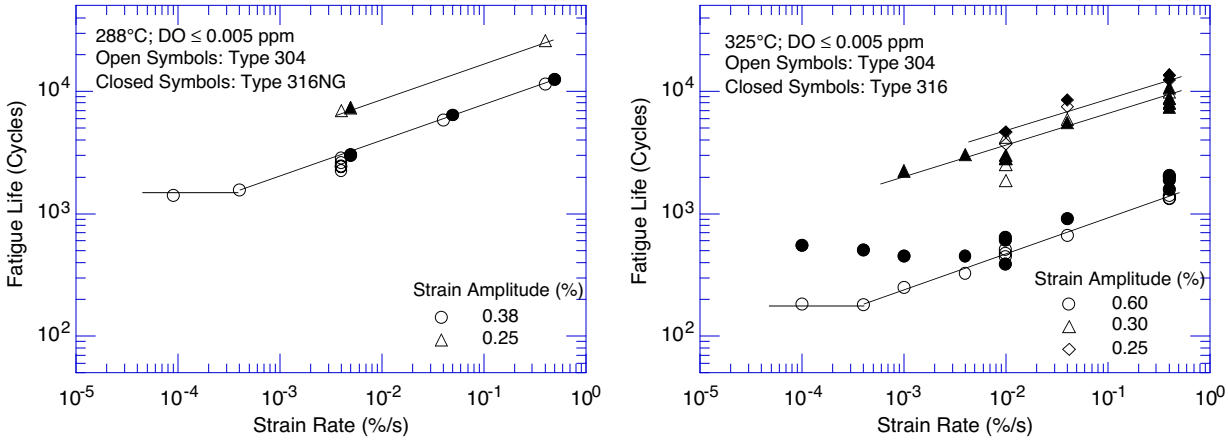


Figure 2. Dependence of fatigue life of austenitic stainless steels on strain rate in low–DO water (Refs. 3,13,15–18).

Dissolved Oxygen in Water: The fatigue lives of austenitic SSs are decreased significantly in low–DO (i.e., <0.01 ppm DO) water; the decrease in life is greater at low strain rates and high temperatures.[3,12–18] Environmental effects on the fatigue lives of these steels in high–DO water are not well known; the magnitude of environmental effects in high–DO water may be influenced by the composition or heat treatment of the steel. The existing fatigue ε–N data indicate that the fatigue lives of cast SSs are approximately the same in low– and high–DO water and comparable to those observed for wrought SSs in low–DO water.[3,15,16,18] The fatigue lives of wrought SSs in high–DO water are comparable[15,16] for some steels and higher[3] for other steels than those in low–DO water.

Only moderate environmental effects (less than a factor of 2 decrease in life) were observed for a heat of Type 304 SS when conductivity of the water was maintained at <0.1 μS/cm and the electrochemical potential (ECP) of the steel was above 150 mV (Fig. 3).[22] During a laboratory test, the time to reach these stable environmental conditions depends on test parameters such as the autoclave volume, flow rate, etc. In the ANL test facility, fatigue tests on austenitic SSs in high–DO water required a soaking period of 5–6 days for the ECP of the steel to stabilize. The steel ECP increased from zero or a negative value to above 150 mV during this period. The fatigue lives of Type 304 SS specimens soaked for ≈5 days in high–DO water before testing in high–DO water at 289°C and ≈0.38 and 0.25% strain amplitude, are plotted as a function of strain rate in Fig. 3a. Similar results for Type 316NG specimens that were soaked for only one day before testing are shown in Fig. 3b. For Type 304 SS, fatigue life decreases linearly with decreasing strain rate in low–DO water, whereas in high–DO water, strain rate has no effect on fatigue life. For example, the fatigue life at ≈0.38% strain amplitude and 0.0004%/s strain rate is ≈1500 cycles in low–DO water and >7300 cycles in high–DO water. At all strain rates, the fatigue life of Type 304 SS is 30% lower in high–DO water than in air. However, the results obtained at MHI, Japan, on Types 304 and 316 SS show a different behavior; environmental effects are observed to be the same in high– and low–DO water.[15,16] As discussed later in this section, the composition or heat treatment of the steel have an important impact on the magnitude of environmental effects in high–DO water; additional tests are in progress to establish the fatigue life of SSs in high–DO environments.

For 316NG, some effect of strain rate is observed in high–DO water, although it is smaller than that in low–DO water (Fig. 3b). The differing strain rate effect for the two steels has been

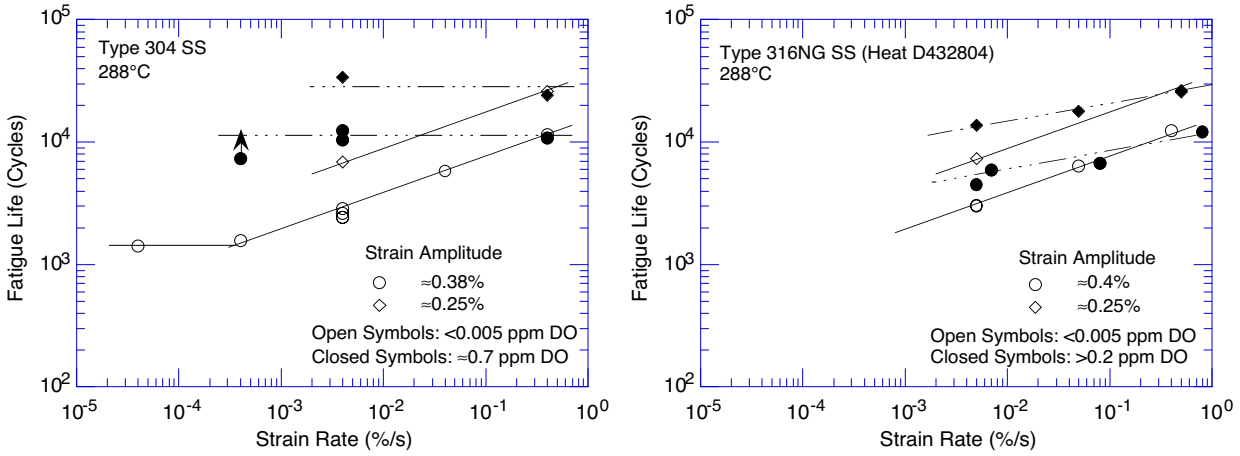


Figure 3. Dependence of fatigue life of Types (a) 304 and (b) 316NG stainless steel on strain rate in high– and low–DO water at 288°C (Refs. 3,22).

explained on the basis of the shorter soak period for Type 316NG specimens, e.g., 24 h for Type 316NG and ≈120 h for Type 304 SS.[22] Environmental conditions may not have been stable for the tests on Type 316NG in high–DO water.

The effect of the conductivity of water and the ECP of the steel on the fatigue life of austenitic SSs is shown in Fig. 4. Environmental effects are significant for the specimens that were soaked for 24 h. For these tests, the ECP of steel was very low initially and increased during the test. Also, in high–DO water, fatigue life is decreased by a factor of ≈2 when conductivity of water is increased from ≈0.07 to 0.4 μS/cm.

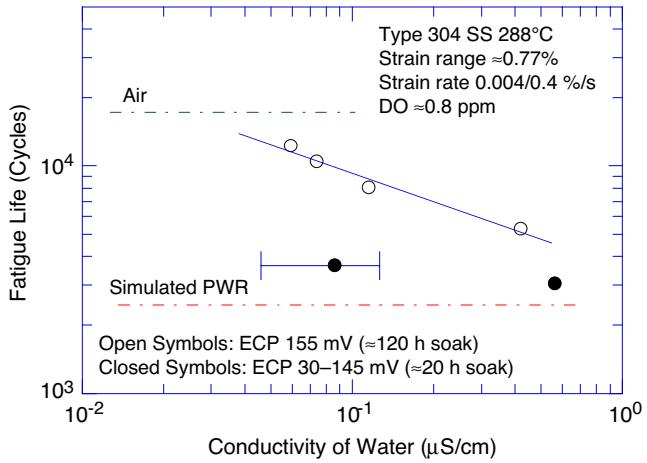


Figure 4.
Effects of conductivity of water and soaking period on fatigue life of Type 304 SS in high–DO water (Ref. 22).

The effects of water chemistry and soaking period on the fatigue life of austenitic SSs in low–DO water have also been investigated. In low–DO water, the following have no effect on the fatigue life of Type 304 SS: the addition of Li and B, low conductivity, soak period of ≈5 days before the test, and dissolved H.

These results suggest that the existing fatigue ε–N data on austenitic SSs in high–DO environments should be reevaluated; some of the data may have been obtained under varying environmental conditions. For example, the ECP of the steel may have been negative at the

start of the test, and low–DO environment or negative ECP is known to decrease fatigue life of austenitic SSs. Also, the composition or heat treatment of the steel may have an important impact on the magnitude of environmental effects in high–DO environments. Additional data are needed to improve our insight into the effect of DO content on the fatigue life of austenitic SSs in LWR environments.

Temperature: At strain rates above the threshold value of 0.4%/s, fatigue life decreases linearly with temperature above 150°C and up to 325°C.[18,24] Only a moderate decrease in life is observed in water at temperatures below the threshold value of 150°C.

Sensitization Anneal: In low–DO water, a sensitization anneal has no effect on the fatigue life of Types 304 and 316 SS, whereas, in high–DO water, environmental effects are enhanced in sensitized steel (Fig. 5). For example, the fatigue life of sensitized steel is a factor of ≈2 lower than that of solution–annealed material in high–DO water.[15,16] Sensitization has little or no effect on the fatigue life of Type 316NG SS in low– and high–DO water.

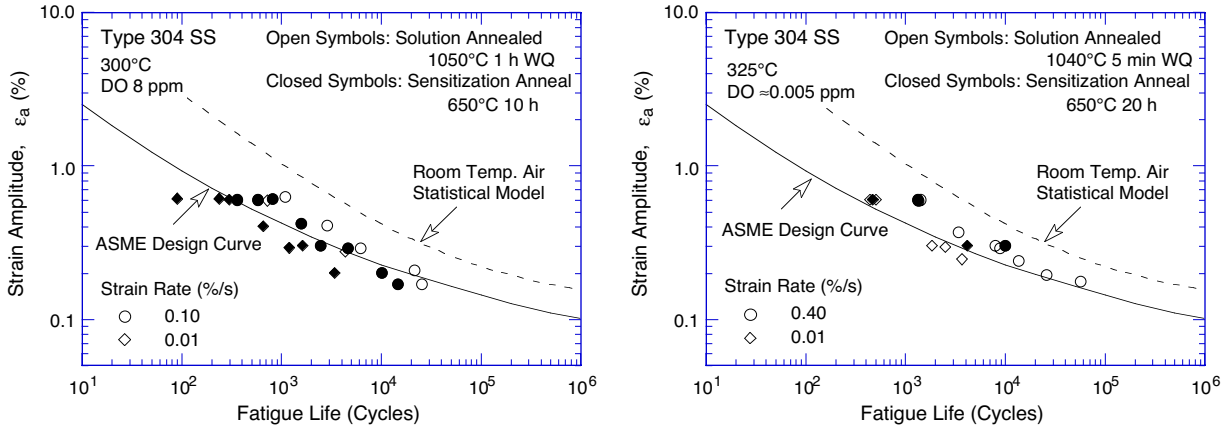


Figure 5. Effect of sensitization anneal on fatigue lives of Type 304 stainless steel in (a) high– and (b) low–DO water (Refs. 15,16).

Flow Rate: The effects of flow rate on the fatigue life of austenitic SSs have not been investigated. The data for carbon steels indicate that, under the environmental conditions typical of operating BWRs, environmental effects on the fatigue life of carbon steels are a factor of ≈2 lower at high flow rates (7 m/s) than at 0.3 m/s or lower.[25,26] Because the mechanism of fatigue crack initiation in LWR environments appears to be different in austenitic SSs than in carbon steels, the effect of flow rate on fatigue life may also be different.

## 2.3 Mechanism of Fatigue Crack Initiation

### 2.3.1 Formation of Engineering–Size Cracks

The formation of surface cracks and their growth to an "engineering" size (3 mm deep) constitute the material's fatigue life, which is represented by the fatigue ε–N curves. Fatigue life has conventionally been divided into two stages: initiation, expressed as the cycles required to form microcracks on the surface; and propagation, expressed as cycles required to propagate the surface cracks to engineering size. During cyclic loading of smooth test specimens, surface

cracks 10 μm or longer form quite early in life (i.e., <10% of life) at surface irregularities or discontinuities either already in existence or produced by slip bands, grain boundaries, second–phase particles, etc.[7,27–31] Consequently, fatigue life may be considered to be composed entirely of propagation of cracks from 10 to 3000 μm long.[32]

A schematic illustration of the two stages, i.e., initiation and propagation, of fatigue life is shown in Fig. 6. The initiation stage involves growth of microstructurally small cracks (MSCs), characterized by decelerating crack growth (Region AB in Fig. 6a). The propagation stage involves growth of mechanically small cracks, characterized by accelerating crack growth (Region BC in Fig. 6a). The growth of MSCs is very sensitive to microstructure.[28,29] Fatigue cracks greater than the critical length of MSCs show little or no influence of microstructure, and are termed mechanically small cracks. Mechanically small cracks correspond to Stage II (tensile) cracks, which are characterized by striated crack growth, with a fracture surface normal to the maximum principal stress.

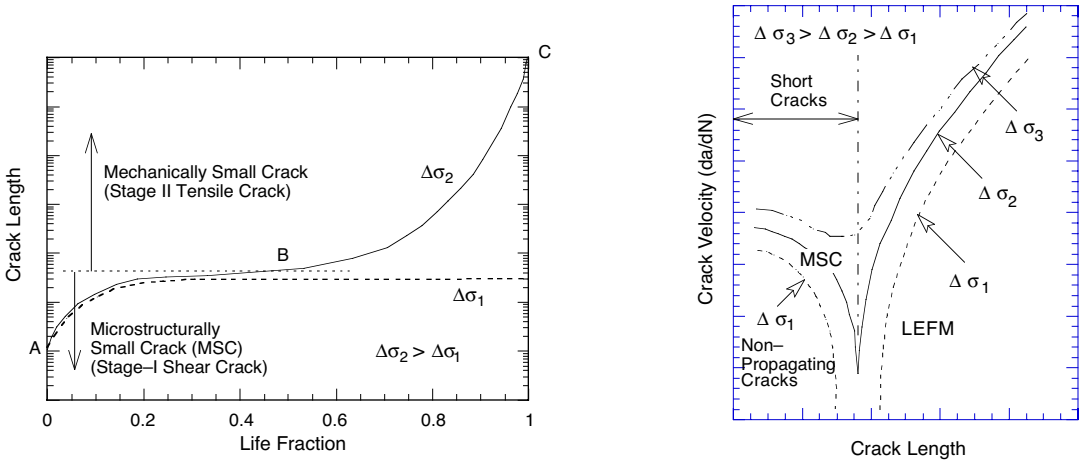


Figure 6. Schematic illustration of (a) growth of short cracks in smooth specimens as a function of fatigue life fraction and (b) crack velocity as a function of crack length. LEFM = linear elastic fracture mechanics; MSC = microstructurally small cracks.

Once a microcrack forms on the surface, it continues to grow along its slip plane as a Mode II (shear) crack in Stage I growth (orientation of the crack is usually at 45° to the stress axis). At low strain amplitudes, a Stage I crack may extend across several grain diameters before the increasing stress intensity of the crack promotes slip on systems other than the primary slip system. A dislocation cell structure normally forms at the crack tip. Because slip is no longer confined to planes at 45° to the stress axis, the crack begins to propagate as a Mode I (tensile) crack, normal to the stress axis in Stage II growth. At high strain amplitudes, the stress intensity is quite large and the crack propagates entirely by the Stage II process. Stage II continues until the crack reaches engineering size (≈3 mm deep).

Various criteria have been used to define the crack length for transition from MSC to mechanically small crack; they may be related to the plastic zone size, crack–length–vs.–fatigue–life curve, Weibull distribution of the cumulative probability of fracture, stress–range–vs.–crack–length curve, or grain size. These criteria, summarized in

Ref. 22, indicate that the transition crack length is a function of applied stress and the microstructure of the material; actual values may range from 150 to 250 μm.

At low stress levels, e.g., $\Delta\sigma_1$ in Fig. 6, the transition from MSC growth to accelerating crack growth does not occur. This circumstance represents the fatigue limit for the smooth specimen. Although cracks can form below the fatigue limit, they can grow to engineering size only at stresses greater than the fatigue limit. However, cracks larger than the transition crack length, either preexisting, e.g., defects in welded samples, or those created by growth of MSCs at high stresses, can grow at stress levels below the fatigue limit, and their growth can be estimated from linear–elastic or elastic–plastic fracture mechanics. To accurately estimate the fatigue lives of structural materials it is important that both crack initiation and crack propagation be characterized and understood.

### 2.3.2 Growth Rates of Small Cracks in LWR Environments

The reduction in fatigue life of structural materials in LWR coolant environments has often been attributed to easy crack formation. Measurements of crack frequency, i.e., number of cracks per unit length of the specimen gauge surface, indicate that, under similar loading conditions, the number of cracks in specimens tested in air and low–DO water are comparable, although fatigue life is significantly lower in low–DO water. For Type 316NG SS tested at 288°C, ≈0.75% strain range, and 0.005%/s strain rate, the number of cracks (longer than 20 μm) along a 7–mm gauge length was 16, 14, and 8 in air, simulated PWR (low–DO) water, and high–DO water, respectively.[12] If reduction in life is caused by easy crack formation, specimens tested in water should contain more cracks. Also, as discussed above, several studies indicate that fatigue cracks that are 10 μm long or longer form quite early in life, i.e., <10% of life. Therefore, at most, easy crack formation can decrease fatigue life by 10%. The reduction in fatigue life in LWR coolant environments most likely arises from an increase in CGRs during either the initiation stage (i.e., growth of MSCs), and/or the propagation stage (i.e., growth of mechanically small cracks).

Studies on crack initiation in smooth fatigue specimens indicate that, although the growth rates of mechanically small cracks are greater in water than in air, the decrease in fatigue lives of austenitic SSs in LWR environments is caused predominantly by the effects of the environment on the growth of MSCs.[33] Figure 7 shows the depth of the largest crack observed in austenitic SSs in air and water environments as a function of fatigue cycles. In the figure, the crack length for the test in air at 288°C and 0.75% strain range was measured only near the end of the test. The data obtained by Orbtlik et al.[30] on Type 316L SS in air at 25°C and ≈0.2% strain range were used to estimate the crack growth in air at 0.75% strain range. Studies on carbon and low-alloy steels[28,29,34] indicate that the fatigue crack size at various life fractions is independent of strain range, strain rate, and temperature; consequently, the depth of the largest crack at various life fractions is approximately the same at the 0.75 and 0.2% strain ranges. The curve for the test in air at 0.75% (shown as a dash line in Fig. 7) was calculated from the best-fit equation of the experimental data for Type 316L SS at the 0.2% strain range; the estimated crack lengths at the 0.75% strain range show very good agreement with the measured values. The results show that, at the same number of cycles, the crack length is longer in low–DO water than in air, e.g., after 1500 cycles the crack length in air, high-DO (BWR) water, and low–DO (PWR) water is ≈40, 300, and 1100 μm, respectively (see Fig. 7). The growth of cracks during the initiation stage, i.e., growth of MSCs, is enhanced in water; fatigue cycles needed to form a 500–μm crack are a factor of ≈12 lower in low–DO water

than in air. Figure 7 shows that the number of cycles required to produce a 500–μm crack is 800, 3000, and 9000 in low–DO (PWR), high-DO (BWR), and air environments, respectively; thus the number of cycles is more than a factor of 10 lower in low–DO water than in air.

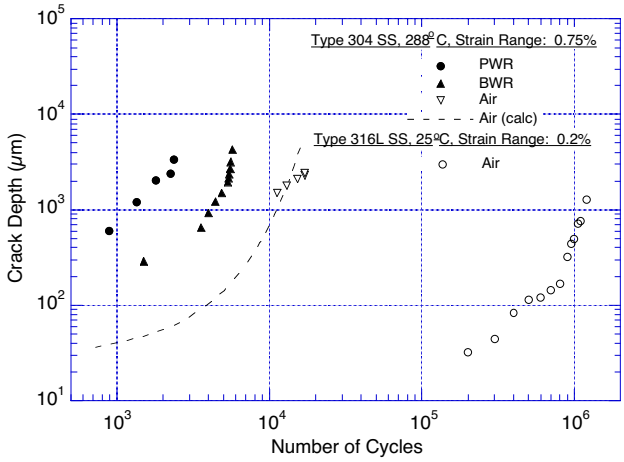


Figure 7.
Depth of largest crack plotted as a function of fatigue cycles for austenitic stainless steels in air and water (Refs. 30,33).

The CGRs during the propagation stage, i.e., growth of mechanically small cracks, in air and water environments are plotted as a function of crack length in Fig. 8; they were calculated from the best–fit of the data in Fig. 7. The CGRs in high–DO water for the specimen with a 24–h soak period (closed circles in Fig. 8) were determined from measurements of fatigue striations on the fracture surface. The CGRs are a factor of 2–6 higher in water than in air. Growth rates in PWR water or high–DO water with a 24–h soak period are higher than those in high–DO water with a 120–h soak period. At a crack length of ≈1000 μm, the CGRs in air, high–DO water, and low–DO PWR environment are 0.30, 0.64, and 1.05 μm/cycle, respectively. For the 0.75% strain range and 0.004%/s strain rate, these values correspond to growth rates of ≈1.6 x $10^{-9}$, 3.4 x $10^{-9}$, and 5.6 x $10^{-9}$ m/s in air, high–DO water, and low–DO water, respectively. Growth rates are a factor of 3.5 greater in low–DO water than in air.

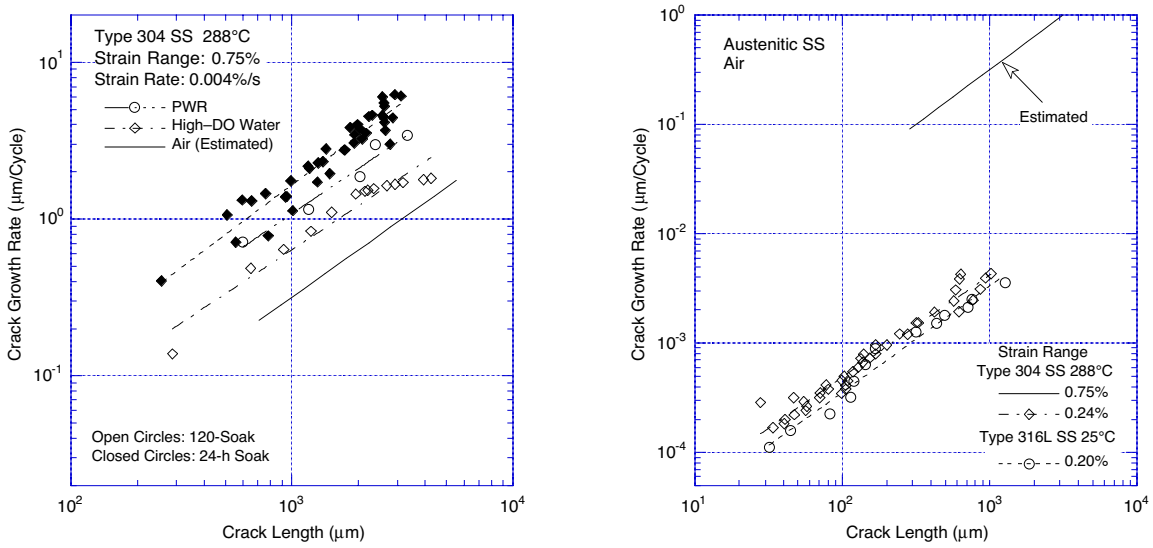


Figure 8. Crack growth rates plotted as a function of crack length for austenitic stainless steels in air and water environments (Refs. 30,33).

The CGR data obtained from fracture–mechanics tests indicate significant enhancement of growth rates in high–DO water;[35] the rates under BWR normal water chemistry (NWC) exceed the air value in the ASME Code by a factor of ≈20–30. The CGRs in air, $\dot{a}_{air}$ (m/s), are determined from the current ASME Section XI correlation at 288°C given by

$$\dot{a}_{air} = 3.43 \times 10^{-12}\, S(R)\, \Delta K^{3.3} / T_R , \qquad (2)$$

where the function S(R) is expressed as

$$\begin{aligned} S(R) &= 1.0 && R < 0 \\ S(R) &= 1.0 + 1.8R && 0 < R < 0.79 \\ S(R) &= -43.35 + 57.97R && 0.79 < R < 1.0, \end{aligned} \qquad (3)$$

and $T_R$ is the rise time (s) of the loading waveform, R is the load ratio ($K_{min}/K_{max}$), and $\Delta K$ is $K_{max} - K_{min}$. The CGR in water [$\dot{a}_{env}$ (m/s)] with 0.2 ppm DO (i.e., BWR NWC) is expressed in terms of the CGR in air ($\dot{a}_{air}$) by the relationship

$$\dot{a}_{env} = \dot{a}_{air} + 4.5 \times 10^{-5} (\dot{a}_{air})^{0.5}. \qquad (4)$$

The CGR data from fracture–mechanics tests in low–DO PWR environments are sparse, particularly at rates that are $<10^{-9}$ m/s. At high CGRs, the observed enhancement in both low– and high–DO environments is relatively small, and the magnitude of the enhancement under the same loading conditions is comparable in the two environments. Until further data become available at low CGRs in simulated PWR water, Shack and Kassner[35] recommend that the environmental enhancement represented by Eq. 4 for 0.2 ppm DO water also be considered for PWR environments.

The CGRs determined from fatigue ε–N tests in water and air environments at 289°C are plotted in Fig. 9. The rates in high–DO and low–DO (PWR) water represent the measured values shown as open diamonds and circles, respectively, in Fig. 8. The CGRs in air for the same loading conditions (i.e., the same crack length) were determined from the estimated rates

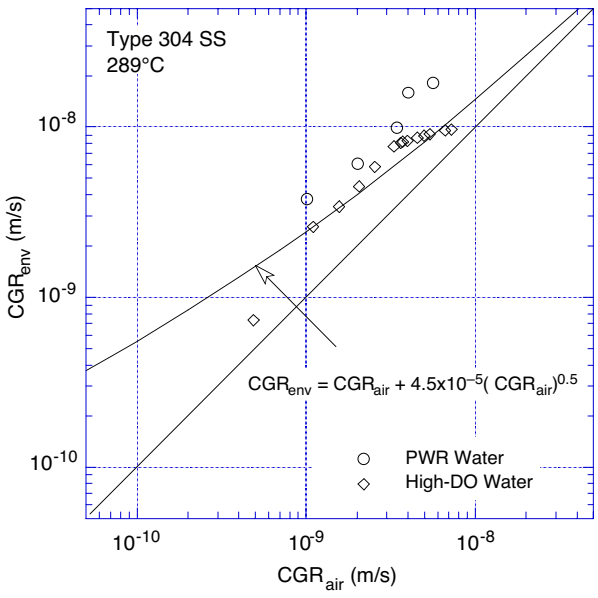


Figure 9.
Crack growth rate data for Type 304 SS determined from fatigue ε–N tests in PWR and high–DO water at 289°C.

in air, shown by a solid line in Fig. 8. The CGRs determined from the ε–N tests in high–DO water are consistent with the trend predicted from Eq. 4; the rates in low–DO water are slightly higher. However, the large reductions in the fatigue life of austenitic SSs in PWR environments cannot be explained entirely on the basis of enhanced CGRs during the propagation stage, i.e., growth of mechanically small cracks. For example, the CGRs in low–DO water are a factor of 1.6 greater than those in high–DO water, but the fatigue life is a factor of ≈4 lower in low–DO water than in high–DO water. As shown in Fig. 7, the decrease in the fatigue lives of austenitic SSs in PWR environments is caused predominantly by the effects of environment on the growth of MSCs.

Equation 4 indicates that environmental effects increase with decreasing CGRs; under loading conditions that correspond to $>10^{-8}$ m/s growth rates in air, mechanical fatigue controls crack advance, and the contribution of environment or corrosion fatigue is insignificant. Because CGRs increase with increasing strain range (Fig. 8), the contribution of corrosion fatigue to crack initiation is likely to decrease with increasing strain range.

It should also be noted that, if enhanced CGRs alone were responsible for the environmentally assisted decrease in fatigue life of materials in LWR environments, environmental effects on the fatigue lives of Alloy 600 and austenitic SSs in LWR environments should be comparable. In air, the fatigue ε–N behavior of Alloy 600 is comparable to that of austenitic SSs.[20] Fatigue CGR data indicate that the enhancement of CGRs of Alloy 600 and austenitic SSs in LWR environments is also comparable.[36] However, the fatigue ε–N behavior of Alloy 600 and austenitic SSs in water differs significantly; only moderate effects of environment are observed for Alloy 600 and its weld both in low– and high–DO water.[37,38] For example, the fatigue life of Alloy 600 weld metal in water with <0.005 ppm DO at 325°C and 0.6% strain amplitude decreased by a factor of ≈2.5 when the strain rate was decreased from 0.4 to 0.001%/s.[37] Under similar environmental and loading conditions, the fatigue life of austenitic SSs decreased by a factor of ≈10. Additional tests on Alloy 600 in low–DO water should be conducted to verify these results.

Studies on crack initiation in carbon and low–alloy steels yield similar results; the decrease in fatigue life in LWR environments is caused primarily by the effects of the environment on the growth of cracks that are <100 μm deep.[7,29] Metallographic evaluation of the specimens indicates that the growth of MSCs in carbon and low–alloy steels occurs predominantly by the slip oxidation/dissolution process.[7] However, for SSs, fatigue lives are lower in low–DO water than in high–DO water; such results are difficult to reconcile in terms of the slip oxidation/dissolution mechanism. The reduction in fatigue life of austenitic SSs in low–DO environments is most likely caused by other mechanisms, such as hydrogen–enhanced crack growth.

### 2.3.3 Fracture Morphology

The crack morphology of the specimen surface is somewhat different in air or high–DO water than in low–DO water. For Type 304 SS, fatigue cracks are always straight and normal to the stress axis in low–DO water, whereas in air or high–DO water, they follow certain crystallographic features (Fig. 10). However, the morphology of crack growth into the material is similar in both air and water. Fatigue cracks appear to grow predominantly as Mode I tensile cracks normal to the stress axis; only a few small shear cracks were observed in Type 304 SS specimens.[12]

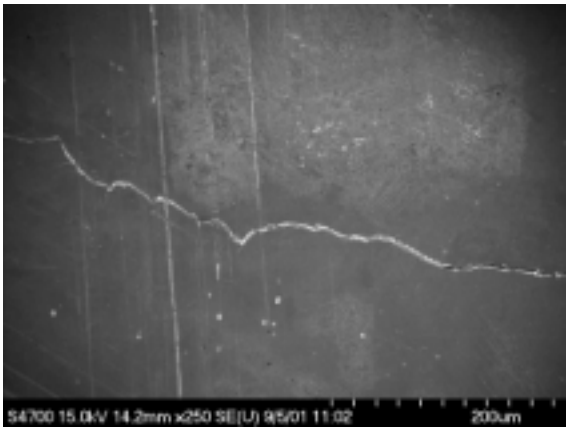


(a)

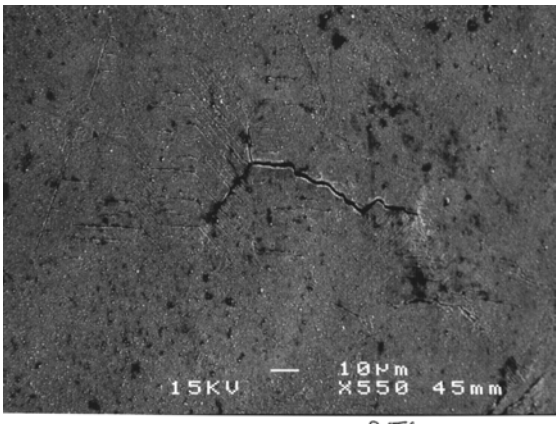


(b)

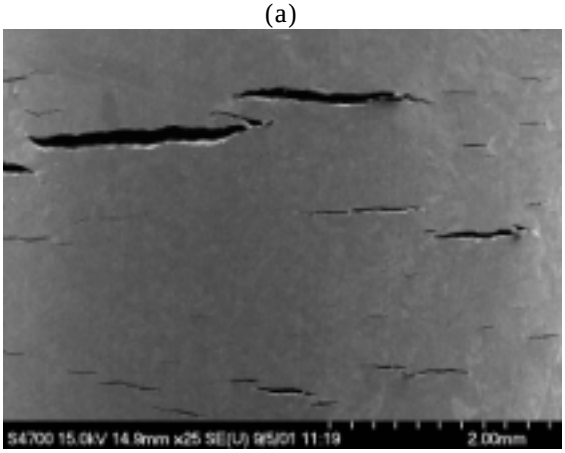


(c)

Figure 10.
Photomicrographs of fatigue cracks on gauge surfaces of Type 304 stainless steel tested in (a) air, (b) high–DO water, and (c) low–DO simulated PWR environment at 288°C, ≈0.75% strain range, and 0.004%/s strain rate.

The fracture morphology of austenitic SSs in an air or LWR environment does not differ significantly; during Stage II growth, well–defined fatigue striations are observed in air and water.[3,12] Figure 11 shows photomicrographs of the fracture surfaces of Type 316NG SS specimens tested at 288°C in air, high–DO water, and a low–DO PWR environment after chemical cleaning and at approximately the same crack length. All specimens show fatigue striations; the spacing between striations is larger in low–DO water than in air. The presence of well–defined striations suggests that mechanical factors, and not the slip dissolution/oxidation process, are important. Fatigue striations should not be observed if crack growth is enhanced by the slip dissolution/oxidation process.

### 2.3.4 Surface Oxide Film

The characteristics of the surface oxide films that form on austenitic SSs in LWR coolant environments can influence the mechanism and kinetics of corrosion processes and thereby influence the initiation stage, i.e., the growth of MSCs. Photomicrographs of the gauge surfaces of Type 316NG specimens tested in simulated PWR water and high–DO water are shown in Fig. 12. Austenitic SSs exposed to LWR environments develop an oxide film that consists of two layers; a fine–grained, tightly–adherent, Cr–rich inner layer, and a crystalline, Ni–rich outer layer composed of large and intermediate–size particles. The inner layer forms by solid–state growth, whereas the crystalline outer layer forms by precipitation or deposition from the solution.

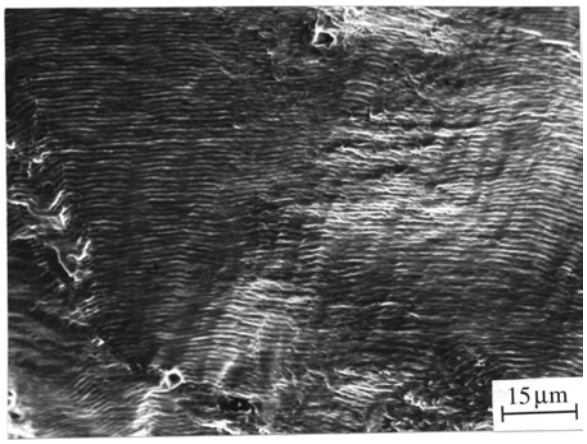


(a)

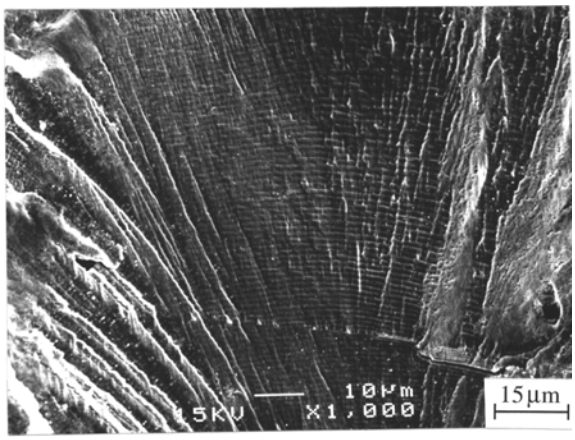


(b)

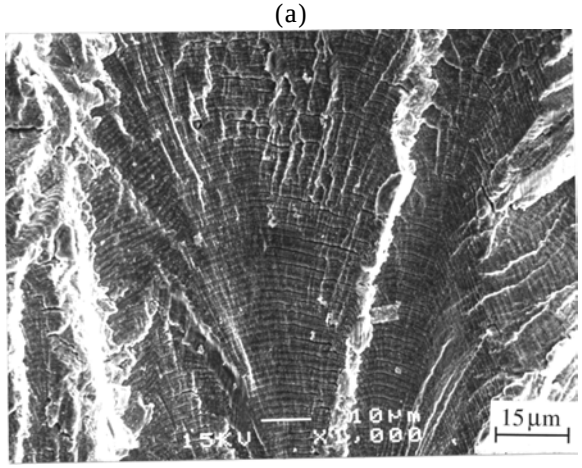


(c)

Figure 11.
Photomicrographs of fracture surfaces of Type 316NG SS specimens tested at 288°C, ≈0.75% strain range, and 0.004%/s strain rate in (a) air, (b) high–DO water, and (c) low–DO simulated PWR water (Refs. 3,12).

A schematic representation of the surface oxide film is shown in Fig. 13. Several studies have characterized the oxide films that form on austenitic SSs in LWR environments.[39–45] The inner layer consists of the Cr–rich spinel $Ni_xCr_yFe_{3-x-y}O_4$ with nonstoichiometric composition; the actual composition of spinels varies with environmental conditions. Kim[39,40] identified the

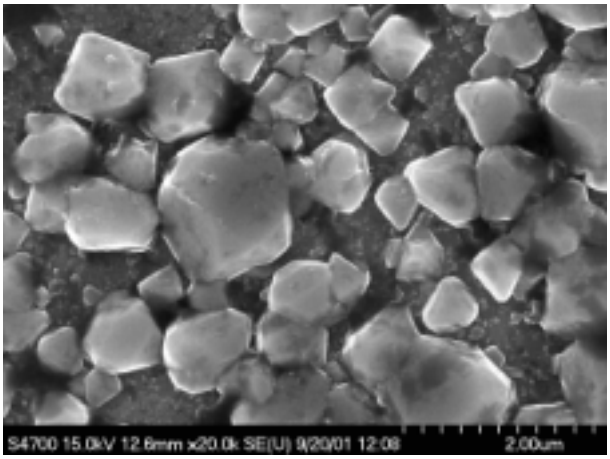


(a)

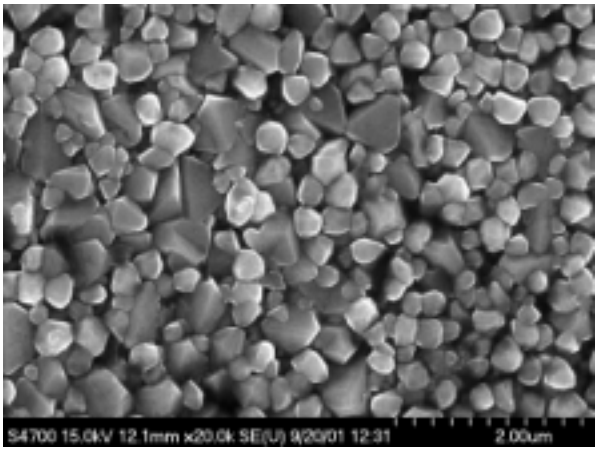


(b)

Figure 12. Photomicrographs of oxide films that formed on Type 316NG stainless steel in (a) simulated PWR water and (b) high–DO water (Ref. 12).

$FeCr_2O_4$ spinel chromite (or $Fe_xCr_{3-x}O_4$), along with $NiFe_2O_4$, in the inner layer formed on Types 304 and 316 SS exposed at 288°C under conditions of NWC or hydrogen water chemistry (HWC). Kim also noted that the inner oxide layer formed in a NWC BWR environment contains a lower concentration of Cr than that formed in a HWC low–DO environment. Such differences have been attributed to Cr oxidation in high–DO water.

The structure and composition of the crystalline outer layer vary with the water chemistry. In BWR environments, the large particles in the outer layer are primarily composed of $\alpha$—$Fe_2O_3$ hematite in NWC, and $Fe_3O_4$ magnetite in HWC.[39,40] The intermediate particles in the outer layer are composed of $\alpha$—$Fe_2O_3$ in NWC and $FeCr_2O_4$ in HWC. The structure of the outer layer varies when the water chemistry is cycled between NWC and HWC. In PWR environments, the large particles have been identified as the $Ni_{0.75}Fe_{2.25}O_4$ spinel, and the intermediate particles, as $Ni_{0.75}Fe_{2.25}O_4 + Fe_3O_4$.[17] The possible effect of minor differences in the surface oxide film on fatigue crack initiation is discussed in the next section.

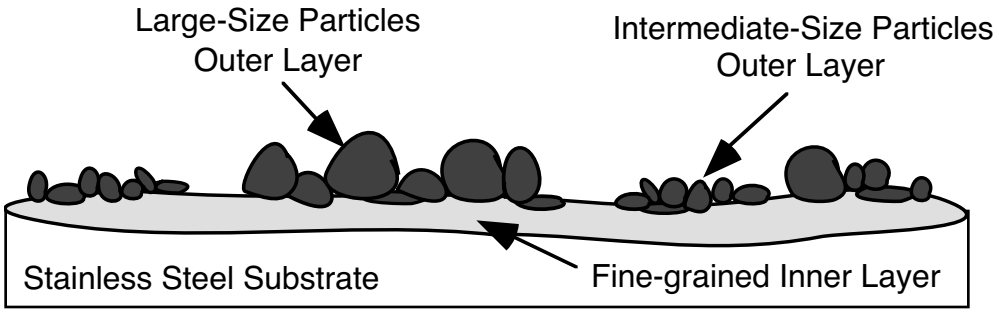


Figure 13. Schematic representation of corrosion oxide film formed on austenitic stainless steels in LWR environments.

### 2.3.5 Exploratory Fatigue Tests

The reduction of fatigue life in high–temperature water has often been attributed to the presence of surface micropits that are formed in high–temperature water and may act as stress raisers and provide preferred sites for the formation of fatigue cracks. In an effort to understand the effects of surface micropits or minor differences in the surface oxide film on fatigue crack initiation, fatigue tests were conducted on Type 316NG (Heat P91576) specimens that were preexposed to either low– or high–DO water and then tested in air or water environments. The results of these tests, and data obtained earlier on this heat and Heat D432804 of Type 316NG SS in air and low–DO water at 288°C, are given in Table 1; the results are plotted in Fig. 14.

Experimental data given in Table 1 indicate that surface micropits have no effect on the formation of fatigue cracks; the fatigue lives of specimens preoxidized at 288°C in low–DO water and then tested in air are identical to those of unoxidized specimens (Fig. 14). If the presence of micropits was responsible for the reduction in life, the preexposed specimens should show a decrease in life. Also, the fatigue limit of these steels should be lower in water than in air. The fatigue limit of austenitic SSs is approximately the same in water and air environments. The presence of an oxide film is not a sufficient condition for the environmentally assisted decrease in fatigue lives of materials in LWR environments.

The results also indicate that minor differences in the composition or structure of the surface oxide film also have no effect on the fatigue life of SSs in low–DO water. The fatigue lives of specimens preoxidized in high– or low–DO water and then tested in low–DO water are identical.

Table 1. Fatigue test results for Type 316NG austenitic stainless steel at 288°C and ≈0.5% strain range

| Test No. | Diss. Oxygen[a] (ppb) | Diss. Hydrogen (cc/kg) | Li (ppm) | Boron (ppm) | pH at RT | Conduc-tivity[b] (µS/cm) | ECP SS[a] mV (SHE) | Ten. Rate (%/s) | Stress Range (MPa) | Strain Range (%) | Life $N_{25}$ (Cycles) |
|---|---|---|---|---|---|---|---|---|---|---|---|
| Heat D432804 | | | | | | | | | | | |
| 1409 | Air Env. | – | – | – | – | – | – | 5.0E-1 | 377.2 | 0.50 | 53,144 |
| 1410 | Air Env. | – | – | – | – | – | – | 5.0E-1 | 377.6 | 0.50 | 51,194 |
| 1792 | Air Env. | – | – | – | – | – | – | 5.0E-3 | 413.4 | 0.50 | 35,710 |
| 1794 | 4 | 23 | 2 | 1000 | 6.4 | 20.00 | –689 | 5.0E-3 | 390.9 | 0.50 | 7,370 |
| Heat P91576 | | | | | | | | | | | |
| 1872[c] | Air Env. | – | – | – | – | – | – | 4.0E-1 | 369.3 | 0.51 | 48,100 |
| 1878[c] | Air Env. | – | – | – | – | – | – | 4.0E-3 | 401.1 | 0.50 | 58,300 |
| 1879[c] | 5 | 23 | – | – | – | 0.06 | -591 | 4.0E-3 | 380.2 | 0.50 | 8,310 |
| 1880[d] | 5 | 23 | – | – | – | 0.10 | -603 | 4.0E-3 | 382.8 | 0.50 | 8,420 |

[a]Measured in effluent.
[b]Measured in feedwater supply tank.
[c]Specimen soaked for 10 days in high–purity water with <5 ppb dissolved oxygen and ≈23 cc/kg dissolved hydrogen.
[d]Specimen soaked for 10 days in high–purity water with ≈500 ppb dissolved oxygen.

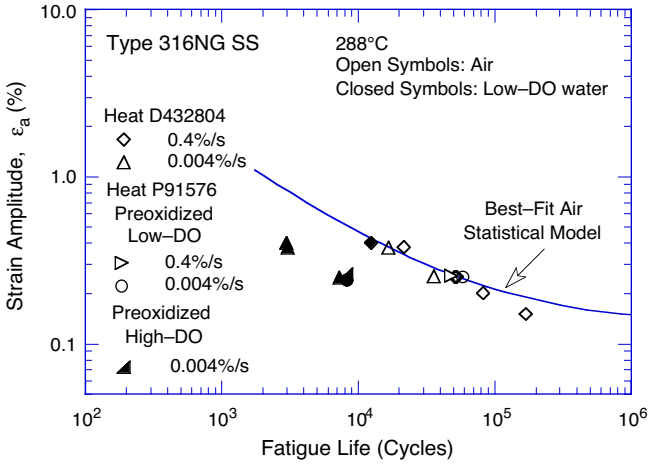


Figure 14.
Effects of environment on formation of fatigue cracks in Type 316NG SS in air and low–DO water environments at 288°C. Preoxidized specimens were exposed for 10 days at 288°C in water that contained either <5 ppb DO and ≈23 $cm^3$/kg dissolved $H_2$ or ≈500 ppb DO and no dissolved $H_2$.

# 3 Irradiation–Assisted Stress Corrosion Cracking of Austenitic Stainless Steel in BWRS

The susceptibility of austenitic SSs and their welds to IASCC as a function of the fluence level, water chemistry, material chemistry, welding process, and fabrication history is being evaluated. Crack growth rate tests and SSRTs are being conducted on model SSs, irradiated at ≈288°C in a He environment in the Halden boiling heavy water reactor, to investigate the effects of material chemistry and irradiation level on the susceptibility of SSs to IASCC. Crack growth tests will be conducted on irradiated specimens of submerged arc (SA) and shielded metal arc (SMA) welds of Types 304 and 304L SS to establish the effects of fluence level, material chemistry, and welding process on IASCC. Models and codes developed under CIR and from industry sources will be benchmarked and used in conjunction with this work. However, for CGR models for irradiated materials it is anticipated that relatively few data will be available because of the expense and difficulty of testing. Additional testing on nonirradiated materials will be performed to provide "limiting cases" against which the models can be tested. These tests will seek to determine the effects of Cr level in the steel and cold work on CGRs in austenitic SSs in LWR environments.

During this reporting period, SSRTs were performed on specimens irradiated to a "high-fluence" level of ≈2.0 x $10^{21}$ n $cm^{-2}$ (E > 1 MeV) and CGR tests were conducted on nonirradiated materials to establish the procedure and conditions that will be used for the tests on irradiated materials.

## 3.1 Slow-Strain-Rate-Tensile Test of Model Austenitic Stainless Steels Irradiated in the Halden Reactor (H. M. Chung, R. V. Strain, and R. W. Clark)

### 3.1.1 Introduction

Failures of some BWR and PWR core internal components have been observed after accumulation of fast neutron fluences higher than ≈0.5 x $10^{21}$ n $cm^{-2}$ (E >1 MeV) (≈0.7 dpa) in BWRs and at fluences approximately an order of magnitude higher in PWRs. The general pattern of the observed failures indicates that, as nuclear plants age and fluence increases, various nonsensitized austenitic SSs become susceptible to intergranular (IG) failure. Failure of welded components (such as core shrouds fabricated from Type 304 or 304L SS) has also been observed in many BWRs, usually at fluence levels significantly lower than the threshold fluence for the solution-annealed base-metal components.

Although most failed components can be replaced, some safety–significant structural components (e.g., the BWR top guide, core shroud, and core plate) would be very difficult or costly to replace. Therefore, the structural integrity of these components has been a subject of concern, and extensive research has been conducted to provide an understanding of this type of degradation, which is commonly known as irradiation-assisted stress corrosion cracking (IASCC).[46–67]

Irradiation produces profound effects on local coolant water chemistry and component microstructure. Neutron irradiation causes alteration of microchemistry, microstructure, and mechanical properties of the core internal components, which are usually fabricated from ASTM Types 304, 304L, 316, or 348 SS. Irradiation produces defects, defect clusters, and

defect-impurity complexes in grain matrices and alters the dislocation and dislocation loop structures, leading to radiation-induced hardening, and in many cases, flow localization via dislocation channeling. Irradiation also leads to changes in the stability of second–phase precipitates and the local alloy chemistry near grain boundaries, precipitates, and defect clusters. Grain–boundary microchemistry significantly different from bulk composition can be produced in association with not only radiation–induced segregation but also thermally driven equilibrium and nonequilibrium segregation of alloying and impurity elements.

Irradiation–induced grain–boundary depletion of Cr has been considered for many years to be the primary metallurgical process that leads to IASCC in BWRs. One of the most important factors that seems to support the Cr–depletion mechanism is the observation that the dependence on water chemistry (i.e., oxidizing potential) of IGSCC of nonirradiated thermally sensitized material and of IASCC of BWR–irradiated solution–annealed material is similar.[46–48] Many investigators have also implicated radiation–induced segregation of common impurities such as Si and P and other minor impurities such as S, O, B, and F.[52–64] However, the exact mechanism of IASCC remains unknown.

In general, IASCC is characterized by strong heat-to-heat variation in susceptibility, in addition to strong effects of irradiation condition, material type, and grade, even among materials of virtually identical chemical composition. These findings indicate that the traditional interpretation based on the role of grain-boundary Cr depletion alone cannot completely explain the IASCC mechanism. In view of this background, an irradiation test program is being conducted to systematically investigate the effects of alloying and impurity elements (Cr, Ni, Si, P, S, Mn, C, N, and O) on the susceptibility of austenitic SSs to IASCC at several fluence levels.

In previous studies, SSRTs and fractographic analyses were conducted on model austenitic SS alloys irradiated at 289°C to a "low-fluence" level of ≈0.3 x $10^{21}$ n $cm^{-2}$ (E > 1 MeV) (≈0.43 dpa), and a "medium-fluence" level of ≈0.9 x $10^{21}$ n $cm^{-2}$ (E > 1 MeV) (≈1.3 dpa).[68–71] This report describes results of initial SSRTs and posttest fractographic analysis performed on specimens irradiated to a "high-fluence" level of ≈2.0 x $10^{21}$ n $cm^{-2}$ (E > 1 MeV) (≈3 dpa).

### 3.1.2 Materials, Irradiation, SSRTs, and Fractographic Analysis

The irradiation test matrix consists of 27 model austenitic SS alloys; the composition of these alloys is given in Table 2. Of these 27 alloys, 8 were commercially purchased heats of Types 304, 304L, and 316 SS. The prefix "C" was added to the identification number of these 8 commercial heats, i.e., Heats C1, C3, C9, C10, C12, C16, C19, and C21 in Table 2. The remaining 19 heats were fabricated in the laboratory; all were designated with identification numbers that began with "L," e.g., L8 and L25C3 (designation L25C3, for example, means a heat fabricated in laboratory that contains a chemical composition close to that of commercial heat C3).

The SSRT specimens were irradiated in the Halden boiling heavy-water reactor in He-filled capsules maintained at 289°C. All SSRTs were conducted in a low-activity-level hot cell in simulated BWR-like deionized water at 289°C. Dissolved oxygen in the water was maintained at ≈8 ppm. Conductivity and pH of the water were kept at ≈0.07-0.10 μS $cm^{-1}$ and

6.3-6.8, respectively. Strain rate was held constant at 1.65 x $10^{-7}$ $s^{-1}$ in a screw driven load frame. Electrochemical potential was measured on the effluent side at regular intervals.

After completion of SSRTs, the fracture tip of the specimen was cut and examined in a shielded scanning electron microscope (SEM) to determine the morphology of the fracture surface, i.e., percent transgranular stress corrosion cracking (TGSCC) and percent IGSCC produced in water at ≈289°C. Fractographs were obtained at magnifications of 50, 200, and 500 times, and composite fracture surface images were prepared at the medium and high magnifications. All fractographs were stored in digitized format for permanent record.

Table 2. Elemental composition of 27 commercial and laboratory model austenitic SS alloys irradiated in the Halden Reactor

| ANL | Source | Composition (wt.%) | | | | | | | | | | |
|---|---|---|---|---|---|---|---|---|---|---|---|---|
| ID[a] | Heat ID | Ni | Si | P | S | Mn | C | N | Cr | O | B | Mo or Nb |
| C1 | DAN-70378 | 8.12 | 0.50 | 0.038 | 0.002 | 1.00 | 0.060 | 0.060 | 18.11 | - | <0.001 | - |
| L2 | BPC-4-111 | 10.50 | 0.82 | 0.080 | 0.034 | 1.58 | 0.074 | 0.102 | 17.02 | 0.0065 | <0.001 | - |
| C3 | PNL-C-1 | 8.91 | 0.46 | 0.019 | 0.004 | 1.81 | 0.016 | 0.083 | 18.55 | - | <0.001 | - |
| L4 | BPC-4-88 | 10.20 | 0.94 | 0.031 | 0.010 | 1.75 | 0.110 | 0.002 | 15.80 | - | <0.001 | - |
| L5 | BPC-4-104 | 9.66 | 0.90 | 0.113 | 0.028 | 0.47 | 0.006 | 0.033 | 21.00 | - | <0.001 | - |
| L6 | BPC-4-127 | 10.00 | 1.90 | 0.020 | 0.005 | 1.13 | 0.096 | 0.087 | 17.10 | 0.0058 | <0.001 | - |
| L7 | BPC-4-112 | 10.60 | 0.18 | 0.040 | 0.038 | 1.02 | 0.007 | 0.111 | 15.40 | 0.0274 | <0.001 | - |
| L8 | BPC-4-91 | 10.20 | 0.15 | 0.093 | 0.010 | 1.85 | 0.041 | 0.001 | 18.30 | - | <0.001 | - |
| C9 | PNL-C-6 | 8.75 | 0.39 | 0.013 | 0.013 | 1.72 | 0.062 | 0.065 | 18.48 | - | <0.001 | - |
| C10 | DAN-23381 | 8.13 | 0.55 | 0.033 | 0.002 | 1.00 | 0.060 | 0.086 | 18.19 | - | <0.001 | - |
| L11 | BPC-4-93 | 8.15 | 0.47 | 0.097 | 0.009 | 1.02 | 0.014 | 0.004 | 17.40 | - | <0.001 | - |
| C12 | DAN-23805 | 8.23 | 0.47 | 0.018 | 0.002 | 1.00 | 0.060 | 0.070 | 18.43 | - | <0.001 | - |
| L13 | BPC-4-96 | 8.18 | 1.18 | 0.027 | 0.022 | 0.36 | 0.026 | 0.001 | 17.40 | - | <0.001 | - |
| L14 | BPC-4-129 | 7.93 | 1.49 | 0.080 | 0.002 | 1.76 | 0.107 | 0.028 | 15.00 | 0.0045 | <0.001 | - |
| L15 | BPC-4-126 | 8.00 | 1.82 | 0.010 | 0.013 | 1.07 | 0.020 | 0.085 | 17.80 | 0.0110 | <0.001 | - |
| C16 | PNL-SS-14 | 12.90 | 0.38 | 0.014 | 0.002 | 1.66 | 0.020 | 0.011 | 16.92 | 0.0157 | <0.001 | Mo 2.30 |
| L17 | BPC-4-128 | 8.00 | 0.66 | 0.090 | 0.009 | 0.48 | 0.061 | 0.078 | 15.30 | 0.0090 | <0.001 | - |
| L18 | BPC-4-98 | 8.13 | 0.14 | 0.016 | 0.033 | 1.13 | 0.080 | 0.001 | 18.00 | - | <0.001 | - |
| C19 | DAN-74827 | 8.08 | 0.45 | 0.031 | 0.003 | 0.99 | 0.060 | 0.070 | 18.21 | 0.0200 | <0.001 | - |
| L20 | BPC-4-101 | 8.91 | 0.017 | 0.010 | 0.004 | 0.41 | 0.002 | 0.002 | 18.10 | 0.0940 | <0.001 | - |
| C21 | DAN-12455 | 10.24 | 0.51 | 0.034 | 0.001 | 1.19 | 0.060 | 0.020 | 16.28 | - | <0.001 | Mo 2.08 |
| L22 | BPC-4-100 | 13.30 | 0.024 | 0.015 | 0.004 | 0.40 | 0.003 | 0.001 | 16.10 | - | <0.001 | Mo 2.04 |
| L23 | BPC-4-114 | 12.04 | 0.68 | 0.030 | 0.047 | 0.96 | 0.043 | 0.092 | 17.30 | 0.0093 | <0.001 | Nb 1.06 |
| L24 | BPC-4-105 | 12.30 | 0.03 | 0.007 | 0.005 | 0.48 | 0.031 | 0.002 | 16.90 | 0.0129 | <0.001 | Nb 1.72 |
| L25C3 | BPC-4-133 | 8.93 | 0.92 | 0.020 | 0.008 | 1.54 | 0.019 | 0.095 | 17.20 | 0.0085 | 0.010 | - |
| L26C19 | BPC-4-131 | 8.09 | 0.79 | 0.004 | 0.002 | 0.91 | 0.070 | 0.089 | 17.20 | 0.0080 | <0.001 | - |
| L27C21 | BPC-4-132 | 10.30 | 0.96 | 0.040 | 0.002 | 0.97 | 0.057 | 0.019 | 15.30 | 0.0058 | 0.030 | Mo 2.01 |

[a]The first letters "C" or "L" denotes, respectively, a commercial or laboratory heat.

Some of the SSRT specimens tested in 289°C water were fractured in the shoulder region (away from the fracture produced in the 289°C water) by bending in air at ≈23°C. Then, the morphology of the fracture surface produced in 23°C air was examined and compared with the fracture surface morphology produced in water at 289°C in the same specimen. The objective of the 23°C bending test was to determine the susceptibility to purely mechanical IG fracture in an inert atmosphere (in the absence of water), thereby providing insight to a better understanding of the mechanism(s) of IG and IASCC failure of irradiated austenitic SSs.

### 3.1.3 Tabulation of Test Results

Results of SSRTs and fractographic analysis, completed for specimens irradiated to ≈0.9 and ≈2.0 x $10^{21}$ n $cm^{-2}$ (E > 1 MeV) (≈1.3 and 3.0 dpa), are summarized in Tables 3-6. Test conditions, results of SSRT, and fractographic characteristics (percent IGSCC, percent TGSCC, and combined percent IGSCC + TGSCC) are listed in Tables 3 and 5, respectively, for specimens irradiated to ≈1.3 and 3.0 dpa. These results are correlated with compositional characteristics of the alloys in Tables 4 and 6.

Of the 27 alloys irradiated to ≈2.0 x $10^{21}$ n $cm^{-2}$ (E > 1 MeV), only 13 were subjected to SSRT during this reporting period. Tests on the other 14 alloys will be completed soon, and the results will be reported elsewhere. A few alloys irradiated to this "high-fluence" level (≈3 dpa) were brittle and failed in the hot cell at 23°C during preparation of the test train, e.g., L13-03 and L8-03 (see Table 5).

Table 3. Stress corrosion test conditions, results of SSRTs[a] and SEM fractography for model austenitic SS alloys irradiated to 0.9 x $10^{21}$ n $cm^{-2}$ (E > 1 MeV)

| Alloy & | | Feedwater Chemistry | | | | SSRT Parameters | | | | Fracture Behavior | | |
|---|---|---|---|---|---|---|---|---|---|---|---|---|
| Spec. | | Oxygen | Average | Cond. | | Yield | Max. | Uniform | Total | | | TGSCC |
| Ident. | SSRT | Conc. | ECP | at 25°C | pH | Stress | Stress | Elongation | Elongation | TGSCC | IGSCC | IGSCC |
| No. | No. | (ppm) | (mV SHE) | (μS·$cm^{-1}$) | at 25°C | (MPa) | (MPa) | (%) | (%) | (%) | (%) | (%) |
| L22-02 | HR-17 | 8.0 | +181 | 0.08 | 6.77 | 475 | 549 | 4.20 | 5.82 | 30 | 35 | 65 |
| L11-02 | HR-18 | 8.0 | +191 | 0.08 | 6.55 | 820 | 856 | 0.43 | 1.65 | 50 | 14 | 64 |
| L18-02 | HR-19 | 8.0 | +193 | 0.10 | 6.07 | 710 | 755 | 3.98 | 5.05 | 38 | 14 | 52 |
| L20-02 | HR-28 | Test in 289°C Air | | | | 826 | 845 | 0.31 | 2.09 | Dendritic structure | | |
| L20-05 | HR-26 | 9.0 | +182 | 0.09 | 6.32 | 670 | 743 | 0.37 | 1.03 | Dendritic structure | | |
| L20-06 | HR-27 | 8.0 | +274 | 0.07 | 6.05 | 632 | 697 | 0.85 | 2.72 | 0 | 0 | 0 |
| C9-02 | HR-21 | 8.0 | +240 | 0.07 | 6.47 | 651 | 679 | 1.42 | 2.50 | 62 | 22 | 84 |
| L17-02 | HR-22 | 8.0 | +198 | 0.07 | 6.42 | 574 | 654 | 2.02 | 3.08 | 44 | 41 | 85 |
| L7-02 | HR-23 | 8.0 | +215 | 0.07 | 6.03 | 553 | 561 | 0.24 | 2.44 | 38 | 54 | 92 |
| C10-02 | HR-24 | 7.0 | +221 | 0.07 | 5.26 | 651 | 706 | 6.35 | 9.25 | 14 | 0 | 14 |
| C3-02 | HR-25 | 8.0 | +240 | 0.07 | 6.34 | 632 | 668 | 16.72 | 19.74 | 9 | 4 | 13 |
| C19-02 | HR-30 | Test in 289°C Air | | | | 888 | 894 | 6.41 | 10.21 | 1 | 0 | 1 |
| C19-04 | HR-31 | 8.0 | +252 | 0.07 | 6.18 | 750 | 769 | 6.06 | 8.79 | 1 | 0 | 1 |
| L6-02 | HR-32 | 8.0 | +250 | 0.07 | 6.40 | 493 | 546 | 2.45 | 3.77 | 8 | 27 | 35 |
| L14-02 | HR-33 | 8.0 | +246 | 0.08 | 6.07 | 649 | 684 | 1.90 | 4.67 | 84 | 2 | 86 |
| L13-02 | HR-34 | 7.0 | +222 | 0.09 | 6.85 | 602 | 624 | 1.67 | 4.95 | 55 | 12 | 67 |
| L04-02 | HR-35 | 7.0 | +259 | 0.08 | 6.54 | 634 | 680 | 1.07 | 2.02 | 58 | 12 | 70 |
| L05-02 | HR-36 | 7.0 | +243 | 0.07 | 6.85 | 665 | 725 | 3.07 | 4.57 | 3 | 5 | 8 |
| C16-02 | HR-37 | 7.0 | +230 | 0.07 | 6.62 | 562 | 618 | 11.99 | 15.80 | 7 | 1 | 8 |
| L8-02 | HR-38 | 8.0 | +242 | 0.07 | 6.57 | 838 | 838 | 0.12 | 3.12 | 15 | 22 | 37 |
| C21-02 | HR-39 | 8.0 | +231 | 0.08 | 6.21 | 643 | 716 | 15.38 | 18.30 | 1 | 2 | 3 |
| L2-02 | HR-40 | 7.0 | +239 | 0.07 | 7.11 | 839 | 849 | 0.88 | 1.56 | 31 | 11 | 42 |
| L24-02 | HR-41 | 8.0 | +239 | 0.06 | 6.40 | 725 | 725 | 0.15 | 2.45 | 2 | 1 | 3 |
| L23-02 | HR-42 | 7.0 | +237 | 0.08 | 6.60 | 787 | 818 | 0.38 | 1.24 | 3 | 24 | 27 |
| C12-02 | HR-43 | 7.0 | +227 | 0.07 | 6.19 | 747 | 756 | 14.96 | 18.57 | 4 | 0 | 4 |
| C1-02 | HR-44 | 8.0 | +229 | 0.07 | 6.30 | 707 | 763 | 13.36 | 17.04 | 2 | 0 | 2 |

[a]Test at 289°C and a strain rate of 1.65 x $10^{-7}$ $s^{-1}$ in simulated BWR-like water; DO ≈8 ppm.

Table 4. Composition characteristics of model austenitic SS alloys irradiated to 0.9 x $10^{21}$ n $cm^{-2}$ (E > 1 MeV) correlated with results of SSRTs[a] and SEM fractography

| Alloy ID | Ni | Si | P | S | Mn | C | N | Cr | Mo, Nb, or O | Remark[b] | YS (MPa) | UTS (MPa) | UE (%) | TE (%) | TG (%) | IG (%) | TG+IG (%) |
|---|---|---|---|---|---|---|---|---|---|---|---|---|---|---|---|---|---|
| L22-02 | 13.30 | 0.024 | 0.015 | 0.004 | 0.40 | 0.003 | 0.001 | 16.10 | Mo 2.04 | HP 316L; low Si, N, S | 475 | 549 | 4.20 | 5.82 | 30 | 35 | 65 |
| L11-02 | 8.15 | 0.47 | 0.097 | 0.009 | 1.02 | 0.014 | 0.004 | 17.40 | - | high P; low Si, C, S, N | 820 | 856 | 0.43 | 1.65 | 50 | 14 | 64 |
| L18-02 | 8.13 | 0.14 | 0.016 | 0.033 | 1.13 | 0.080 | 0.001 | 18.00 | - | low Si, N | 710 | 755 | 3.98 | 5.05 | 38 | 14 | 52 |
| L20-05 | 8.91 | 0.017 | 0.010 | 0.004 | 0.41 | 0.002 | 0.002 | 18.10 | O 0.0940 | high O; low Si, N; HP 304L | 670 | 743 | 0.37 | 1.03 | Dendritic structure | | |
| L20-06 | 8.91 | 0.017 | 0.010 | 0.004 | 0.41 | 0.002 | 0.002 | 18.10 | O 0.0940 | high O; low Si, N; HP 304L | 632 | 697 | 0.85 | 2.72 | Dendritic structure | | |
| C9-02 | 8.75 | 0.39 | 0.013 | 0.013 | 1.72 | 0.062 | 0.065 | 18.48 | - | low Si; high Mn | 651 | 679 | 1.42 | 2.50 | 62 | 22 | 84 |
| L17-02 | 8.00 | 0.66 | 0.090 | 0.009 | 0.48 | 0.061 | 0.078 | 15.30 | O 0.0090 | high P; low Cr, Mn, S | 574 | 654 | 2.02 | 3.08 | 44 | 41 | 85 |
| L7-02 | 10.60 | 0.18 | 0.040 | 0.038 | 1.02 | 0.007 | 0.111 | 15.40 | O 0.0274 | high S, N, O; low Si, C | 553 | 561 | 0.24 | 2.44 | 38 | 54 | 92 |
| C10-02 | 8.13 | 0.55 | 0.033 | 0.002 | 1.00 | 0.060 | 0.086 | 18.19 | - | CP 304; low S; high N | 651 | 706 | 6.35 | 9.25 | 14 | 0 | 14 |
| C3-02 | 8.91 | 0.46 | 0.019 | 0.004 | 1.81 | 0.016 | 0.083 | 18.55 | - | CP 304L; high Mn, N; low S | 632 | 668 | 16.7 | 19.7 | 9 | 4 | 13 |
| C19-04 | 8.08 | 0.45 | 0.031 | 0.003 | 0.99 | 0.060 | 0.070 | 18.21 | O 0.0200 | CP 304; low S | 750 | 769 | 6.06 | 8.79 | 1 | 0 | 1 |
| L6-02 | 10.00 | 1.90 | 0.020 | 0.005 | 1.13 | 0.096 | 0.087 | 17.10 | O 0.0058 | high Si; low S | 493 | 546 | 2.45 | 3.77 | 8 | 27 | 35 |
| L14-02 | 7.93 | 1.49 | 0.080 | 0.002 | 1.76 | 0.107 | 0.028 | 15.00 | O 0.0045 | high Si, P, Mn; low Cr, S | 649 | 684 | 1.90 | 4.67 | 84 | 2 | 86 |
| L13-02 | 8.18 | 1.18 | 0.027 | 0.022 | 0.36 | 0.026 | 0.001 | 17.40 | - | high Si, S; Low Mn, C, N | 602 | 624 | 1.67 | 4.95 | 55 | 12 | 67 |
| L4-02 | 10.20 | 0.94 | 0.031 | 0.010 | 1.75 | 0.110 | 0.002 | 15.80 | - | high Si, C; low N, Cr | 634 | 680 | 1.07 | 2.02 | 58 | 12 | 70 |
| L5-02 | 9.66 | 0.90 | 0.113 | 0.028 | 0.47 | 0.006 | 0.033 | 21.00 | 3% ferrite | high Si, P, Cr; Low Mn, C | 665 | 725 | 3.07 | 4.57 | 3 | 5 | 8 |
| C16-02 | 12.90 | 0.38 | 0.014 | 0.002 | 1.66 | 0.020 | 0.011 | 16.92 | Mo 2.30<br>O 0.0157 | CP 316L; low P, S, C | 562 | 618 | 12.0 | 15.8 | 7 | 1 | 8 |
| L8-02 | 10.20 | 0.15 | 0.093 | 0.010 | 1.85 | 0.041 | 0.001 | 18.30 | - | high P, Mn; low Si, N | 838 | 838 | 0.12 | 3.12 | 15 | 22 | 37 |
| C21-02 | 10.24 | 0.51 | 0.034 | 0.001 | 1.19 | 0.060 | 0.020 | 16.28 | Mo 2.08 | CP 316, low S | 643 | 716 | 15.4 | 18.3 | 1 | 2 | 3 |
| L2-02 | 10.50 | 0.82 | 0.080 | 0.034 | 1.58 | 0.074 | 0.102 | 17.02 | O 0.0066 | high O, P, S, N | 839 | 849 | 0.88 | 1.56 | 31 | 11 | 42 |
| L24-02 | 12.30 | 0.03 | 0.007 | 0.005 | 0.48 | 0.031 | 0.002 | 16.90 | Nb 1.72<br>O 0.0129 | HP 348L; low Si, P, S, C, N | 725 | 725 | 0.15 | 2.45 | 2 | 1 | 3 |
| L23-02 | 12.04 | 0.68 | 0.030 | 0.047 | 0.96 | 0.043 | 0.092 | 17.30 | Nb 1.06<br>O 0.0093 | CP 348, high S | 787 | 818 | 0.38 | 1.24 | 3 | 24 | 27 |
| C12-02 | 8.23 | 0.47 | 0.018 | 0.002 | 1.00 | 0.060 | 0.070 | 18.43 | - | 304, low S, low P | 747 | 756 | 15.0 | 18.6 | 4 | 0 | 4 |
| C1-02 | 8.12 | 0.50 | 0.038 | 0.002 | 1.00 | 0.060 | 0.060 | 18.11 | - | 304, low S | 707 | 763 | 13.4 | 17.0 | 2 | 0 | 2 |

[a]Test at 289°C and a strain rate of 1.65 x $10^{-7}$ $s^{-1}$ in simulated BWR-like water; DO ≈8 ppm.
[b]HP = high purity, CP = commercial purity.

Table 5. Stress corrosion test conditions, results of SSRTs[a] and SEM fractography of model austenitic SS alloys irradiated to 2.0 x $10^{21}$ n $cm^{-2}$ (E > 1 MeV)

| Alloy & Spec. Ident. No. | SSRT No. | Feedwater Chemistry: Oxygen Conc. (ppm) | Feedwater Chemistry: Average ECP (mV SHE) | Feedwater Chemistry: Cond. at 25°C (μS·$cm^{-1}$) | Feedwater Chemistry: pH at 25°C | SSRT Parameters: Yield Stress (MPa) | SSRT Parameters: Max. Stress (MPa) | SSRT Parameters: Uniform Elongation (%) | SSRT Parameters: Total Elongation (%) | Fracture Behavior: TGSCC (%) | Fracture Behavior: IGSCC (%) | Fracture Behavior: TGSCC IGSCC (%) |
|---|---|---|---|---|---|---|---|---|---|---|---|---|
| L4-03 | HR-45 | 9.0 | +198 | 0.09 | 6.52 | 876 | 1068 | 2.49 | 3.27 | 5 | 95 | 100 |
| C12-03 | HR-46 | 8.0 | +208 | 0.09 | 6.32 | 922 | 966 | 1.28 | 2.73 | 8 | 2 | 10 |
| C9-03 | HR-47 | 8.0 | +212 | 0.11 | 6.47 | early failure during start of loading | | | | 6 | 94 | 100 |
| L5-03 | HR-48 | 8.0 | +204 | 0.10 | 6.58 | 953 | 985 | 0.59 | 2.97 | 2 | 4 | 6 |
| C19-03 | HR-49 | 8.0 | +171 | 0.11 | 6.68 | 787 | 801 | 0.89 | 3.32 | 2 | 62 | 64 |
| C16-03 | HR-50 | 7.9 | +202 | 0.10 | 6.62 | 766 | 803 | 0.83 | 1.84 | 2 | 29 | 31 |
| C10-03 | HR-51 | 8.0 | +167 | 0.11 | 6.04 | 1062 | 1065 | 3.15 | 4.51 | 3 | 0 | 3 |
| L18-03 | HR-52 | 8.0 | +169 | 0.11 | 6.0 | 795 | 779 | 0.35 | 1.75 | 5 | 86 | 91 |
| L13-03 | HR-53 | - | - | brittle fracture during test preparation | | | | | - | - | - | - |
| C1-03 | HR-54 | 7.8 | +161 | 0.10 | 6.5 | 802 | 833 | 3.38 | 5.27 | 2 | 0 | 2 |
| C3-03 | HR-55 | 7.8 | +160 | 0.10 | 6.5 | 796 | 826 | 5.05 | 7.31 | 0 | 26 | 2 |
| C21-03 | HR-56 | 7.6 | +156 | 0.10 | 6.5 | 893 | 893 | 1.89 | 4.85 | - | - | - |
| L8-03 | HR-57 | - | - | brittle fracture during test preparation | | | | | - | - | - | - |

[a]Test at 289°C and a strain rate of 1.65 x $10^{-7}$ $s^{-1}$ in simulated BWR-like water; DO ≈8 ppm.

Table 6. Composition characteristics of model SS alloys irradiated to 2.0 x $10^{21}$ n $cm^{-2}$ correlated with SEM fractography after SSRT in 289°C water[a]

| Alloy ID | Ni | Si | P | S | Mn | C | N | Cr | O | Remark[b] | YS (MPa) | UTS (MPa) | UE (%) | TE (%) | IGSCC (%) |
|---|---|---|---|---|---|---|---|---|---|---|---|---|---|---|---|
| L4-03 | 10.20 | 0.94 | 0.031 | 0.010 | 1.75 | 0.110 | 0.002 | 15.80 | - | high Ni, S; low Cr, N | 876 | 1068 | 2.49 | 3.27 | 95 |
| C12-03 | 8.23 | 0.47 | 0.018 | 0.002 | 1.00 | 0.060 | 0.070 | 18.43 | - | CP 304; low S | 922 | 966 | 1.28 | 2.73 | 2 |
| C9-03 | 8.75 | 0.39 | 0.013 | 0.013 | 1.72 | 0.062 | 0.065 | 18.48 | - | CP 304; low S, Mn | | | | | 94 |
| L5-03 | 9.66 | 0.90 | 0.113 | 0.028 | 0.47 | 0.006 | 0.033 | 21.00 | 3% ferrite | high Cr, P, S; Low Mn, C | 953 | 985 | 0.59 | 2.97 | 4 |
| C19-03 | 8.08 | 0.45 | 0.031 | 0.003 | 0.99 | 0.060 | 0.070 | 18.21 | O 0.0200 | CP 304; low S; high O | 787 | 801 | 0.89 | 3.32 | 62 |
| C16-03 | 12.90 | 0.38 | 0.014 | 0.002 | 1.66 | 0.020 | 0.011 | 16.92 | Mo 2.30 O 0.0157 | CP 316L; low S | 766 | 803 | 0.83 | 1.84 | 29 |
| C10-03 | 8.13 | 0.55 | 0.033 | 0.002 | 1.00 | 0.060 | 0.086 | 18.19 | - | CP 304; low S | 1062 | 1065 | 3.15 | 4.51 | 0 |
| L18-03 | 8.13 | 0.14 | 0.016 | 0.033 | 1.13 | 0.080 | 0.001 | 18.00 | - | CP 304; low S; high Ni | 795 | 779 | 0.35 | 1.75 | 86 |
| L13-03 | 8.18 | 1.18 | 0.027 | 0.022 | 0.36 | 0.026 | 0.001 | 17.40 | - | CP 304; low S | - | - | - | - | - |
| C1-03 | 8.12 | 0.50 | 0.038 | 0.002 | 1.00 | 0.060 | 0.060 | 18.11 | - | CP 304; low S; high Ni | 802 | 833 | 3.38 | 5.27 | 0 |
| C3-03 | 8.91 | 0.46 | 0.019 | 0.004 | 1.81 | 0.016 | 0.083 | 18.55 | - | CP 304; low S | 796 | 826 | 5.05 | 7.31 | 26 |
| C21-03 | 10.24 | 0.51 | 0.034 | 0.001 | 1.19 | 0.060 | 0.020 | 16.28 | - | CP 304; low S; high Ni | 893 | 924 | 1.89 | 4.85 | 0 |
| L8-03 | 10.20 | 0.15 | 0.093 | 0.010 | 1.85 | 0.041 | 0.001 | 18.30 | - | CP 304; low S | - | - | - | - | - |

[a]Test at 289°C and a strain rate of 1.65 x $10^{-7}$ $s^{-1}$ in simulated BWR-like water; DO ≈8 ppm.
[b]HP = high purity, CP = commercial purity.

### 3.1.4 Effect of Sulfur

Initial results obtained for specimens irradiated to ≈2.0 x $10^{21}$ n $cm^{-2}$ (≈3 dpa) indicate that S is the major culprit impurity that increases the susceptibility of austenitic SSs to IASCC. As shown in Fig. 15, Types 304 and 304L SS that contain ≤0.002 wt.% S exhibited negligible susceptibility to IASCC (i.e., negligible % IGSCC), whereas heats with ≥0.003 wt.% S exhibited high susceptibility to IASCC, especially low–C Types 304L or 316L SSs. This observation is consistent with the results obtained for specimens irradiated to ≈0.9 x $10^{21}$ n $cm^{-2}$, reported in Ref. 71. Figure 15 shows a summary plot of the effect of S for three fluence levels. The S contents in the figure are vendor–supplied bulk contents. Sulfur content is commonly measured per ASTM Standard E–1019 "Standard Test Method for Determination of Carbon, Sulfur, Nitrogen, and Oxygen in Steel and in Iron, Nickel, and Cobalt Alloys," usually in the range of 0.002 to 0.035 wt.% using the method of combustion–infrared absorption. Accuracy of ≤0.005 wt.% S requires good calibrated standards.

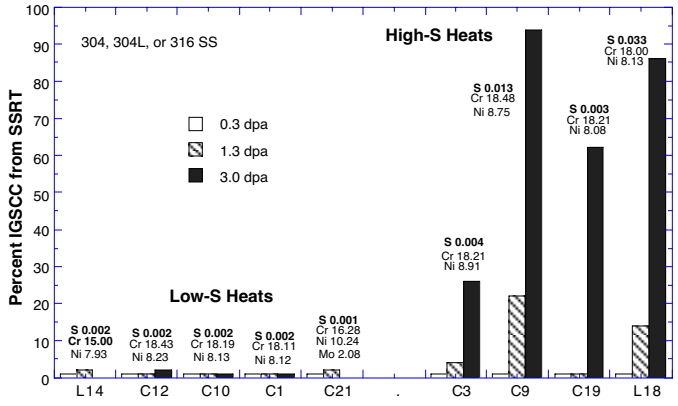


Figure 15.
Effect of S on susceptibility of Types 304, 304L, and 316 SS to IGSCC after irradiation to ≈0.3, 0.9, and 2.0 x $10^{21}$ n $cm^{-2}$ (E > 1 MeV) (≈0.43,1.3, and 3 dpa); alloys containing low concentrations of S (≤0.002 wt.%) are resistant to IGSCC but alloys containing higher concentrations of S are susceptible.

The effects of S content and fluence on the susceptibility to IASCC were examined in more detail for two commercial heats of Type 304 SS (i.e., Heat C12, S content 0.002 wt.%, and Heat C9, S content 0.013 wt.%). Other than S, the composition of the solution–annealed and

water-quenched steels was virtually identical (see Table 7). As fluence increased from ≈0.3 to 2.0 x $10^{21}$ n $cm^{-2}$ (E > 1 MeV), Heat C12, which contained 0.002 wt.% S, exhibited negligible susceptibility to IASCC, whereas Heat C9, which contained 0.013 wt.%, exhibited increasingly high susceptibility to IASCC (see Fig. 16).

Table 7 IASCC behavior at three fluence levels[a] of low- and high-sulfur commercial heats C12 and C9 of Type 304 SS that are otherwise of virtually identical composition

| Heat | Composition (wt.%) | | | | | | | | %IGSCC | %IGSCC | %IGSCC |
|---|---|---|---|---|---|---|---|---|---|---|---|
| ID | Ni | Si | P | S | Mn | C | N | Cr | at 0.3e21 | at 0.9e21 | at 2.0e21 |
| C12-03 | 8.23 | 0.47 | 0.018 | 0.002 | 1.00 | 0.060 | 0.070 | 18.43 | 0 | 0 | 2 |
| C9-03 | 8.75 | 0.39 | 0.013 | 0.013 | 1.72 | 0.062 | 0.065 | 18.48 | 0 | 22 | 94 |

[a]0.3, 0.9, and 2.0 x $10^{21}$ n $cm^{-2}$ (E > 1 MeV).

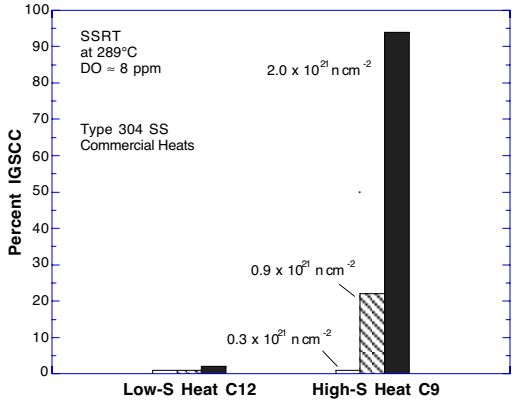


Figure 16.
Effect of fluence on susceptibility to IGSCC of commercial heats C12 and C9 of Type 304 SS that contain low and high levels of S, respectively. Note that low-S Heat C12 is resistant to IASCC and that the high-S Heat C9 is susceptible to IASCC.

Following irradiation to ≈2.5 x $10^{21}$ n $cm^{-2}$ (E > 1 MeV) in a BWR, a result similar to that in Fig. 16 has also been observed by Kasahara et al.[57] for two commercial heats of Type 316L SS; their results are summarized in Table 8 and Fig. 17.

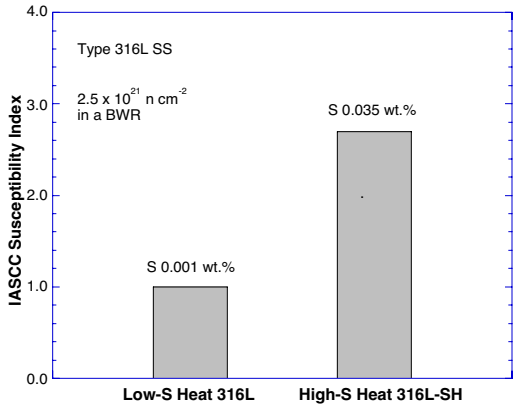


Figure 17.
Effect of sulfur on susceptibility to IASCC of two commercial heats of Type 316L SS that contain low and high levels of S (Ref. 57). IASCC susceptibility index is defined by the number of crack lines crossing three geometrical lines drawn along the tube circumference 5 mm apart near the center of the tube length.

Table 8. IASCC behavior[a] of low- and high-sulfur heats of Type 316L SS that are otherwise of virtually identical composition (Kasahara et al., Ref. 57)

| Heat | Composition (wt.%) | | | | | | | | IASCC |
|---|---|---|---|---|---|---|---|---|---|
| ID | Ni | Si | P | S | Mn | C | N | Cr | Index |
| 316L | 12.36 | 0.48 | 0.026 | 0.001 | 2.20 | 0.017 | 0.032 | 16.90 | 1.0 |
| 316L-SH | 12.10 | 0.49 | 0.020 | 0.035 | 2.10 | 0.015 | 0.038 | 17.11 | 2.7 |

[a]Irradiated to 2.5 x $10^{21}$ n $cm^{-2}$ (E > 1 MeV) in a BWR at 288°C.

Tsukada and Miwa.[59] have reported a result similar to those in Figs. 16 and 17 for a high-purity laboratory heat of Type 304L SS irradiated to ≈0.7 x $10^{21}$ n $cm^{-2}$ (E > 1 MeV) in He at ≈240°C in a material-testing reactor; their results are summarized in Table 9 and Fig. 18.

Table 9. IASCC behavior[a] of low- and high-sulfur heats of Type 304L SS that are otherwise of virtually identical composition (Tsukada and Miwa, Ref. 59)

| Heat | Composition (wt.%) | | | | | | | | |
|---|---|---|---|---|---|---|---|---|---|
| ID | Ni | Si | P | S | Mn | C | N | Cr | %IGSCC |
| HP | 12.27 | 0.01 | 0.001 | 0.0014 | 1.36 | 0.003 | 0.0014 | 18.17 | 51 |
| HP+S | 12.47 | 0.03 | 0.001 | 0.0318 | 1.41 | 0.002 | 0.0012 | 18.32 | 89 |

[a]Irradiated to 0.67 x $10^{21}$ n $cm^{-2}$ (E > 1 MeV) in JRR–3 in helium at 240°C.

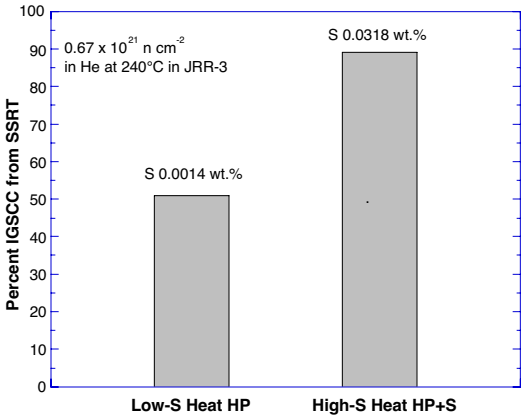


Figure 18.
Effect of sulfur on susceptibility to IGSCC of two high-purity laboratory heats of Type 304L SS that contain low and high levels of S (Ref. 59).

The observations summarized in Figs. 15–18 are consistent with each other and indicate that, for Types 304, 304L, 316, and 316L SS, a high concentration of S is detrimental and that S impurity in an austenitic SS plays a key role in IASCC.

### 3.1.5 Effect of Delta Ferrite

In spite of high S content (≈0.028 wt.% S), Laboratory Alloy L5, which contained a high concentration of Cr (≈21 wt.%) and ≈3 vol.% delta ferrite, exhibited excellent resistance to IASCC after irradiation to ≈0.9 x $10^{21}$ n $cm^{-2}$ and ≈2.0 x $10^{21}$ n $cm^{-2}$ (E > 1 MeV); this is shown in Fig. 19. In contrast, other Type 304 SS heats in Fig. 19 that contained high concentrations of S but no delta ferrite exhibited high susceptibility to IASCC, as reflected in IGSCC data.

As shown in the optical photomicrograph in Fig. 20, the IASCC-resistant Alloy L5 contained small globules of delta ferrite in high number density. It appears that the mechanism of how the small amount of delta ferrite suppressed the susceptibility to IASCC in Heat L5 can be explained by the effect of delta ferrite on the distribution of S in the alloy. As shown in the equilibrium Fe-S diagram in Fig. 21, the solubility limit of S is several times higher in the δ ferrite than in the austenitic (γ) phase. At ≈1365°C, the solubility limits in δ ferrite and austenite are, 0.18 and 0.05 wt.%, respectively. Therefore, during the process of ingot melting, solidification, and cooling, S atoms will migrate toward and be incorporated in the delta ferrite globules that act as trapping sites for S atoms. Likewise, segregation of S atoms to austenite grain boundaries during irradiation may be suppressed because of the

presence of delta ferrite globules and austenite ferrite phase boundaries. As a consequence, the concentration of S on austenite grain boundaries is expected to be low, and the susceptibility to IASCC (i.e., IGSCC along austenite grain boundaries) is suppressed in irradiated steels that contain delta ferrite even in small volume fraction. If the volume fraction of delta ferrite is too large, however, significant embrittlement of the ferrite phase could lead to unacceptable degradation of the fracture toughness of irradiated steel. Explanation based on this model needs, however, to be confirmed by further investigations, e.g., AES analysis of S on grain boundaries and quantitative metallography of ferrite and MnS inclusions.

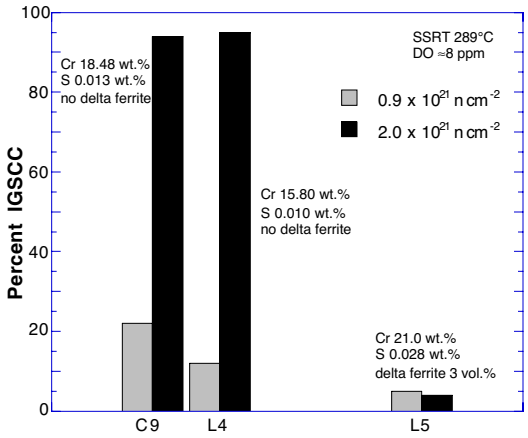


Figure 19.
Effects of delta ferrite on susceptibility to IASCC, as reflected in IGSCC data, of heats that contain high concentrations of sulfur. Note that Heat L5, which contains ≈3 vol.% δ ferrite, is resistant to IASCC but Heats C9 and L18 that contain no delta ferrite are highly susceptible to IASCC.

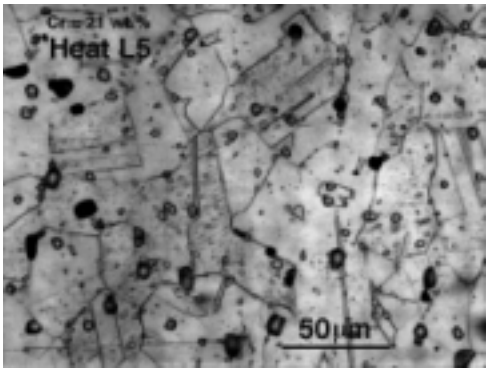


Figure 20.
Optical photomicrograph of IASCC-resistant high-Cr Alloy L5 (21wt.% Cr), showing twins and 3– to 15–µm–diameter globules of delta ferrite.

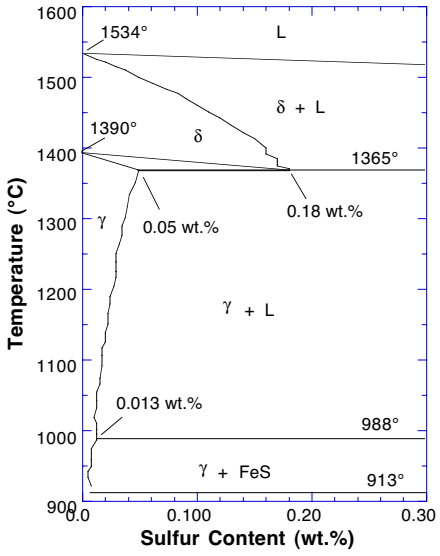


Figure 21.
Fe-rich side of Fe-S phase diagram, from M. Hansen, “Constitution of Binary Alloys,” McGraw Hill, New York, NY, 1958, pp. 704-707.

Figure 22 shows a predominantly intergranular–fracture surface morphology in Type 304 SS Heats C9 and L18 that contain high concentrations of S and were irradiated to ≈3 dpa (Fig. 19). The figure also shows a predominantly ductile-dimple fracture surface morphology in Alloy L5 that contains high concentrations of S and ≈3 vol.% δ ferrite.

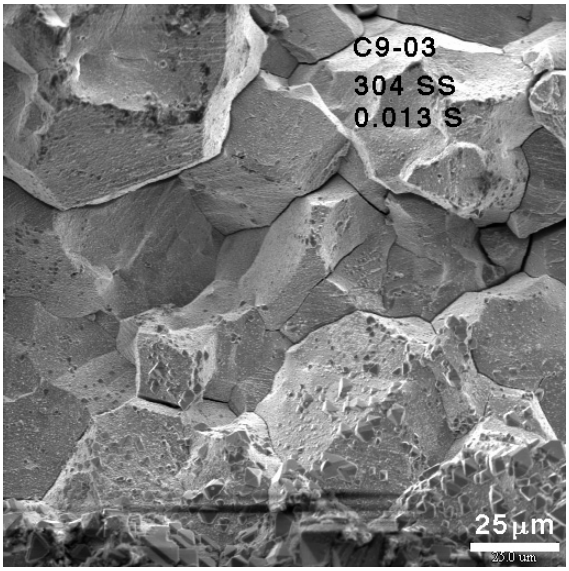


(a)

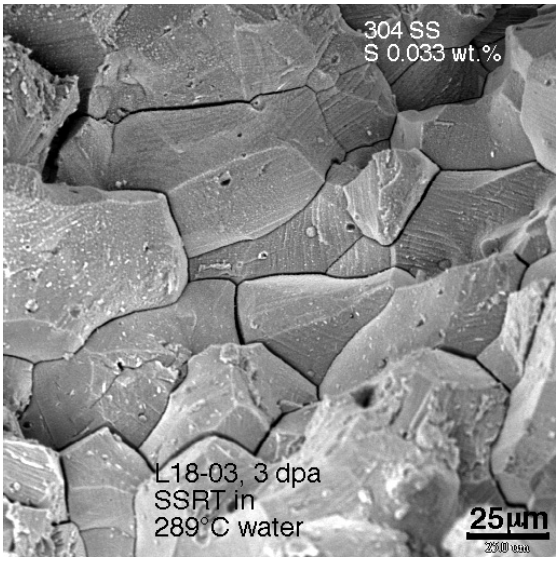


(b)

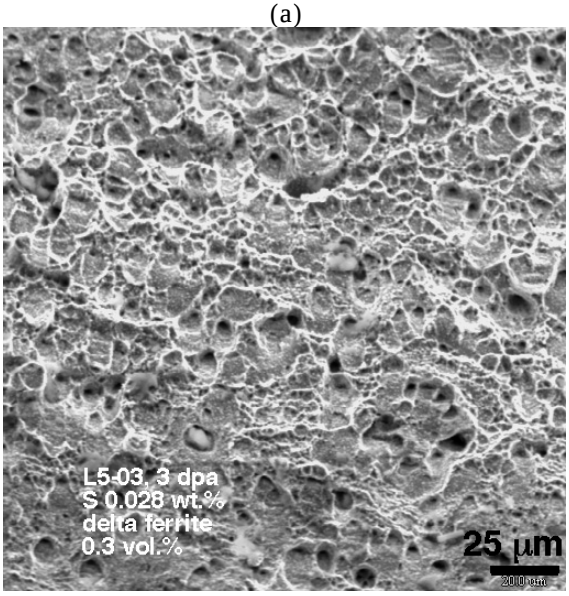


(c)

Figure 22.
Fracture surface morphology of IASCC-susceptible high-S Heats (a) C9 (0.013 wt.% S) and (b) L18 (0.033 wt.% S), and (c) IASCC-resistant Alloy L5 that contains high concentration of S (0.028 wt.% S) and ≈3 vol.% δ ferrite. All specimens were irradiated to ≈2 x $10^{21}$ n $cm^{-2}$ (≈3 dpa).

## 3.2 Crack Growth Rate Test of Austenitic Stainless Steels Irradiated in the Halden Reactor (E. E. Gruber and O. K. Chopra)

### 3.2.1 Introduction

Austenitic SSs are used extensively as structural alloys in reactor pressure vessel internal components because of their high strength, ductility, and fracture toughness. Fracture of these steels occurs by stable tearing at stresses well above the yield stress, and tearing instabilities require extensive plastic deformation. However, exposure to neutron irradiation for extended periods changes the microstructure and degrades the fracture properties of these steels. Irradiation leads to a significant increase in yield strength and reduction in ductility and fracture resistance of austenitic SSs.[72–74]

The purpose of the tests of Task 2 is to obtain fracture toughness and CGR data that are applicable to irradiated austenitic SS internal components of BWRs. Tests are being conducted on several commercial heats of Type 304 SS that were irradiated to fluence levels of ≈0.3, 0.9, and 2.0 x $10^{21}$ n $cm^{-2}$ (E > 1 MeV) (≈0.45, 1.35, and 3.0 dpa) at ≈288°C in a He environment in the Halden boiling heavy water reactor. Fracture toughness J–R curve tests have been completed on irradiated wrought austenitic SSs.[75–77] The current effort is focused on CGR tests on nonirradiated specimens in high–purity water at 289°C to establish the test procedure and conditions that will be used for the tests on irradiated materials. The intent of these tests is to gain a better understanding of environmentally assisted cracking and not to just determine CGRs; under certain loading conditions the dominant mechanism is fatigue. Crack growth tests have been completed on two heats of thermally aged CF8M cast SS and a 50% cold–worked (CW) Type 316LN SS in high–purity water at 289°C.

### 3.2.2 Experimental

Tests were performed in accordance with ASTM E–647 “Standard Test Method for Measurement of Fatigue Crack Growth Rates” and ASTM E–1681 “Standard Test Method for Determining a Threshold Stress Intensity Factor for Environment–Assisted Cracking of Metallic Materials under Constant Load.” All tests were conducted under load control by either a triangular or sawtooth waveform. A mechanical test facility outside the hot cell was used for the tests. The facility consists of a test frame mounted on a portable wheeled cart, a recirculating water system, Instron 8500+ electronic control console, hydraulic pump, temperature–control units, DC potential rig, a PC for data acquisition and DC potential measurements, and a strip chart recorder. A detailed description of the facility has been presented earlier.[77]

The composition and tensile strength of the various materials are presented in Table 10. The tests were performed on 1/4–T compact tension (CT) specimens; configuration of the specimens is shown in Fig. 23. The initial crack length of these specimens was smaller than that of the irradiated specimens, i.e., 4 mm for the nonirradiated and 6 mm for irradiated specimens. Because the specimens were side grooved, effective thickness $B_{eff}$ was used to calculate the stress intensity factor range ΔK. $B_{eff}$ is defined as

$$B_{eff} = (B\ B_N)^{0.5}, \quad (5)$$

where B is the specimen thickness and $B_N$ is net specimen thickness or distance between the roots of the side grooves. The stress intensity factor range ΔK was calculated as follows:

$$\Delta K = \frac{\Delta P}{(B B_N W)^{1/2}} \frac{\left(2 + \frac{a}{W}\right)}{\left(1 - \frac{a}{W}\right)^{3/2}} f\left(\frac{a}{W}\right) \tag{6}$$

$$\Delta P = P_{max} - P_{min} \qquad \text{for } R > 0 \tag{7}$$

$$f\left(\frac{a}{W}\right) = 0.886 + 4.64\left(\frac{a}{W}\right) - 13.32\left(\frac{a}{W}\right)^2 + 14.72\left(\frac{a}{W}\right)^3 - 5.6\left(\frac{a}{W}\right)^4 . \tag{8}$$

Table 10. Composition (wt.%) of cast and wrought austenitic SSs for crack growth tests

| Alloy Type | Heat ID[a] | Cr | Mo | Ni | Mn | Si | C | N | P | S | Meas. Ferrite (%) | Yield Stress[b] (MPa) | Ultimate Stress[b] (MPa) |
|---|---|---|---|---|---|---|---|---|---|---|---|---|---|
| CF8M | 75 | 20.86 | 2.58 | 9.12 | 0.53 | 0.67 | 0.065 | 0.052 | 0.022 | 0.012 | 28 | 208 | 612 |
| CF8M | 4331 | 20.75 | 2.58 | 10.05 | 0.76 | 1.17 | 0.044 | 0.040 | 0.022 | 0.001 | 21 | 193 | 628 |
| 316LN | 18474 | 16.10 | 2.04 | 10.30 | 1.80 | 0.50 | 0.012 | 0.120 | 0.018 | 0.004 | – | 825 | 897 |

[a]Heat 75 was aged 10,000 h at 400°C, Heat 4331 aged 700 h at 400°C, and Heat 18474 was cold worked 50%.
[b]Measured at 290°C for Heats 75 and 18474 and at 300°C for Heat 4331.

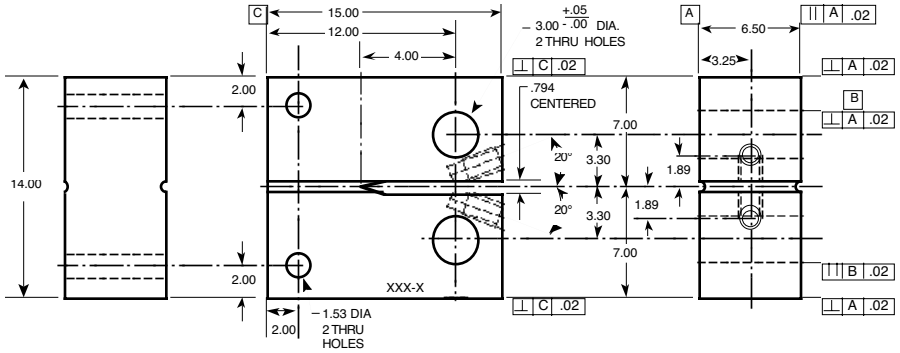


Figure 23. Configuration of compact–tension specimen for this study (dimensions in mm).

where $P_{max}$ and $P_{min}$ are maximum and minimum applied load, a is crack length, and W is the specimen width. Also, because a modified configuration of a disc–shaped CT specimen was used in the present study, crack length was calculated from correlations that were developed from the best–fit of the experimental data for normalized crack length and normalized DC potential. The normalized crack length a/W is expressed as

$$\left(\frac{a}{W}\right) = \left[0.28887\left(\frac{U}{U_0} - 0.5\right)\right]^{0.34775} , \tag{9}$$

where U and $U_0$ are current and reference crack potentials. The final crack size was marked by fatigue cycling at room temperature. The specimens were then fractured and the initial (i.e., fatigue precrack) and final (test) crack lengths of both halves of the fractured specimen were

measured optically. The crack lengths were determined by the 9/8 averaging technique, i.e., the two near–surface measurements were averaged and the resultant value was averaged with the remaining seven measurements.

The CGR test results were validated in accordance with the specimen size criteria of ASTM E–1681 and E–647. To ensure that the experimental data obtained under various specimen geometry, thickness, and loading conditions can be compared with each other and applied to reactor components, the specimen size criteria require that the plastic zone at the tip of a fatigue crack be small relative to the specimen geometry. For threshold K measurements, ASTM E–1681 requires that

$$B_{eff}, a, \text{ and } (W-a) \geq 2.5\,(K/\sigma_{ys})^2, \tag{10}$$

where $\sigma_{ys}$ is the yield strength of the material. For tests on irradiated material, side grooved specimens are strongly recommended, with a depth for each side groove between 5–10% of the specimen thickness. The threshold K is the highest value of K at which crack growth is not observed for a specified combination of material and environmental conditions and where the specimen size is sufficient to meet the requirements for plane strain. For valid CGR results, ASTM 647 requires that

$$(W-a) \geq (4/\pi)\,(K/\sigma_{ys})^2. \tag{11}$$

For high–strain–hardening materials, i.e., materials with an ultimate–to–yield–strength ratio $(\sigma_{ult}/\sigma_{ys}) \geq 1.3$, both criteria allow the use of effective yield strength (or flow strength), defined as $\sigma_f = (\sigma_{ult} + \sigma_{ys})/2$. For nonirradiated materials, the K/size criteria are generally conservative, violating them by a small amount, e.g., 20–30% in K, is acceptable.

### 3.2.3 Results

The crack growth results, as well as the environmental and loading conditions, for Specimen Y4–09 of CF8M SS Heat 4331, Specimen 75–09T of CF8M SS Heat 75, and Specimen 184–46 of Type 316LN SS Heat 18474, are given in Tables 11–13, respectively. The ECPs of a Pt electrode and a SS electrode were monitored continuously during these tests,

Table 11. Crack growth results for thermally aged CF8M cast SS Heat 4331[a] in high–purity water at 289°C

| Test Period | Test Time, h | $O_2$ [b] Conc., ppb | Cond. [b] at 25°C, µS/cm | ECP [b] mV (SHE) Pt | ECP [b] mV (SHE) Steel | Load Ratio | Rise Time, s | $K_{max}$,[c] MPa·m$^{1/2}$ | ΔK, MPa·m$^{1/2}$ | Growth Rate, m/s |
|---|---|---|---|---|---|---|---|---|---|---|
| | 24 | | – | – | – | 0.70 | 12 | 22.8 | 6.8 | – |
| | 80 | 164 | – | 41 | 74 | 0.71 | 60 | 23.7 | 7.0 | – |
| 1a | 150 | 222 | – | 83 | 65 | 0.71 | 60 | 27.1 | 8.0 | 4.99E-10 |
| 1b | 230 | 290 | – | 106 | 74 | 0.71 | 60 | 28.6 | 8.4 | 7.86E-10 |
| 1c | 310 | 328 | – | 130 | 86 | 0.71 | 60 | 30.7 | 9.0 | 1.03E-09 |
| 2a | 380 | 380 | 0.83 | 137 | 81 | 0.70 | 300 | 31.6 | 9.5 | 3.83E-10 |
| 2b | 500 | 396 | – | 155 | 105 | 0.70 | 300 | 33.2 | 10.0 | 4.68E-10 |
| 3 | 650 | 410 | – | 180 | 135 | 0.70 | 1000 | 34.4 | 10.4 | 2.51E-10 |
| 4 | 1,058 | 440 | 0.43 | 190 | 171 | 0.70 | 5000 | 35.5 | 10.8 | 8.58E-11 |

[a]Specimen Y4–09 of Heat 4331 of CF8M cast SS thermally aged for 700 h at 400°C.
[b]Represents values in the effluent. Feedwater pH at room temperature was 6.5.
[c]Stress intensity, $K_{max}$, values at the end of the time period.

Table 12. Crack growth results for thermally aged CF8M cast SS Heat 75[a] in high–purity water at 289°C

| Test Period | Test Time, h | $O_2$ [b] Conc., ppb | Cond. [b] at 25°C, µS/cm | ECP [b] mV (SHE) Pt | ECP [b] mV (SHE) Steel | Load Ratio | Rise Time, s | $K_{max}$,[c] MPa·m$^{1/2}$ | ΔK, MPa·m$^{1/2}$ | Growth Rate, m/s |
|---|---|---|---|---|---|---|---|---|---|---|
| | 2 | 380 | 0.77 | 161 | 160 | 0.20 | – | 20.0 | 16.0 | - |
| | 10 | 380 | 0.77 | 161 | 160 | 0.71 | – | 25.9 | 7.5 | - |
| 1a | 35 | 380 | 0.77 | 161 | 160 | 0.71 | 60 | 27.2 | 8.0 | 2.04E-09 |
| 1b | 48 | 380 | 0.77 | 160 | 165 | 0.71 | 60 | 28.5 | 8.4 | 3.47E-09 |
| 1c | 72 | 380 | 0.77 | 160 | 165 | 0.71 | 60 | 34.4 | 10.1 | 8.11E-09 |
| 1d | 83 | 380 | 0.77 | 160 | 165 | 0.71 | 60 | 39.7 | 11.6 | 1.04E-08 |
| | 168 | 350 | 0.77 | 173 | 163 | 1.00 | – | 28.2 | – | 4.85E-10 |
| 2 | 194 | 350 | 0.77 | 173 | 163 | 0.71 | 60 | 25.3 | 7.3 | 5.06E-09 |
| 3 | 238 | 380 | 0.77 | 169 | 176 | 0.70 | 1000 | 26.3 | 7.9 | 5.35E-10 |
| 4a | 280 | 450 | 0.77 | 187 | 192 | 0.70 | 5000 | 21.7 | 6.6 | 6.71E-11 |
| 4b | 408 | 450 | 0.67 | 177 | 204 | 0.70 | 5000 | 21.8 | 6.6 | 1.42E-11 |
| 5a | 450 | 450 | 0.67 | 177 | 204 | 0.70 | 1000 | 25.5 | 7.7 | 9.70E-11 |
| 5b | 480 | 600 | 0.59 | 199 | 212 | 0.70 | 1000 | 26.1 | 7.9 | 6.57E-10 |
| 5c | 490 | 600 | 0.59 | 199 | 212 | 0.70 | 1000 | 26.8 | 8.1 | 9.02E-10 |

[a]Specimen 75–09T of Heat 75 of CF8M cast SS thermally aged for 10,000 h at 400°C.
[b]Represents values in the effluent. Feedwater pH at room temperature was ≈6.5.
[c]Stress intensity, $K_{max}$, values at the end of the time period.

Table 13. Crack growth results for 50% cold–worked Type 316LN SS Heat 18474[a] in high–purity water at 289°C

| Test Period | Test Time, h | $O_2$ [b] Conc., ppb | Cond. [b] at 25°C, µS/cm | ECP [b] mV (SHE) Pt | ECP [b] mV (SHE) Steel | Load Ratio | Rise Time, s | $K_{max}$,[c] MPa·m$^{1/2}$ | ΔK, MPa·m$^{1/2}$ | Growth Rate, m/s |
|---|---|---|---|---|---|---|---|---|---|---|
| | 10 | 610 | – | 212 | 212 | 0.29 | | 26.1 | 18.5 | |
| 0 | 20 | 610 | – | 204 | 211 | 0.29 | 30 | 31.0 | 22.0 | 1.80E-08 |
| 1 | 25 | 610 | – | 204 | 211 | 0.49 | 30 | 31.1 | 15.8 | 1.08E-08 |
| 2 | 92 | 560 | 0.63 | 211 | 211 | 0.69 | 1,000 | 31.2 | 9.6 | 6.75E-10 |
| 3 | 140 | 530 | – | 215 | 210 | 0.69 | 300 | 31.8 | 9.8 | 1.98E-09 |
| 4 | 149 | 530 | – | 215 | 210 | 0.69 | 60 | 31.8 | 9.8 | 4.37E-09 |
| 5a | 245 | 480 | – | 222 | 212 | 0.69 | 5,000 | 32.5 | 10.0 | 5.45E-10 |
| 5b | 290 | 480 | – | 221 | 213 | 0.69 | 5,000 | 32.6 | 10.1 | 6.02E-10 |
| 6 | 430 | 550 | – | 226 | 217 | 1.00 | – | 32.4 | – | 3.17e-10 |
| 7a | 457 | 550 | – | 226 | 217 | 0.69 | 5,000 | 32.5 | 10.1 | 1.44E-09 |
| 7b | 478 | 550 | – | 224 | 218 | 0.69 | 5,000 | 32.4 | 10.1 | 6.88E-10 |
| | 599 | 40 | – | -482 | -507 | 1.00 | – | 11.5 | – | – |
| 8a | 710 | 30 | – | -477 | -594 | 0.69 | 5,000 | 33.1 | 10.3 | 1.26E-10 |
| 8b | 840 | 36 | – | -483 | -604 | 0.69 | 5,000 | 33.1 | 10.3 | 7.08E-11 |

[a]Specimen 184–46 of Heat 18474 of 50% CW Type 316LN SS.
[b]Represents values in the effluent. Feedwater pH at room temperature was 6.5.
[c]Stress intensity, $K_{max}$, values at the end of the time period.

whereas the water DO level and conductivity were determined periodically; the values are listed in the tables. For these specimens, the change in crack length and $K_{max}$ with time is shown in Figs. 24–26 and photomicrographs of the fracture surfaces are shown in Fig. 27. All specimens were precracked at R = 0.2 and 0.5 or 1 Hz to allow an ≈1–2–mm crack advance. The CGR tests were conducted at R = 0.7 and a sawtooth waveform with a 12–5000 s rise time and 1 s return time. Significant results from these tests are summarized below.

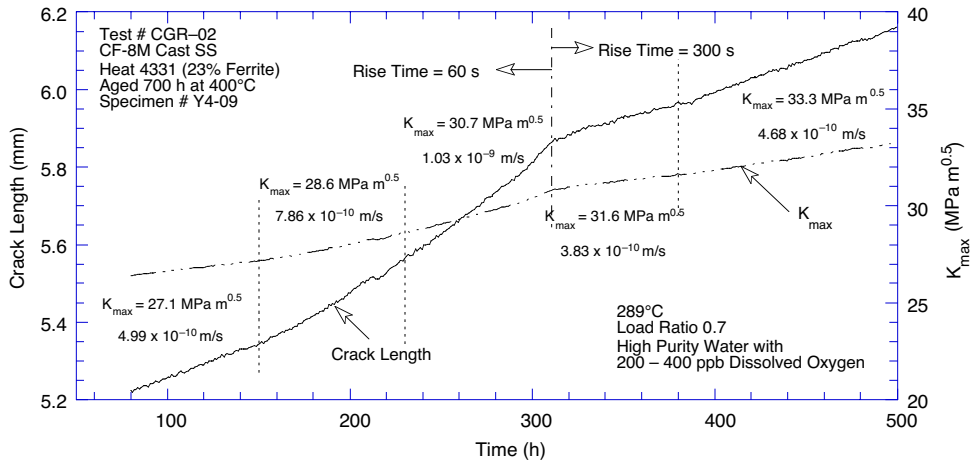


(a)

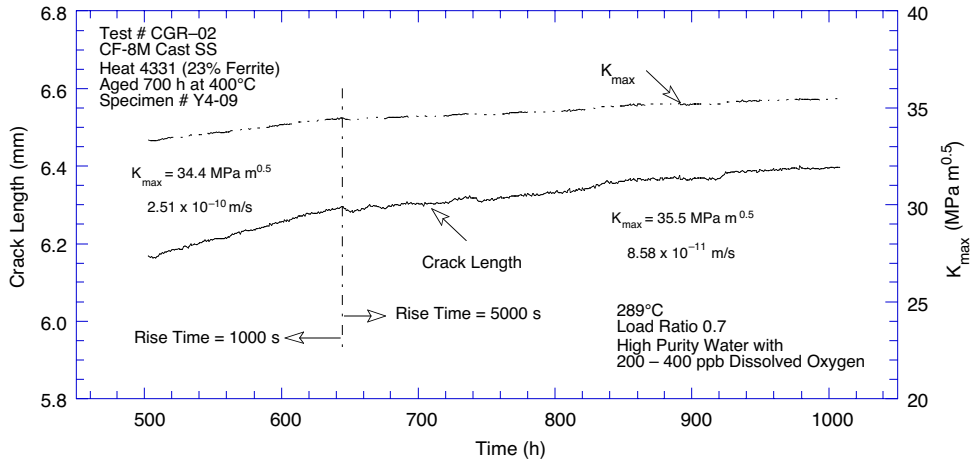


(b)

Figure 24. Crack–length–vs.–time plot for Specimen Y4–09 of thermally aged Heat 4331 of cast SS in high–purity water at 289°C: (a) 80–500 h; (b) 500–1000 h.

Test CGR–02 (Heat 4331 of Cast CF8M SS, Specimen Y4–09)

The CGR test was conducted at a constant load; $K_{max}$ increased from ≈23 to 35 MPa $m^{1/2}$ during the test. For these loading conditions and a material flow stress of 410.5 MPa, the constant in Eq. 11 decreased from 2.0 to 0.8, i.e., the ASTM 647 criterion was not satisfied for Test Periods 2–4. The optically measured precrack and final crack lengths showed very good agreement with the values estimated from the DC potential method. The precrack and final crack lengths, respectively, were 5.08 and 6.42 mm from optical measurements, and 5.04 and 6.40 from DC potential technique. It was necessary to terminate the test because the ceramic clip used for current leads in the DC potential measurements had degraded in the high–temperature water. Other methods of attaching current leads to the test specimen were developed in subsequent tests.

Test CGR–03 (Heat 75 of Cast CF8M SS, Specimen 75–09T)

Crack growth was quite rapid for this test. During the initial 80 h, $K_{max}$ increased from ≈25 to 39 MPa $m^{1/2}$. The excessive crack growth tripped the system hydraulics and the specimen was subject to the autoclave internal pressure of 1300 psi ($K_{max}$ ≈28 MPa $m^{1/2}$).

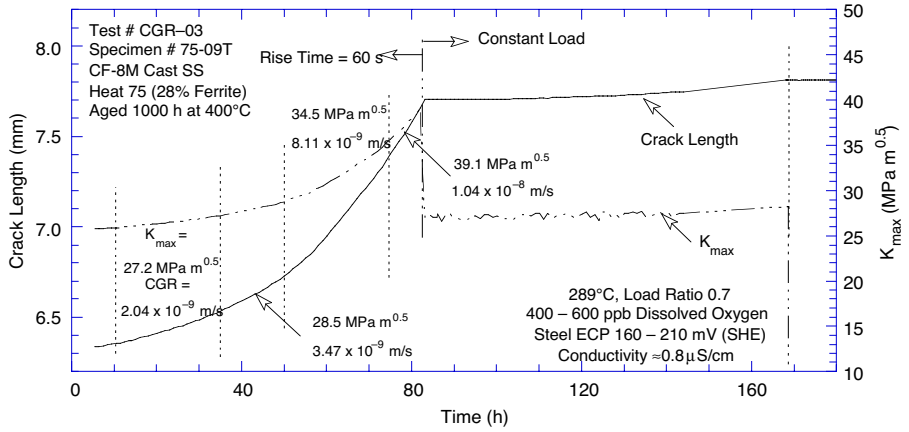


(a)

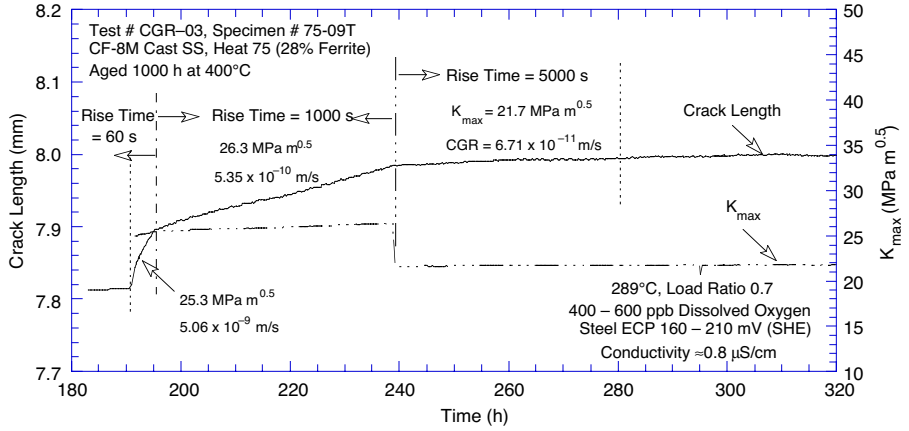


(b)

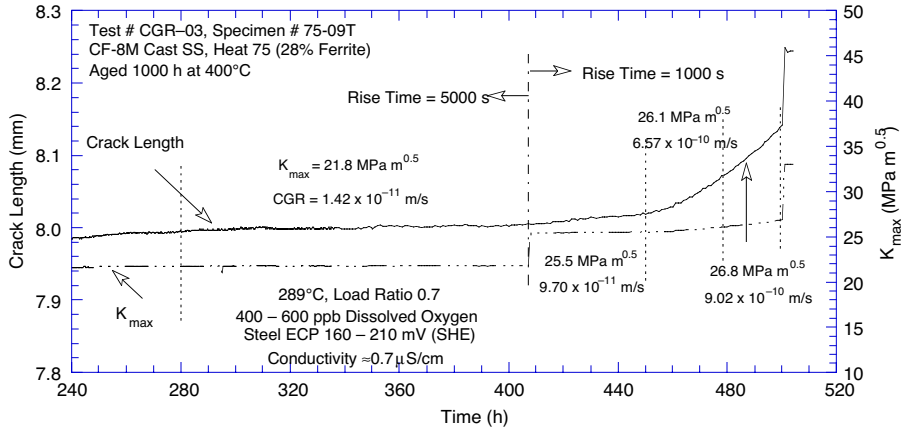


(c)

Figure 25. Crack–length–vs.–time plot for Specimen 75–09T of thermally aged Heat 75 of cast SS in high–purity water at 289°C: (a) 0–180 h; (b) 180–320 h; (c) 240–520 h.

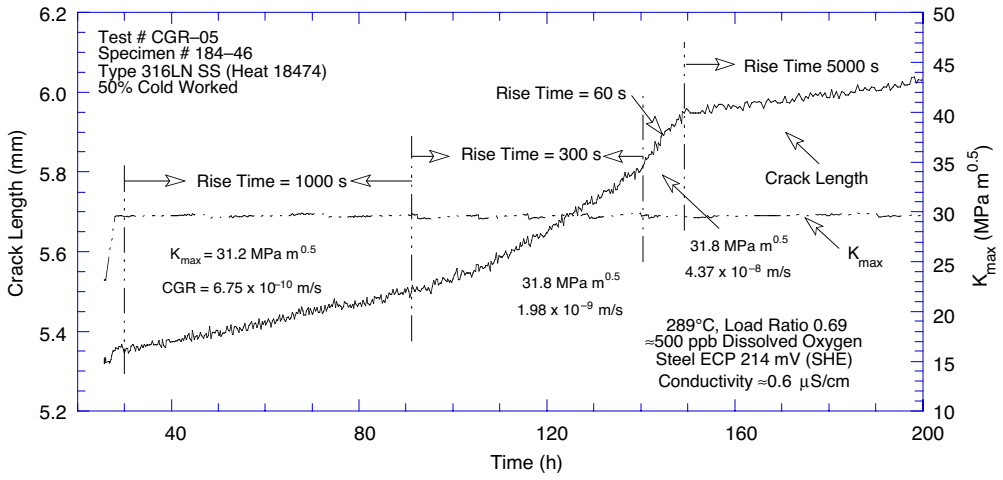


(a)

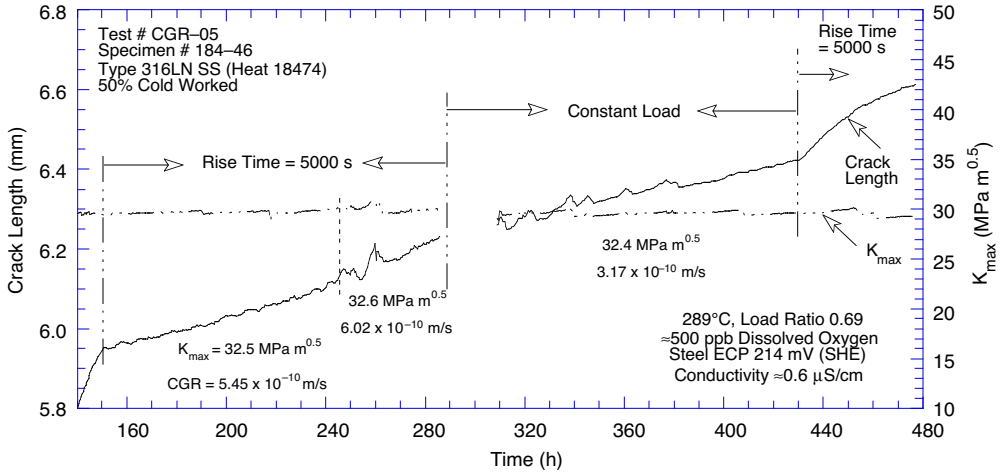


(b)

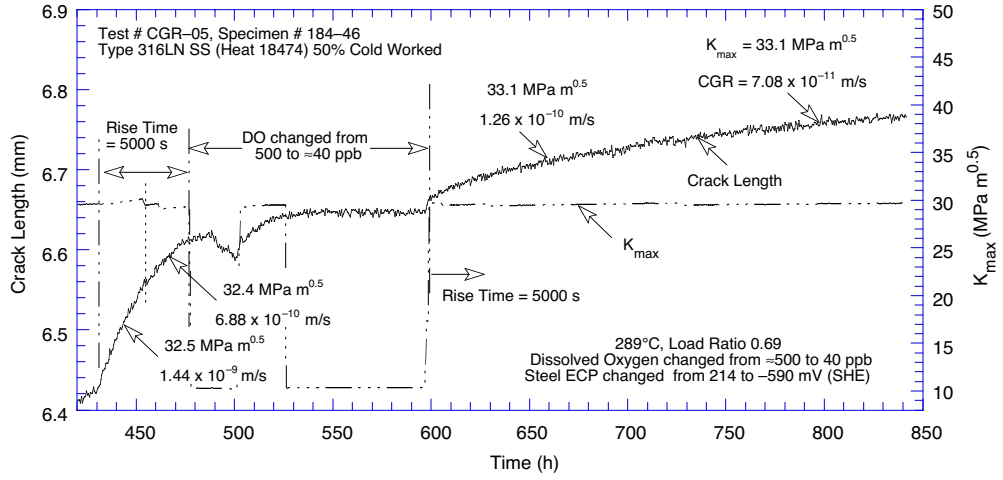


(c)

Figure 26. Crack–length–vs.–time plot for Specimen 184–46 of 50% cold worked Type 316LN SS in high–purity water at 289°C: (a) 0–200 h; (b) 140–480 h; (c) 420–850 h.

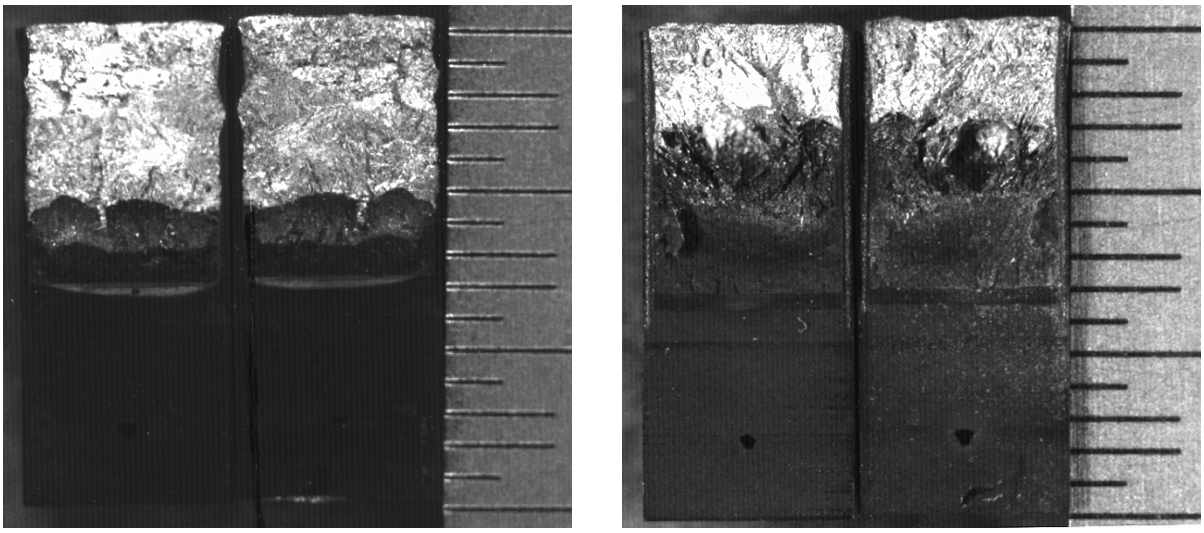

(a) (b)

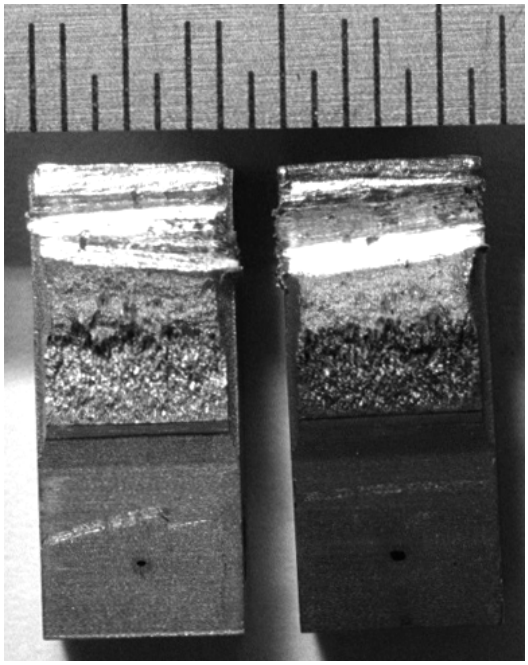

(c)

Figure 27.
Photomicrographs of fracture surface of specimens (a) Y4–09, (b) 75–09T, and (c) 184–46, tested in high–purity water at 289°C.

The load was decreased after the test was restarted; for Test Periods 2–5, $K_{max}$ was between 22 and 26 Mpa $m^{1/2}$. However, the ligament criterion of Eq. 11 was not satisfied for $K_{max}$ values >25 MPa $m^{1/2}$, i.e., for most test periods. The CGR data may be affected by the decrease in $K_{max}$ from 39 to ≈25 MPa $m^{1/2}$. Also, because the grain structure of this material was very coarse, (Fig. 27b), the final crack front was difficult to define accurately. The final crack length from optical measurements was 8.16 and 8.00 mm for the two halves of the fractured specimen; DC potential measurements gave a value of 8.24 mm. A correction of the CGR data was not deemed necessary. These results indicate that load shedding is needed to prevent a large increase in $K_{max}$.

Test CGR–05 (Specimen 184–46)

This test was a dry run for in–cell CGR tests on irradiated specimens. An updated/modified version of computer software for the DC potential system provided a simple and reliable method for monitoring crack length. Test Periods 1–4 were carried out at constant load, during which $K_{max}$ increased from ≈25 to 30 MPa $m^{1/2}$. From Test Period 5 onward, load shedding was successfully used to maintain constant $K_{max}$. Applied load was decreased twice each day at high growth rates and once every 2 or 3 days at very low rates; load shedding was <0.5% of the current value for most cases, and up to 1% for some. The constant in Eq. 11 was >3.6 during the entire test, i.e., the ASTM 647 criterion was satisfied for all test periods.

After ≈480 h, the DO level in water was decreased from ≈550 to <40 ppb by sparging the feedwater tank with pure N cover gas. The change in crack length and ECP of Pt and SS electrodes during the transition is shown in Fig. 28. The results indicate that the environmental conditions of the system take several days to reach a stable condition. For example, although the effluent DO content decreased from 550 to <40 ppb and ECP of the Pt electrode decreased from 225 to –480 mV in a relatively short time, the ECP of the steel electrode took several days to stabilize.

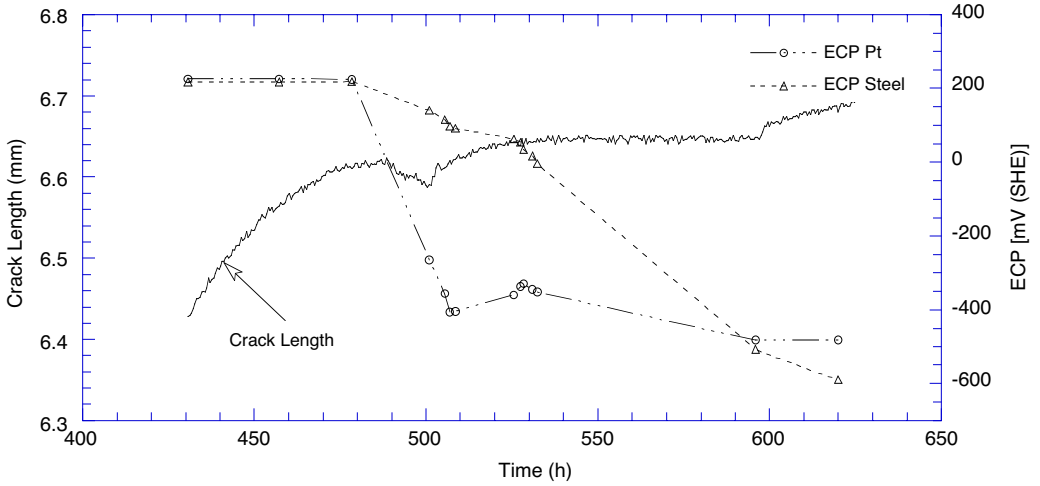


Figure 28. Change in crack length and ECP of Pt and SS electrodes after dissolved oxygen level in feedwater was decreased from ≈550 to <40 ppb.

The average final crack length measured by SEM and that estimated by the DC potential method was 6.76 and 6.38, respectively, i.e., the experimental crack extension was ≈16% lower than the value obtained from SEM measurements. The CGR data were corrected and the results are presented in Table 13 and Fig. 26.

Crack Growth Rate Data

The experimental CGRs for thermally aged CF8M cast SSs and 50% CW Type 316LN SS in water and those predicted in air for the same loading conditions are plotted in Fig. 29. The results obtained earlier on a 1–T CT specimen of the same heat of 50% CW Type 316LN SS and Heat 75 of CF8M cast SS in high–DO water are also included in the figure. The CGRs in air, $\dot{a}_{air}$ (m/s), were determined from the correlations developed by James and Jones;[78] the CGR is given by the expression

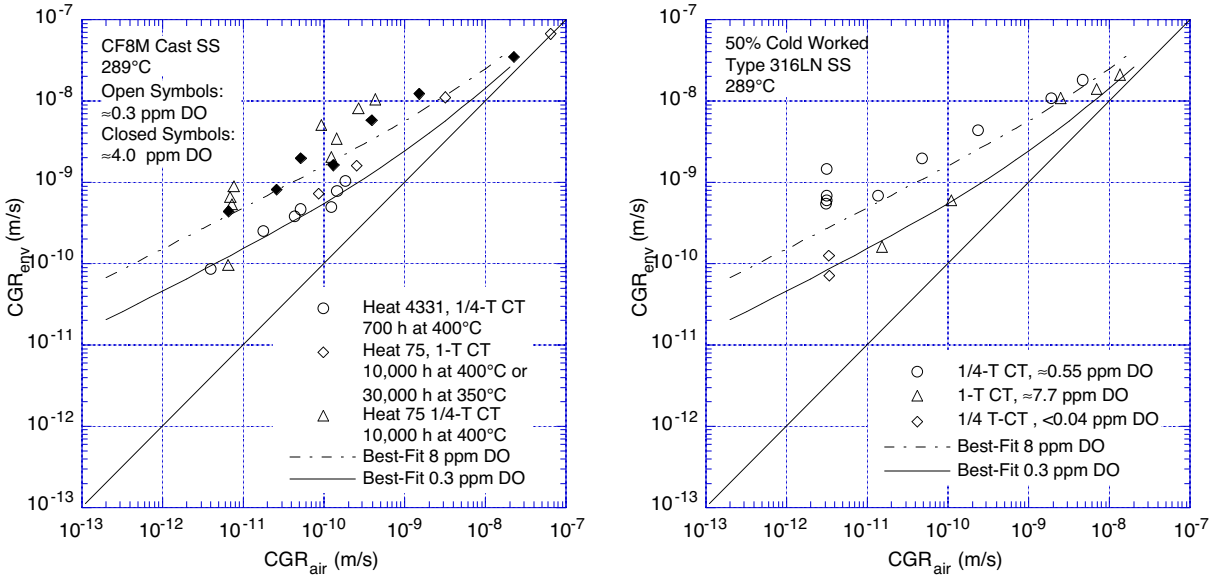


(a) (b)

Figure 29. Crack growth rate data under gentle cycling for (a) thermally aged cast SS and (b) 50% cold–worked Type 316LN SS in high–purity water at 289°C.

$$\dot{a}_{air} = C_{SS}\ S(R)\ \Delta K^{3.3}/T_R\,, \tag{12}$$

where R is the load ratio ($K_{min}/K_{max}$), $\Delta K$ is $K_{max} - K_{min}$ in MPa $m^{1/2}$, $T_R$ is the rise time (s) of the loading waveform, and function S(R) is expressed in terms of the load ratio R as follows:

$$\begin{aligned} S(R) &= 1.0 && R < 0 \\ S(R) &= 1.0 + 1.8R && 0 < R < 0.79 \\ S(R) &= -43.35 + 57.97R && 0.79 < R < 1.0, \end{aligned} \tag{13}$$

and function $C_{SS}$ is given by a third–order polynomial of temperature T (°C), expressed as

$$C_{SS} = 1.9142 \times 10^{-12} + 6.7911 \times 10^{-15}\ T - 1.6638 \times 10^{-17}\ T^2 + 3{,}9616 \times 10^{-20}\ T^3. \tag{14}$$

The CGRs of both thermally aged cast SS and 50% CW wrought SS are enhanced in high–purity high–DO water at 289°C. Figure 29a shows that, for CF8M cast SSs, the experimental CGRs for the 1/4–T CT specimen of Heat 4331 are in good agreement with the data obtained on the 1–T CT specimen of Heat 75. The rates for the 1/4–T CT specimen of Heat 75 are somewhat higher. Please note that the K/size criteria were exceeded for Heat 75, i.e., the experimental values of $K_{max}$ were significantly higher than those allowed by Eqs. 10 and 11. In high–DO water, the CGRs for thermally aged cast SS are best represented by the curve for sensitized austenitic SSs in ≈0.3 ppm DO water,[79] given by the expression

$$\dot{a}_{env} = \dot{a}_{air} + 4.5 \times 10^{-5}\,(\dot{a}_{air})^{0.5}. \tag{15}$$

For the 50% CW Type 316LN SS, environmental enhancement of CGRs for the 1/4–T CT specimens appears to be greater than that observed earlier (solid circles in Fig. 29b) for 1–T CT specimens of the same heat of the material. These differences may be due to high load ratios

used for the 1–T CT specimens; the two data points with $<10^{-9}$ m/s growth rates were obtained at R values of 0.9 and 0.95. Under gentle cycling, CGRs for the CW SS are slightly higher than the CGRs for sensitized austenitic SSs in ≈8 ppm DO water,[79] given by the expression

$$\dot{a}_{env} = \dot{a}_{air} + 1.5 \times 10^{-4} (\dot{a}_{air})^{0.5}. \quad (16)$$

Decreasing the DO level to <40 ppb decreased the CGRs by nearly an order of magnitude.

For the 50% CW Type 316LN SS, the CGR under–constant load conditions in high–DO water at 289°C is plotted in Fig. 30; the maximum stress intensity for the test was within the K/size–validity criteria. Data obtained earlier on 1–T CT specimens of several heats of Types 304 and 316 SS are also included in the figure. In ≈250–ppb–DO water, the CGRs for a 1/4–T CT specimen of 50% CW Type 316LN SS are higher than those for a 1–T CT specimen of sensitized Type 304 SS. Rates for the 1/4–T specimen are comparable to those of sensitized Type 304 SS in very high–DO water (>6000 ppb DO).

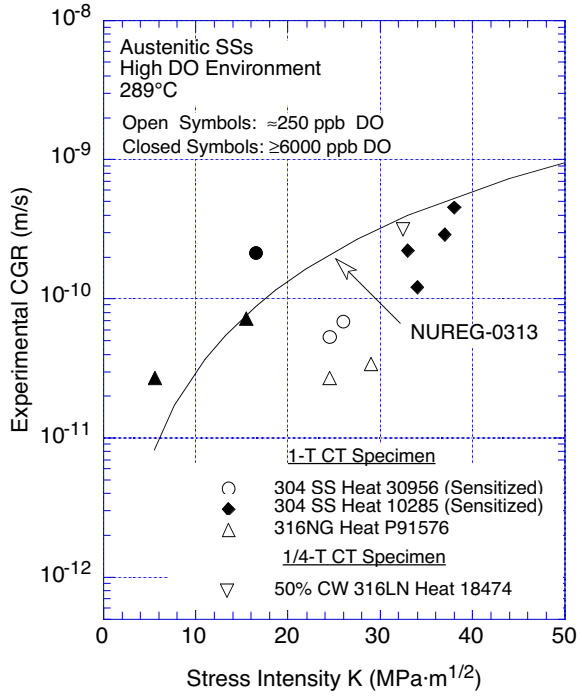


Figure 30.
Stress corrosion cracking data for austenitic stainless steels in high–DO water at 289°C.

## Fracture Morphology

Fractographs of the 1/4–T CT specimens of thermally aged Heat 4331 of CF–8M cast SS and 50% CW Heat 18474 of Type 316LN tested in high–purity water at 289°C during various test periods, are shown in Figs. 31 and 32, respectively. The fracture mode for the cast SS specimen is transgranular; austenite phase exhibits only transgranular facets with a river pattern, whereas the ferrite phase exhibits a faceted river pattern (Fig. 31a) or a rough appearance (Figs. 31c and d).

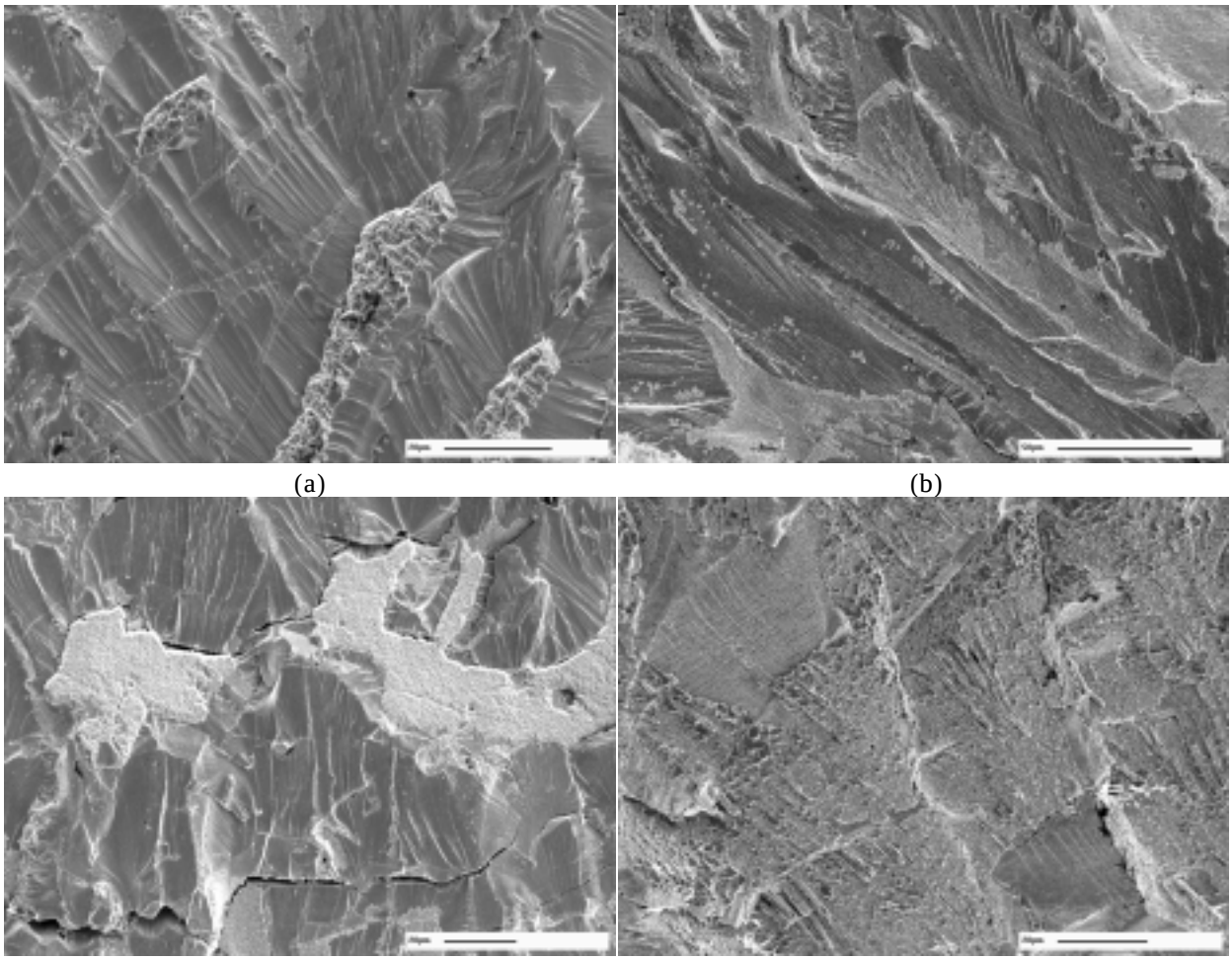

(a) (b)

(c) (d)

Figure 31. Fractographs of CF-8M cast SS Heat 4331 tested in high–purity water at 289°C: (a) Test Period 1, 80–310 h; (b) Test Period 2, 310–500 h; (c) Test Period 3, 500–650 h; (d) Test Period 4, 650–1058 h.

The fracture mode for the 50% CW Type 316LN specimen is also a predominantly transgranular with a well–defined river pattern. It is completely transgranular during the precracking test period. The main feature of the fracture mode during corrosion fatigue test periods, e.g., loading cycles with long rise times, is extensive secondary cracking (Fig. 32b). Intergranular fracture is also observed in some regions (Fig. 32c). Also, slip offsets and crystallographic facets on the fracture surface (Fig. 32e and f) suggest enhanced planar slip.

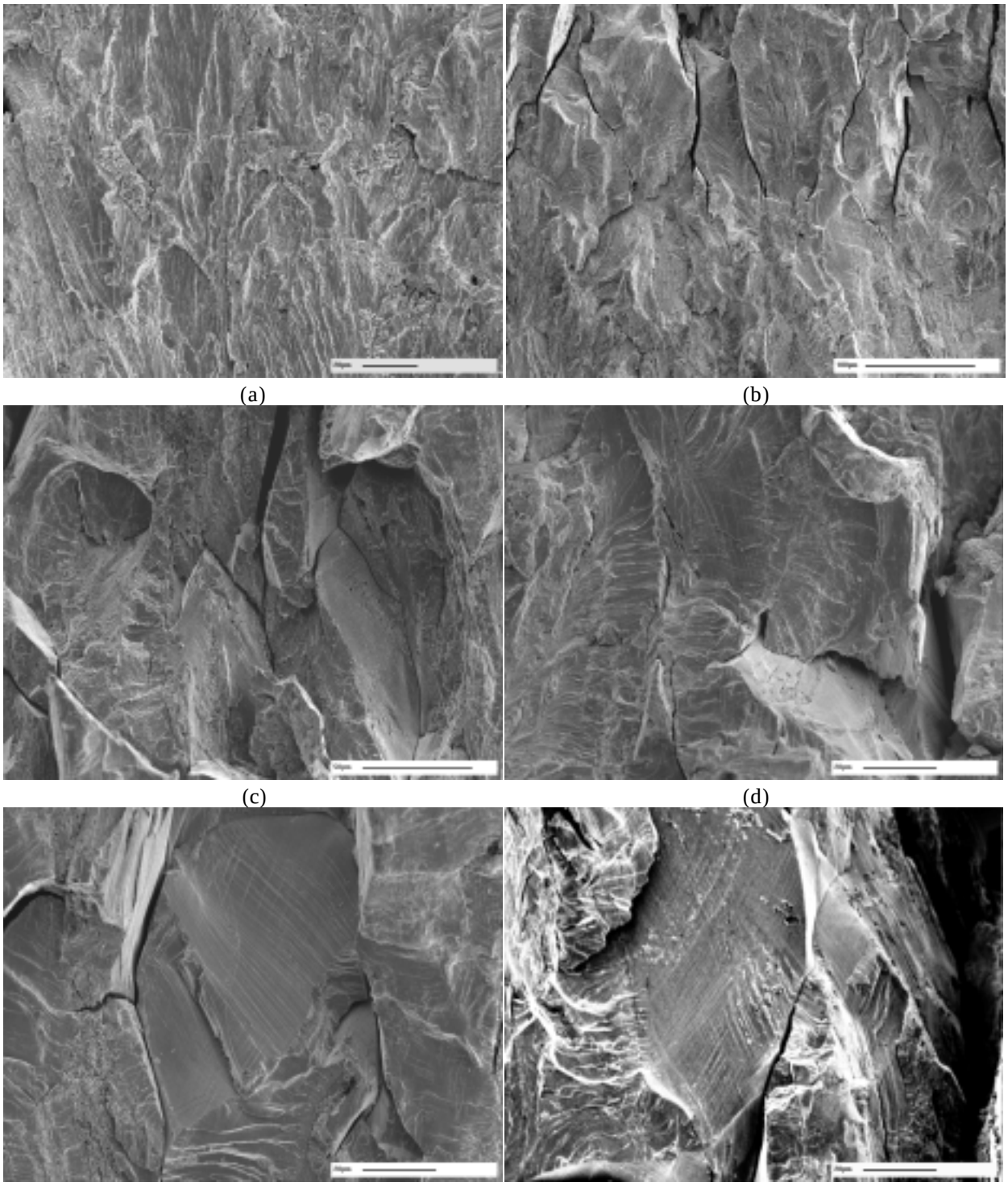

Figure 32. Fractographs of 50% cold–worked Type 316LN SS Heat 18474 tested in high–purity water at 289°C: (a) precracking, 0–20 h; (b) Test Period 1, 10–25 h; (c) Test Periods 6 or 7, 290–480 h; (d) Test Period 7, 430–480 h; (e) and (f) Test Period 5, 150–290 h.

# 4 Evaluation of Causes and Mechanisms of Irradiation-Assisted Cracking of Austenitic Stainless Steel in PWRs

## 4.1 Introduction

Field failures have been reported in various PWR core internal components fabricated from austenitic SSs, e.g., baffle bolt, control rod cladding, pins, keys, and bolts. Many of the failed components were fabricated from cold-worked materials of Types 316, 347, and 304 SS. Typically, failures of PWR core internals are intergranular and are observed at neutron-damage levels approximately a few orders of magnitude higher (i.e., >10 dpa) than the threshold damage level of BWR core internals (i.e., ≈0.7 dpa). At this time, the database on and the mechanistic understanding of PWR core internals are very limited, and it is not clear if the failures should be classified as IASCC or irradiation-assisted cracking (IAC).

The objective of Task 3 of this study is to evaluate the susceptibility of austenitic SS core internals of PWRs to IASCC as a function of fluence, water chemistry, material chemistry, and cold-work. The focus will be on (a) the evaluation of the effects of PWR-like high fluence on susceptibility to IASCC, (b) neutron irradiation embrittlement, e.g., loss of fracture toughness, (c) void swelling behavior in austenitic SSs, (d) effect of cold-work and solution anneal, (e) fracture toughness and SCC behavior of cast duplex SSs at high fluence, and (f) effectiveness of mitigative measures, such as optimization of ferrite content, grain-boundary engineering, and minimization of S concentration. Tests will be conducted on material procured from EBR–II reactor fuel cans and on SS specimens irradiated in the BOR–60 reactor in Russia.

## 4.2 Irradiation of Austenitic Stainless Steels in the BOR-60 Reactor under PWR-Like Conditions (H. M. Chung, W. K. Soppet, and J. M. Hiller)

A major experiment has been initiated during this reporting period to irradiate specimens of various types of materials and geometry under PWR-like conditions. The irradiation experiment is being conducted jointly in cooperation with the Cooperative Irradiation-Assisted Stress Corrosion Cracking Research (CIR) Program. Irradiation of the specimens is performed in the BOR-60 reactor, a sodium-cooled breeder reactor located at the Research Institute of Atomic Reactors (RIAR), Dimitrovgrad, Ulyansk Region, Russian Federation.

Three other parties are participating in the joint irradiation experiment: the CIR-II Program, EdF-Framatome, and the industrial Joint Baffle Bolt (JoBB) Program. Because of this arrangement with the CIR-II Program, a close coordination among the participating parties has been required to optimize available irradiation space, specimen type, specimen size, and target fluence levels. Capsule design, fabrication, specimen loading, and quality control, are being provided by the Research Institute of Atomic Reactors.

### 4.2.1 Specimen Geometry and Material Types

Because of limited irradiation-capsule space in the BOR-60 reactor and in consideration of the effects of very high radioactivity of the specimens on post irradiation testing and post-test analyses, miniaturized SSRT and standard transmission electron microscopy (TEM) disk specimens were selected for the irradiation experiment. After several iterations, test materials

for the irradiation experiment in the BOR-60 reactor were finalized. Table 14 lists the composition of all materials selected for the experiment. The test matrix includes (a) CW and solution-annealed heats of Types 304, 304L, 316, 316 LN, 347 SS, (b) CF-3 and CF-8 cast duplex SSs, (c) grain-boundary-optimized Types 304 and 316 SS and Alloy 690, (d) several model austenitic SSs, and (e) commercial heats of Types 304 and 304L SS that contain low or high concentrations of S or O. The geometry of the SSRT specimens is shown in Fig. 33.

Table 14. Composition (wt.%) of materials selected for irradiation experiment in BOR-60

| | Material Type[a] | Heat ID | Mat. Code[b] | Ni | Si | P | S | Mn | C | N | Cr | Other Elements[c] |
|---|---|---|---|---|---|---|---|---|---|---|---|---|
| 1 | 347 SA | 316642 | D1 | 10.81 | 0.29 | 0.023 | 0.014 | 1.56 | 0.030 | 0.021 | 18.06 | Nb 0.60, Mo 0.29, Cu 0.09 |
| 2 | 347 CW | 316642CW | D2 | 10.81 | 0.29 | 0.023 | 0.014 | 1.56 | 0.030 | 0.021 | 18.06 | Nb 0.60, Mo 0.29, Cu 0.09 |
| 3 | 316 SA | 2333 | B1 | 8.50 | 0.65 | 0.031 | 0.029 | 1.38 | 0.035 | 0.068 | 18.30 | Mo 0.37 |
| 4 | 316 CW | 2333 CW | B2 | 8.50 | 0.65 | 0.031 | 0.029 | 1.38 | 0.035 | 0.068 | 18.30 | Mo 0.37 |
| 5 | 316 LN SA | 623 | B3 | 10.33 | 0.70 | 0.007 | 0.002 | 0.97 | 0.019 | 0.103 | 17.23 | Mo 2.38, Cu 0.21 |
| 6 | 316 LN-Ti SA | 625 | B4 | 10.31 | 0.72 | 0.007 | 0.002 | 0.92 | 0.012 | 0.064 | 17.25 | Mo 2.39, Ti 0.027, Cu 0.21 |
| 7 | 316 SA | C21 | B5 | 10.24 | 0.51 | 0.034 | 0.001 | 1.19 | 0.060 | 0.020 | 16.28 | Mo 2.08, B <0.001, O 0.0112 |
| 8 | 316 CW | C21 CW | B6 | 10.24 | 0.51 | 0.034 | 0.001 | 1.19 | 0.060 | 0.020 | 16.28 | Mo 2.08, B <0.001 |
| 9 | 316 WW | C21 WW | B7 | 10.24 | 0.51 | 0.034 | 0.001 | 1.19 | 0.060 | 0.020 | 16.28 | Mo 2.08, B <0.001 |
| 10 | CF-3 cast SS | 52 | C1 | 9.40 | 0.92 | 0.012 | 0.005 | 0.57 | 0.009 | 0.052 | 19.49 | Mo 0.35, δ 13.5% |
| 11 | CF-8 cast SS | 59 | C2 | 9.34 | 1.08 | 0.008 | 0.007 | 0.60 | 0.062 | 0.045 | 20.33 | Mo 0.32, δ 13.5% |
| 12 | CF-3 cast SS | 69 | C3 | 8.59 | 1.13 | 0.015 | 0.005 | 0.63 | 0.023 | 0.028 | 20.18 | Mo 0.34, δ 23.6% |
| 13 | CF-8 cast SS | 68 | C4 | 8.08 | 1.07 | 0.021 | 0.014 | 0.64 | 0.063 | 0.062 | 20.64 | Mo 0.31, δ 23.4% |
| 14 | 304 SA | C1 | A1 | 8.12 | 0.50 | 0.038 | 0.002 | 1.00 | 0.060 | 0.060 | 18.11 | B 0.001, O 0.0102 |
| 15 | 304 SA | C9 | A2 | 8.75 | 0.39 | 0.013 | 0.013 | 1.72 | 0.062 | 0.065 | 18.48 | B <0.001, O 0.0101 |
| 16 | 304 SA | C12 | A3 | 8.23 | 0.47 | 0.018 | 0.002 | 1.00 | 0.060 | 0.070 | 18.43 | B <0.001 |
| 17 | 304 CW | C1 CW | A4 | 8.12 | 0.50 | 0.038 | 0.002 | 1.00 | 0.060 | 0.060 | 18.11 | B <0.001 |
| 18 | 304 CW | C12 CW | A5 | 8.23 | 0.47 | 0.018 | 0.002 | 1.00 | 0.060 | 0.070 | 18.43 | B <0.001 |
| 19 | 304 GBE | 304 GBE | A6 | 8.43 | 0.46 | 0.014 | 0.003 | 1.54 | 0.065 | 0.088 | 18.38 | Mo 0.51, Co 0.22 |
| 20 | 316 GBE | 316 GBE | B8 | 11.12 | 0.57 | 0.011 | 0.022 | 1.85 | 0.070 | 0.056 | 16.57 | Mo 2.27, Co 0.10 |
| 21 | 690 GBE | 690 GBE | E1 | 59.40 | 0.30 | – | 0.003 | 0.42 | 0.010 | – | 29.10 | Fe 10.26 |
| 22 | 304 BASE | 304 BASE | A7 | 8.46 | 0.41 | 0.013 | 0.014 | 1.56 | 0.065 | 0.086 | 18.32 | Mo 0.36, Co 0.12 |
| 23 | 316 BASE | 316 BASE | B9 | 10.30 | 0.43 | 0.013 | 0.020 | 1.53 | 0.055 | 0.054 | 16.42 | Mo 2.19, Co 0.10 |
| 24 | 690 BASE | 690 BASE | E2 | 61.49 | 0.05 | – | <0.01 | 0.15 | 0.030 | – | 29.24 | Fe 9.02 |
| 25 | HP 304L SA | 945 | A8 | 9.03 | 0.03 | <0.005 | 0.005 | 1.11 | 0.005 | 0.003 | 19.21 | O 0.047, Mo <0.005 |
| 26 | HP 304L SA | 1327 | A9 | 9.54 | 0.01 | 0.001 | 0.002 | 1.12 | 0.006 | <0.001 | 19.71 | O 0.008, Mo 0.02 |
| 27 | 304L SA | C3 | A10 | 8.91 | 0.46 | 0.019 | 0.004 | 1.81 | 0.016 | 0.083 | 18.55 | B <0.001 |
| 28 | 304L CW | C3 CW | A11 | 8.91 | 0.46 | 0.019 | 0.004 | 1.81 | 0.016 | 0.083 | 18.55 | B <0.001 |
| 29 | 304-like | L5 | A12 | 9.66 | 0.90 | 0.113 | 0.028 | 0.47 | 0.006 | 0.033 | 21.00 | B <0.001, δ 3%, O 0.0068 |

[a]SA = solution-annealed; CW = cold-worked at room temperature; WW = warm-worked at 400°C; SS = stainless steel; GBE = grain-boundary-engineered; BASE = base heat for GBE modification; HP = high-purity.
[b]A = Type 304 SS, B = Type 316 SS, C = cast SS, and D = Type 347 SS; E = Alloy 690.
[c]δ = Ferrite content.

### 4.2.2 Test Matrix and Irradiation Plan

A total of 109 SSRT specimens and 222 TEM disks were selected for irradiation in the BOR-60 reactor. The plan calls for irradiation of these specimens to four dose levels, i.e., 5, 10, 20, and 40 dpa. Table 15 summarizes the irradiation plan for the 109 SSRT specimens.

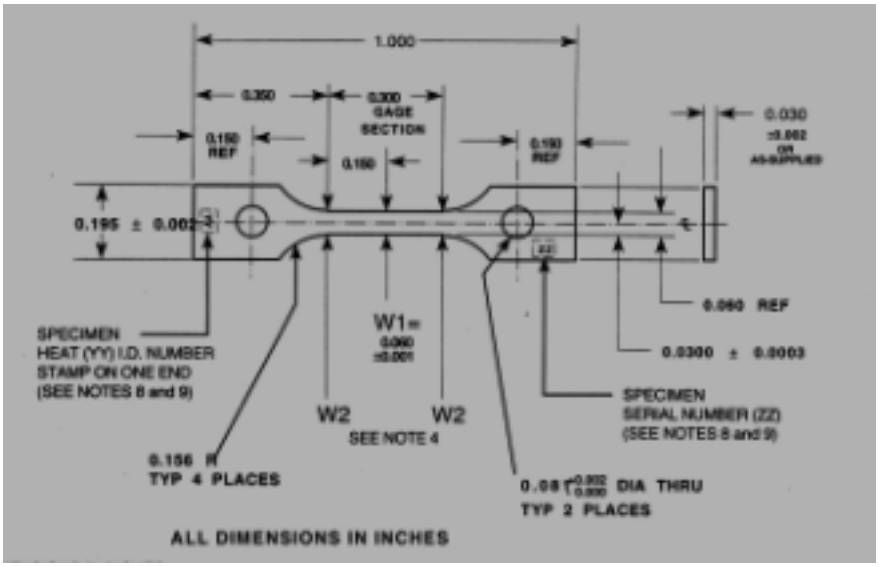


Figure 33. Geometry of SSRT specimen for PWR-like irradiation experiment in the BOR-60 reactor.

Table 15. Summary of material states and target dose of SSRT specimens from BOR-60 experiment

| | Material Type[a] | Descritpion of Material[a] | Heat ID | Mat. Code[b] | SSRT 5 dpa | SSRT 10 dpa | SSRT 20 dpa | SSRT 40 dpa | Mat. Code[b] | SSRT Total |
|---|---|---|---|---|---|---|---|---|---|---|
| 1 | 347 SA | commercial heat 347, SA | 316642 | D1 | 1 | 2 | – | 2 | D1 | 5 |
| 2 | 347 CW | commercial heat 347, CW | 316642CW | D2 | 2 | 2 | – | 2 | D2 | 6 |
| 3 | 316 SA | 316, Heat B, SA | 2333 | B1 | – | 2 | – | | B1 | 2 |
| 4 | 316 CW | 316, Heat B, CW | 2333 CW | B2 | – | 2 | – | 1 | B2 | 3 |
| 5 | 316LN SA | 316LN, SA | 623 | B3 | 1 | 2 | – | | B3 | 3 |
| 6 | 316LN-Ti SA | 316LN, Ti-doped, SA | 625 | B4 | 1 | 2 | 2 | 1 | B4 | 6 |
| 7 | 316 SA | 316, SA | C21 | B5 | 1 | 3 | – | 2 | B5 | 6 |
| 8 | 316 CW | 316, CW | C21 CW | B6 | 2 | 3 | – | 1 | B6 | 6 |
| 9 | 316 WW | 316, warm-worked | C21 WW | B7 | – | 2 | – | 2 | B7 | 4 |
| 10 | CF-3 cast | cast keel block, 13.5% ferrite | 52 | C1 | – | 2 | – | – | C1 | 2 |
| 11 | CF-8 cast | cast keel block, 13.5% ferrite | 59 | C2 | – | 2 | – | – | C2 | 2 |
| 12 | CF-3 cast | cast steel, 23% ferrite | 69 | C3 | – | – | 2 | – | C3 | 2 |
| 13 | CF-8 cast | cast steel, 23% ferrite | 68 | C4 | – | – | 2 | – | C4 | 2 |
| 14 | 304 SA | commercial heat 304, SA, low S | C1 | A1 | 1 | 2 | – | – | A1 | 3 |
| 15 | 304 SA | commercial heat 304, SA, high S | C9 | A2 | 1 | 2 | – | – | A2 | 3 |
| 16 | 304 SA | commercial heat 304, SA, low S | C12 | A3 | 1 | 2 | – | – | A3 | 3 |
| 17 | 304 CW | commercial heat 304, CW | C1 CW | A4 | 1 | 2 | – | – | A4 | 3 |
| 18 | 304 CW | commercial heat 304, CW | C12 CW | A5 | 1 | 2 | 1 | – | A5 | 4 |
| 19 | 304 GBE | grain-boundary-optimized 304 SS | 304 GBE | A6 | 1 | 2 | 1 | – | A6 | 4 |
| 20 | 316 GBE | grain-boundary-optimized 316 SS | 316 GBE | B8 | 1 | 2 | 1 | – | B8 | 4 |
| 21 | 690 GBE | grain-boundary-optimized Alloy 690 | 690 GBE | E1 | 1 | 2 | 1 | – | E1 | 4 |
| 22 | 304 BASE | 304 SS, base heat of 304 GBE | 304 BASE | A7 | 1 | 2 | – | – | A7 | 3 |
| 23 | 316 BASE | 316 SS, base heat of 316 GBE | 316 BASE | B9 | 1 | 2 | – | – | B9 | 3 |
| 24 | 690 BASE | Alloy 690, base heat of 690 GBE | 690 BASE | E2 | 1 | 2 | – | – | E2 | 3 |
| 25 | HP 304L SA | HP 304L, high O, SA | 945 | A8 | 1 | 2 | 1 | – | A8 | 4 |
| 26 | HP 304L SA | HP 304L, low O, SA | 1327 | A9 | 1 | 2 | 2 | 1 | A9 | 6 |
| 27 | 304L SA | commercial heat 304L, SA | C3 | A10 | 1 | 2 | – | – | A10 | 3 |
| 28 | 304L CW | commercial heat 304L, CW | C3 CW | A11 | 1 | 2 | – | 1 | A11 | 4 |
| 29 | 304-like alloy | lab alloy, 21wt.% Cr, ≈2% ferrite, SA | L5 | A12 | 1 | 2 | 3 | – | A12 | 6 |
| | | Total SSRT Specimens 109 | | | 24 | 56 | 16 | 13 | | 109 |

[a]SA = solution-annealed; CW = cold-worked at room temperature; WW = warm-worked at 400°C; GBE = grain-boundary-engineered; BASE = base heat for GBE modification; HP = high-purity.
[b]A = Type 304 SS; B = Type 316 SS; C = cast austenitic SS; D = Type 347 SS; E = Alloy 690.

The material type, target dose, and identification codes for material state and heats are listed in the table. Ninety–six SSRT specimens were arranged in 24 bundles (of four specimens each) for convenience of loading in the irradiation capsules. Table 16 summarizes the target dose and identification codes of the bundles and specimens contained in the bundles. The other 13 SSRT specimens were loosely loaded in the 40-dpa capsule.

Table 16. Summary of bundles of tensile specimens and system used to identify each bundle (SSRT specimens to be irradiated in the BOR-60 experiment; 1 bundle = 4 tensile specimens)

| Target dpa | Bundle Code | Engraved Mark on Front Tensile Specimen to Identify Bundle | Engraved Mark on Back Tensile Specimen to Identify Bundle |
|---|---|---|---|
| 5 | 5-1 | D1-1 | B3-1 |
| 5 | 5-2 | A5-1 | E1-1 |
| 5 | 5-3 | B4-1 | B6-2 |
| 5 | 5-4 | A7-1 | A8-1 |
| 5 | 5-5 | A1-1 | A4-1 |
| 5 | 5-6 | A9-1 | A12-1 |
| 10 | 10-1 | D1-2 | D2-4 |
| 10 | 10-2 | B1-1 | B2-2 |
| 10 | 10-3 | B3-2 | B4-3 |
| 10 | 10-4 | B5-2 | B6-3 |
| 10 | 10-5 | B6-4 | B7-2 |
| 10 | 10-6 | C1-1 | C2-2 |
| 10 | 10-7 | A1-2 | A2-3 |
| 10 | 10-8 | A3-2 | A4-3 |
| 10 | 10-9 | A5-2 | A6-3 |
| 10 | 10-10 | B8-2 | E1-3 |
| 10 | 10-11 | A7-2 | B9-3 |
| 10 | 10-12 | E2-2 | A8-3 |
| 10 | 10-13 | A9-2 | A10-3 |
| 10 | 10-14 | A11-2 | A12-3 |
| 20 | 20-1 | B4-4 | C4-2 |
| 20 | 20-2 | A5-4 | A12-4 |
| 20 | 20-3 | C3-1 | B8-4 |
| 20 | 20-4 | A8-4 | A12-5 |
| 40 | 13 loose tensiles | D1-4, D1-5, D2-5, D2-6, B2-3, B4-6, B5-5, B5-6, B6-6, B7-3, B7-4, A9-6, A11-4 | |

The 3-mm-diameter disk specimens were encapsulated in one He-filled and sealed capsule and four "weeper" capsules that are open to flowing sodium through machined holes. All capsules were fabricated from Type 316 SS. Table 17 describes the five capsules that contain the disk specimens. Table 18 describes the disk specimens, i.e., material type, material state, source heat number, target dose, and identification codes.

### 4.2.3 Status of BOR-60 Irradiation Experiment

Fabrication of the tensile and disk specimens was completed. The specimens were cleaned, packaged, transported, and encapsulated at the BOR-60 reactor site. Irradiation started May 2001. Irradiation to 5.7 dpa was completed in October 2001 in two cycles (1st cycle 2.8 dpa, 2nd cycle 2.9 dpa). Sodium inlet and outlet temperatures were, respectively, 312.7°C and 322.1–322.6°C during the irradiation of 24 tensile and 56 disk specimens.

Table 17. Description of five capsules that contain disk specimens (all capsules fabricated from Type 316 stainless steel)

| | Capsule Identification Number | Target Irradiation (dpa) | Description of Capsule | TEM Disks in Contact with |
|---|---|---|---|---|
| 1 | AN05 | 5 | Perforated to allow sodium flow, weeper | Liquid sodium |
| 2 | AN10 | 10 | Perforated to allow sodium flow, weeper | Liquid sodium |
| 3 | AN20 | 20 | Perforated to allow sodium flow, weeper | Liquid sodium |
| 4 | AN40 | 40 | Perforated to allow sodium flow, weeper | Liquid sodium |
| 5 | HE10 | 10 | Solid tube filled with helium and weld-sealed | Gaseous helium |

Table 18. Disk specimens sealed in four perforated sodium capsules and one helium-filled capsule (see Table 17 for capsule identification numbers AN05, AN10, HE10, AN20, and AN40)

| | Material Type[a] | Descritpion of Material[a] | Heat ID | Mat. Code[b] | AN05 5 dpa | AN10 10 dpa | HE10 10 dpa | AN20 20 dpa | AN40 40 dpa | Disk Total |
|---|---|---|---|---|---|---|---|---|---|---|
| 1 | 347 SA | commercial heat 347, SA | 316642 | D1 | 2 | 1 | 1 | 1 | 2 | 7 |
| 2 | 347 CW | commercial heat 347, CW | 316642CW | D2 | 2 | 1 | 1 | 2 | 2 | 8 |
| 3 | 316 SA | 316, Heat B, SA | 2333 | B1 | 2 | 1 | 1 | 2 | 2 | 8 |
| 4 | 316 CW | 316, Heat B, CW | 2333 CW | B2 | 2 | 1 | 1 | 2 | 2 | 8 |
| 5 | 316LN SA | 316LN, SA | 623 | B3 | 2 | 1 | 1 | 2 | 2 | 8 |
| 6 | 316LN-Ti SA | 316LN, Ti-doped, SA | 625 | B4 | 2 | 1 | 1 | 2 | 2 | 8 |
| 7 | 316 SA | 316, SA | C21 | B5 | 2 | 1 | 1 | 2 | 2 | 8 |
| 8 | 316 CW | 316, CW | C21 CW | B6 | 2 | 1 | 1 | 1 | 2 | 8 |
| 9 | 316 WW | 316, WW | C21 WW | B7 | 2 | 2 | - | 2 | 2 | 8 |
| 10 | CF-3 cast | cast keel block, 13.5% ferrite | 52 | C1 | 2 | 1 | 1 | 2 | 2 | 8 |
| 11 | CF-8 cast | cast keel block, f13.5% ferrite | 59 | C2 | 2 | 2 | - | 2 | 2 | 8 |
| 12 | CF-3 cast | cast steel, 23% ferrite | 69 | C3 | 2 | 1 | - | 1 | 2 | 6 |
| 13 | CF-8 cast | cast steel, f23% ferrite | 68 | C4 | 2 | 2 | - | 2 | 2 | 8 |
| 14 | 304 SA | commercial 304, SA, low S | C1 | A1 | 2 | 1 | 1 | 2 | 2 | 8 |
| 15 | 304 SA | commercial 304, SA, high S | C9 | A2 | 2 | 1 | 1 | 2 | 2 | 8 |
| 16 | 304 SA | commercial 304, SA, low S | C12 | A3 | 2 | 1 | 1 | 2 | 2 | 8 |
| 17 | 304 CW | commercial 304, CW | C1 CW | A4 | 2 | 1 | 1 | 2 | 2 | 8 |
| 18 | 304 CW | commercial 304, CW | C12 CW | A5 | 2 | 1 | 1 | 2 | 2 | 8 |
| 19 | 304 GBE | grain-boundary-optimized 304 SS | 304 GBE | A6 | 2 | 1 | 1 | 2 | 2 | 8 |
| 20 | 316 GBE | grain-boundary-optimized 316 SS | 316 GBE | B8 | 2 | 1 | 1 | 2 | 2 | 8 |
| 21 | 690 GBE | grain-boundary-optimized Alloy 690 | 690 GBE | E1 | 2 | 1 | 1 | 2 | 2 | 8 |
| 22 | 304 BASE | 304 SS, GBE 304 base heat | 304 BASE | A7 | 2 | 1 | 1 | 2 | 2 | 8 |
| 23 | 316 BASE | 316 SS, GBE 316 base heat | 316 BASE | B9 | 2 | 2 | - | 2 | 2 | 8 |
| 24 | 690 BASE | A 690, GBE 690 base heat | 690 BASE | E2 | 2 | 2 | - | 2 | 2 | 8 |
| 25 | HP 304L SA | HP 304L, high O, SA | 945 | A8 | 2 | 1 | 1 | 2 | 2 | 8 |
| 26 | HP 304L SA | HP 304L, low O, SA | 1327 | A9 | 2 | 2 | 2 | 2 | 2 | 10 |
| 27 | 304L SA | commercial heat 304L, SA | C3 | 10 | - | - | - | - | - | 0 |
| 28 | 304L CW | commercial heat 304L, CW | C3 CW | 11 | 2 | 1 | 1 | 2 | 2 | 8 |
| 29 | 304-like alloy | lab alloy, 21wt.% Cr, ≈2% ferrite, SA | L5 | 12 | 2 | 1 | 1 | 2 | 2 | 8 |
| | | Total TEM Disk Specimens: 222 | | | 56 | 34 | 23 | | | 222 |

[a]SA = solution-annealed; CW = cold-worked at room temperature; WW = warm-worked at 400°C; GBE = grain-boundary-engineered; BASE = base heat for GBE modification; HP = high-purity.
[b]A = Type 304, B = Type 316, C = cast, and D = Type 347 stainless steels; E = Alloy 690.

# 5 Cracking of Nickel Alloys and Weldments (W. K. Soppet, O. K. Chopra, and W. J. Shack)

## 5.1 Introduction

This part of the study consists primarily of establishing CGRs under constant and cyclic loading and evaluating Ni alloys and weld metals metallographically to develop comprehensive and statistically significant analyses that could be used to determine the dependence of the SCC of these materials on alloy composition, microstructure, water chemistry, temperature, and other factors. High–Ni alloys have experienced general corrosion (tube wall thinning), localized intergranular attack (IGA), and SCC in LWRs. Secondary–side IGA* and axial and circumferential SCC** have occurred in Alloy 600 tubes at tube support plates in many steam generators. Primary–water SCC of Alloy 600 steam generator tubes in PWRs at roll transitions and U–bends and in tube plugs*** is a widespread problem that has been studied intensively. In the primary system of PWRs, cracking has occurred in Alloy 600 and other high–Ni alloys that are used in applications such as instrument nozzles and heater thermal sleeves in the pressurizer,† and penetrations for the control–rod drive mechanism in the closure heads of reactor vessels.†† In BWRs, cracking has occurred in dissimilar–metal welds between SS piping and low–alloy steel nozzles,††† in jet pump hold–down beams,§ and in shroud–support–access–hole covers.§§ Alloy 690, with a higher Cr content and greater resistance to SCC, has been proposed as an alternate to Alloy 600.

A program is being conducted at ANL to evaluate the resistance of Alloys 600 and 690 and their welds to EAC in simulated LWR coolant environments. Fracture mechanics CGR tests are being conducted on CT specimens of Alloys 600 and 690 in either oxygenated high–purity water or deaerated water that contained B, Li, and low concentrations of dissolved H at 289–320°C; the results have been presented elsewhere.[80–86] Because environmental degradation of the alloys in many cases is very sensitive to processing, the effects of various thermomechanical treatments are also being evaluated.

---

*NRC Information Notice No. 91–67, "Problems with the Reliable Detection of Intergranular Attack (IGA) of Steam Generator Tubing," Oct. 1991.

**NRC Information Notice No. 90–49, "Stress Corrosion Cracking in PWR Steam Generator Tubes," Aug. 1990; Notice No. 96–38, "Results of Steam Generator Tube Examinations," June 1996; Notice No. 2001–16, "Recent Foreign and Domestic Experience with Degradation of Steam Generator Tubes and Internals," Oct. 2001.

***NRC Regulatory Issue Summary 00–022, "Issues Stemming from NRC Staff Review of Recent Difficulties Experienced in Maintaining Steam Generator Tube Integrity," Nov. 2000; Information Notice No. 97–26, "Degradation in Small-Radius U-bend Regions of Steam Generator Tubes," May 1997; Notice No. 94–87, "Unanticipated Crack in a Particular Heat of Alloy 600 Used for Westinghouse Mechanical Plugs for Steam Generator Tubes," Dec. 1994.

†NRC Information Notice No. 90–10, "Primary Water Stress Corrosion Cracking (PWSCC) of Inconel 600," Feb. 1990.

††NRC Generic Letter 97-01: "Degradation of Control Rod Drive Mechanism and Other Vessel Closure Head Penetrations," Apr. 1, 1997; USNRC Bulletin 01–01, "Circumferential Cracking of Reactor Pressure Vessel Head Penetration Nozzles," Aug. 2001; Bulletin 02–01, "Reactor Pressure Vessel Head Degradation and Reactor Coolant Pressure Boundary Integrity," March 2002.

†††NRC Information Notice 2000–17, "Crack in Weld Area of Reactor Coolant System Hot Leg Piping at V. C. Summer," Oct. 2000; Supp. 1, Nov. 2000; Supp. 2, Feb. 2001.

§NRC Information Notice 93–101, "Jet Pump Hold–Down Beam Failure," Dec. 1993.

§§NRC Information Notice 92–57, "Radial Cracking of Shroud Support Access Hole Cover Welds," Aug. 1992.

The existing CGR data obtained at ANL and elsewhere for Alloys 600 and 690 under cyclic loading conditions have been compiled and evaluated to establish the effects of alloy type, temperature, load ratio R, stress intensity K, and DO level. To obtain a qualitative understanding of the degree and range of conditions that are necessary for significant environmental enhancement of growth rates in LWR environments, the experimental CGRs have been compared with CGRs that would be expected in air under the same mechanical loading conditions. In air, fatigue CGRs are generally represented by the equation

$$da/dN = C(T)\, F(f)\, S(R)\, (\Delta K)^n, \tag{17}$$

where the functions C, F, and S express the dependence of temperature, frequency, and stress ratio, and n is the exponent for the power–law dependence of growth rates on the stress intensity factor range ΔK. The effect of temperature, stress ratio R, cyclic frequency, and stress intensity factor range ΔK on the CGRs was established from an analysis of the existing fatigue CGR data.[84] The CGR (m/cycle) of Alloy 600 in air is expressed as

$$da/dN = C_{A600}\, (1 - 0.82\, R)^{-2.2}\, (\Delta K)^{4.1}, \tag{18}$$

where ΔK is in $MPa \cdot m^{1/2}$, and the constant $C_{A600}$ is given by a third-order polynomial of temperature T (°C) expressed as

$$C_{A600} = 4.835 \times 10^{-14} + (1.622 \times 10^{-16})T - (1.490 \times 10^{-18})T^2 + (4.355 \times 10^{-21})T^3. \tag{19}$$

The CGR (m/cycle) of Alloy 690 in air is expressed as

$$da/dN = C_{A690}\, (1 - 0.82\, R)^{-2.2}\, (\Delta K)^{4.1}, \tag{20}$$

where ΔK is in $MPa \cdot m^{1/2}$ and the constant $C_{A690}$ is given by a third-order polynomial of temperature T (°C) expressed as

$$C_{A690} = 5.423 \times 10^{-14} + (1.83 \times 10^{-16})T - (1.725 \times 10^{-18})T^2 + (5.490 \times 10^{-21})T^3. \tag{21}$$

For both alloys, the estimated values show good agreement with the experimental results. Under similar loading conditions, the CGRs of Alloy 690 appear to be slightly higher than the CGR of Alloy 600. This difference most likely is an artifact of a smaller database for Alloy 690.

The fatigue CGRs of Alloy 600 are enhanced in high–DO water; the environmental enhancement of growth rates does not appear to depend on either the C content or heat treatment of the material. Also, in high–DO water, the CGRs at 320°C are comparable to those at 289°C. In contrast to the behavior in high–DO water, environmental enhancement of CGRs of Alloy 600 in low–DO water seems to depend on material conditions such as yield strength and grain boundary coverage of carbides. Materials with high yield strength and/or low grain boundary coverage of carbides exhibit enhanced CGRs. Correlations have been developed for estimating the enhancement of CGRs of Alloy 600 in LWR environments relative to the CGRs in air under the same loading conditions.

During the current reporting period, CGR tests have been completed on 30% CW Alloy 600 (Heat NX131031) specimen in high–purity water under various environmental and loading

conditions. The results from these tests are compared with data obtained earlier on several heats of Alloy 600 tested in high–DO water.

## 5.2 Experimental

The facility for conducting corrosion-fatigue tests in water at elevated temperature and pressure consists of a closed-loop electro hydraulic material test system equipped with an extra high load frame rated at 89 kN (20,000 lbs) maximum, and a commercial autoclave with a recirculating or once–through water system. The autoclave, mounted within the load frame, has been modified to permit an ≈19–mm (0.75–in.) shaft to load the test specimen through a "Bal-Seal" gland in the top of the autoclave cover.

1. COVER GAS SUPPLY CYLINDER
2. TWO-STAGE HIGH-PRESSURE REGULATOR
3. FLASH ARRESTOR (WITH HYDROGEN CYLINDERS ONLY)
4. LOW-PRESSURE REGULATOR
5. FLOW METER
6. GAS PURIFIER
7. COMPOUND VACUUM & PRESSURE GAUGE
8. PRESSURE RELIEF VALVE
9. VENT TO AIR WITH FLASH ARRESTOR
10. FEEDWATER STORAGE TANK
11. SPARGE TUBE
12. FEEDWATER FILL PORT
13. WATER SAMPLE PORT
14. SOLENOID VALVE
15. 0.2–MICRON FILTER
16. HIGH-PRESSURE PUMP
17. CHECK VALVE
18. AIR INJECTION PORT
19. SYSTEM BLEED PORT
20. RUPTURE DISK
21. PRESSURE TRANSDUCER
22. HIGH-PRESSURE GAUGE
23. HEAT EXCHANGER
24. AUTOCLAVE PREHEATER
25. COMMERCIAL AUTOCLAVE
26. THERMOWELL
27. "BAL SEAL" RETAINER
28. ECP CELL
29. ECP CELL BYPASS LINE
30. BACK-PRESSURE REGULATOR
31. PRESSURE RELIEF VALVE
32. CONDUCTIVITY METER
33. DISSOLVED-OXYGEN METER
34. RECIRCULATING PUMP
35. ION EXCHANGE BED
36. ION EXCHANGE BED BYPASS LINE

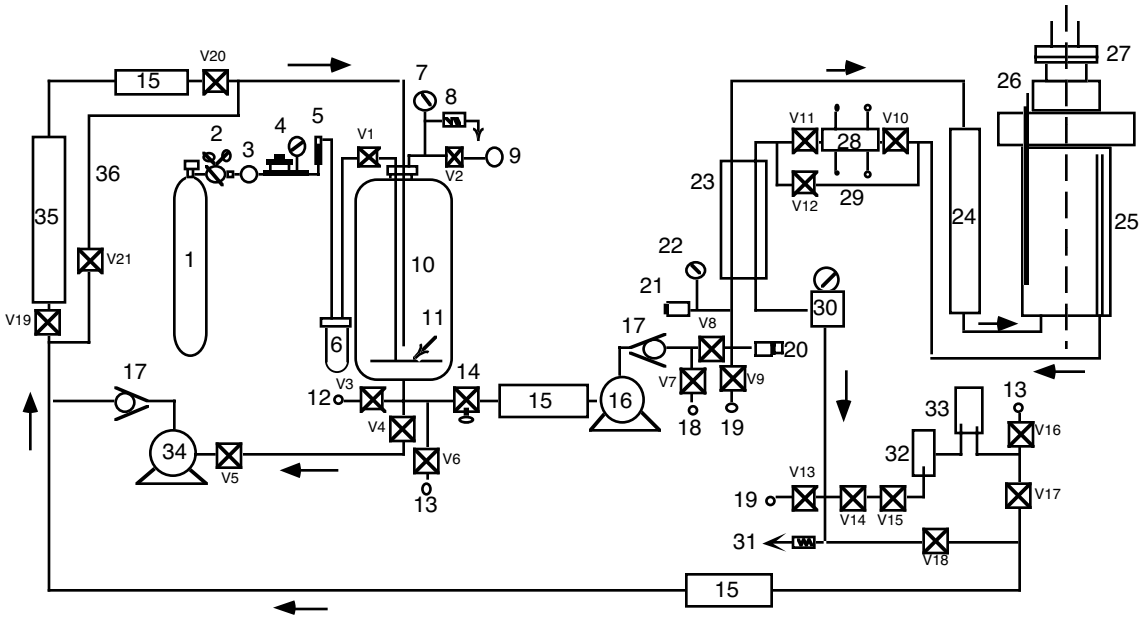


Figure 34. Schematic diagram of recirculating autoclave system used for crack growth rate tests on 1–T compact tension specimens.

Figure 34 is a schematic diagram of the recirculating water system. The water system consists of a closed feedwater storage tank, 0.2 micron filter, high–pressure pump, regenerative heat exchanger, autoclave preheater, test autoclave, ECP cell, regenerative heat exchanger, back-pressure regulator, a 0.2–micron filter, an ion exchange bed, another 0.2–micron filter,

and a return line to the tank. The system uses Types 316 and 304 stainless steel tubing. For tests in simulated BWR environments, water quality is maintained by recirculating the supply tank feedwater through a cleanup system that consists of a recirculating pump (Item 33), ion exchange bed (Item 34), and 0.2-micron filter (Item 15). For tests in simulated PWR environments, the feedwater cleanup system is omitted; also, to avoid contamination, the ECP cell in the return line from the autoclave to the water supply tank is bypassed during recirculation. Water from the back–pressure regulator is released in the once–through water system to the drain, and, in the recirculating system, to the ion–exchange cleanup system. In some systems, a conductivity meter and a DO meter (Items 31 and 32) are included downstream from the back–pressure regulator to monitor the effluent water chemistry. Water is recirculated at relatively low flow rates of ≈10 mL/min.

The 130–L feedwater storage tank, manufactured by Filpaco Industries, is constructed of Types 304 and 316 SS. The tank is designed for vacuum, or positive pressure to 60 psig. The storage tank contains either a mixture of $N_2/O_2$ or pure $H_2$ cover gas to maintain a desired DO or dissolved H concentration in the water.

The BWR environment consists of high–purity deionized water that typically contains ≈300 ppb DO. The simulated PWR feedwater contains <0.01 ppm DO but contains small additions of Li and B. The deionized water is prepared by passing building deionized water through a local set of filters that comprise a C filter, an Organex–Q filter, two ion exchangers, and a 0.2–mm capsule filter. The DO level in water is established by bubbling $N_2$ that contains 1–2% $O_2$ through deionized water in the supply tank. Water samples are taken periodically to measure pH, resistivity, and DO concentration.

The corrosion fatigue tests were conducted according to ASTM Designation E 647 "Standard Test Method for Measurement of Fatigue Crack Growth Rates." The crack length of each specimen is monitored by DC potential measurements. The composition of Alloy 600 (Heat NX131031) used for the present CGR tests is given in Table 19.

Table 19. Composition (wt.%) of Alloy 600 Heat NX131031 base metal as determined by the vendor and by ANL

| Analyst | C | Mn | Fe | S | P | Si | Cu | Ni | Cr | Ti | Nb | Co |
|---|---|---|---|---|---|---|---|---|---|---|---|---|
| Vendor | 0.07 | 0.22 | 7.39 | 0.002 | 0.006 | 0.12 | 0.05 | 76.00 | 15.55 | 0.24 | 0.07 | 0.058 |
| ANL | 0.07 | 0.22 | 7.73 | 0.001 | – | 0.18 | 0.06 | 75.34 | – | – | – | – |

## 5.3 Results

The environmental and loading conditions, and the CGRs measured by the DC potential method are given in Table 20. The water DO level and conductivity were monitored continuously during the test, whereas the ECPs of a Pt and SS electrode were determined periodically; the values are listed in the table. The change in crack length and $K_{max}$ during the various test periods is shown in Fig. 35. The specimen was precracked at R = 0.2 or 0.4 to allow a crack advance of at least 2 mm. The corrosion fatigue tests were conducted at R = 0.7 and a sawtooth waveform with a 300– or 1000–s rise time and 2–s return time. The maximum stress intensity factor was increased from 28 to 32 MPa $m^{1/2}$ and then to 37 MPa $m^{1/2}$ (Test Periods 10 and 12, respectively) by cycling at R = 0.2– and 10–s rise time.

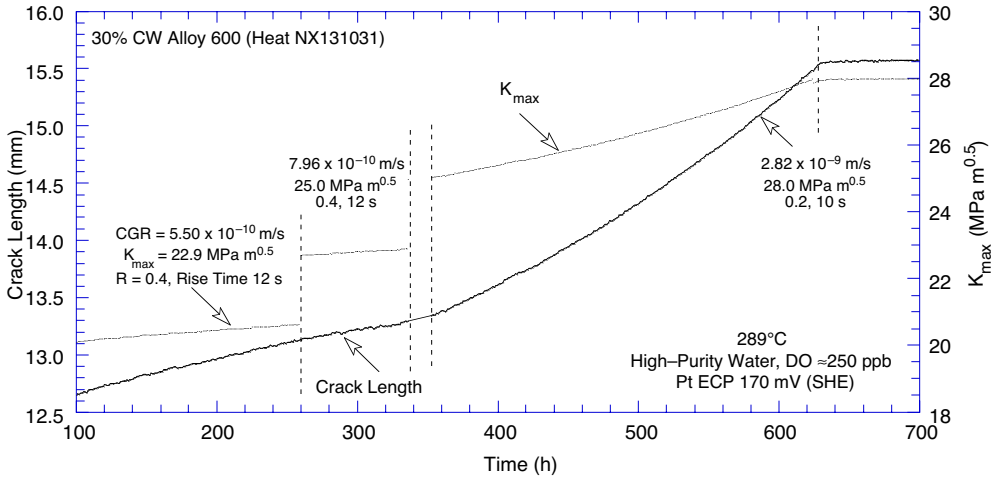


(a)

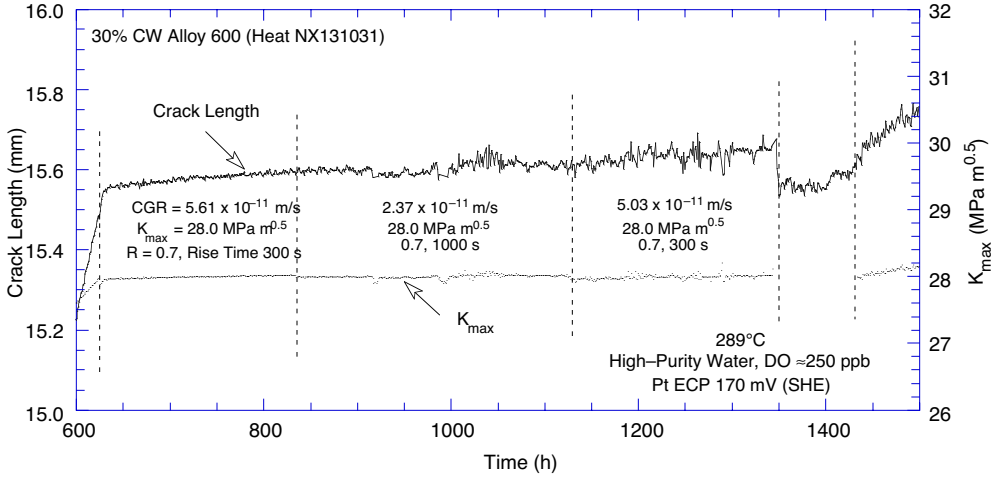


(b)

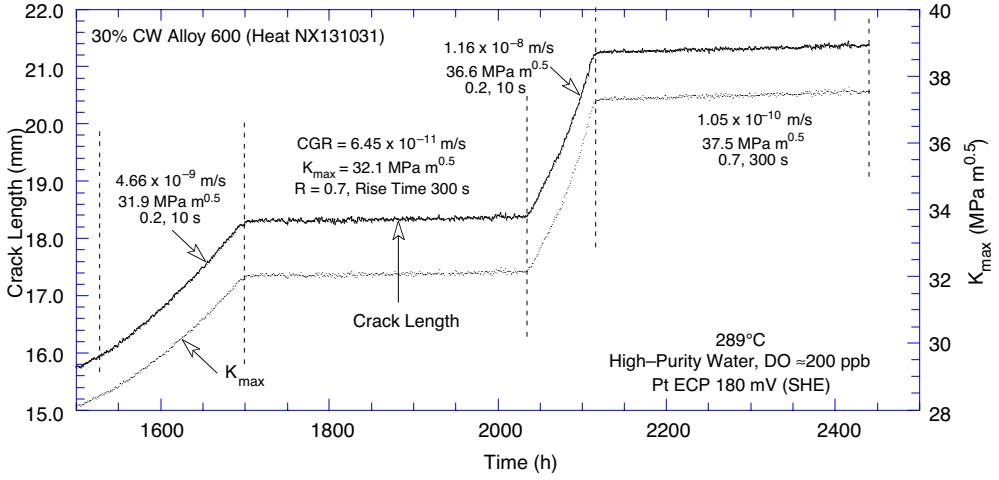


(c)

Figure. 35. Crack–length–vs.–time plot for 30% cold–worked Alloy 600 specimen in high–purity water at 289°C: (a) 100–700 h, (b) 600–1500 h, (c) 1500–2500 h.

Table 20. Crack growth results for 30% cold–worked Alloy 600[a] in high–purity water at 290°C

| Test Period | Test Time, h | $O_2$[b] Conc. ppb | Electrode Potential[b] mV(SHE) at 289°C SS | Pt | Load Ratio | Rise Time s | $K_{max}$[c], MPa·m$^{1/2}$ | ΔK, MPa·m$^{1/2}$ | Growth Rate, m/s | Crack Length, mm |
|---|---|---|---|---|---|---|---|---|---|---|
| Precrack | 283 | 266 | 47 | 200 | 0.2 | 12 | 20.63 | 16.50 | 8.33E-10 | 13.15 |
| 1 | 336 | 253 | – | – | 0.4 | 12 | 22.89 | 13.73 | 5.50E-10 | 13.29 |
| 2 | 355 | 266 | – | 168 | 0.4 | 12 | 25.03 | 15.02 | 7.96E-10 | 13.34 |
| 3 | 430 | 200 | 48 | 176 | 0.2 | 12 | 25.63 | 20.50 | 1.70E-09 | 13.79 |
| 4a | 495 | 250 | 53 | 172 | 0.2 | 10 | 26.28 | 21.02 | 2.03E-09 | 14.27 |
| 4b | 560 | 245 | – | – | 0.2 | 10 | 27.05 | 21.64 | 2.40E-09 | 14.83 |
| 4c | 624 | 245 | – | – | 0.2 | 10 | 27.96 | 22.36 | 2.82E-09 | 15.48 |
| 5 | 834 | 239 | – | – | 0.7 | 300 | 28.02 | 8.41 | 5.61E-11 | 15.60 |
| 6 | 1127 | 231 | – | – | 0.7 | 1000 | 28.02 | 8.41 | 2.37E-11 | 15.62 |
| 7 | 1344 | 241 | – | – | 0.7 | 300 | 28.02 | 8.41 | 5.03E-11 | 15.65 |
| 8 | 1433 | 243 | – | – | 1.0 | - | 11.79 | - | - | |
| 9 | 1506 | 242 | – | – | 0.4 | 60 | 28.17 | 16.90 | 4.57E-10 | 15.76 |
| 10a | 1570 | 233 | – | – | 0.2 | 10 | 29.00 | 23.20 | 2.60E-09 | 16.34 |
| 10b | 1645 | 224 | – | – | 0.2 | 10 | 30.57 | 24.46 | 3.82E-09 | 17.38 |
| 10c | 1695 | 221 | – | – | 0.2 | 10 | 31.91 | 25.53 | 4.66E-09 | 18.22 |
| 11 | 2032 | 203 | 43 | 187 | 0.7 | 300 | 32.14 | 9.64 | 6.45E-11 | 18.37 |
| 12a | 2076 | 177 | – | – | 0.2 | 10 | 34.13 | 27.30 | 8.01E-09 | 19.54 |
| 12b | 2107 | 184 | – | – | 0.2 | 10 | 36.55 | 29.24 | 1.16E-08 | 20.86 |
| 13 | 2441 | 185 | – | – | 0.7 | 300 | 37.54 | 11.26 | 1.05E-10 | 21.37 |

[a]Compact tension specimen (1T CT) of Alloy 600 (Heat NX131031), mill annealed + 30% cold worked.
[b]Effluent dissolved oxygen concentration and ECP. Effluent conductivity was 0.2–0.3 μS/cm. Feedwater conductivity at 25°C 0.06 μS/cm and pH at 25°C 6.0.
[c]Stress intensity, $K_{max}$, values at the end of the time period.

After the test, the specimen was fractured, and a detailed metallographic examination of the specimen was performed to validate the measurements of crack length by the DC potential method. A photograph of the broken top half of the 1T–CT specimen is shown in Fig. 36. Three distinct elliptical crack fronts can be seen on the fracture surface; these correspond to the final crack and start of Test Periods 10 and 12, in which a load ratio of 0.2 was used. The average crack lengths were determined by (a) measuring the area under each of the crack fronts, and (b) the 9/8 averaging technique, i.e., the two–near–surface measurements were

Figure 36.
Fracture surface of 30% cold worked Alloy 600 specimen tested at 289°C in high–purity water with ≈250 ppb dissolved oxygen.

averaged and the resultant value was averaged with the remaining seven measurements. The average crack lengths from area measurements and 9/8 averaging were 16.46, 19.02, and 21.45 mm, and 16.71, 19.12, and 21.55 mm, respectively. The measured value of the final crack length is in good agreement with the value of 21.37 mm estimated from the DC potential method; the difference between the measured and estimated values is <1%. For the other two crack fronts, measured values are somewhat greater than the values of 15.76 and 18.37 mm estimated from the DC potential method. These differences most likely are due to poor definition of the two intermediate crack fronts near the edge of the specimen; the crack front cannot be clearly defined near the specimen edge. Based on these results, a correction was considered unnecessary for the crack lengths estimated from the DC potential method.

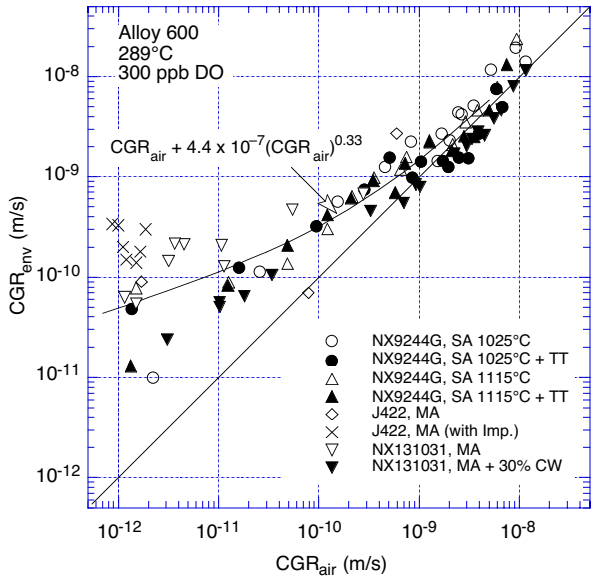


Figure 37.
Corrosion fatigue data for mill–annealed and 30% cold worked Alloy 600 at 289°C in high–purity water with ≈250 ppb DO.

The measured CGRs in water and those predicted in air for 30% CW Alloy 600 for the same loading conditions are plotted in Fig. 37. The results obtained earlier on the same heat of Alloy 600 in the mill annealed (MA) condition and several other heats of Alloy 600 in ≈ 0.3 or 6 ppm DO are also included in the figure. The CGRs (da/dN in m/cycle) in air were determined from Eqs. 18 and 19. In high–DO water, nearly all of the heats and heat treatment conditions that have been investigated show enhanced growth rates. The growth rates for MA Heat NX131031 are slightly higher than those for several other heats of Alloy 600 either in the solution annealed (SA) condition or SA plus thermally treated condition.

The environmental enhancement of CGRs of 30% CW Heat NX131031 in high–DO water appears to be a factor of 2–5 lower than that observed earlier for MA material. This difference may be partially due to a change in the CGRs in air for the CW material, e.g., the CGRs of 30% CW Alloy 600 in air may be somewhat lower that those for the MA material. For example, under loading conditions that correspond to >1 x $10^{-9}$ m/s CGRs in air, the rates for the 30% CW material are a factor of ≈2 lower than those predicted for SA or MA Alloy 600 in air. Under these loading conditions mechanical fatigue dominates crack propagation and environmental effects on growth rates are insignificant; the CGRs in water should be comparable to those in air. After accounting for the lower CGRs of the CW alloy in air (i.e., shifting the solid inverted triangles in Fig. 37 to the left by a factor of 2), the growth rates of the 30% CW Alloy 600 are comparable to those for the MA material.

These results appear to be consistent with the very limited data available for the effect of cold work on the CGRs of Alloy 600 in high–DO environments.[87] Although several studies have established the effect of cold–work on the susceptibility of Alloy 600 to IGSCC in low–DO PWR environments,[88–90] limited data in high–DO water show comparable growth rates for annealed and CW Alloy 600.[87] In low–DO water, the CGRs for the same two materials, i.e., annealed and CW Alloy 600, differed by nearly one order of magnitude. Additional tests will be conducted on CW Alloy 600 to investigate the effects of cold–work on CGRs in low– and high–DO environments.

Figure 37 shows that the CGRs of 30% CW Heat NX131031 are slightly lower and those of MA Heat NX131031 are slightly higher than the rates predicted by the best–fit curve for Alloy 600 in high–DO water, given by the expression

$$CGR_{env} = CGR_{air} + 4.4x10^{-7}\left(CGR_{air}\right)^{0.33}. \quad (22)$$

The elliptical shape of the crack front seems to be consistent with these results, i.e., in high–DO water, CGRs of CW material are lower than those of MA material. The amount of cold–work is not uniform across the thickness of the specimen; it is greater near the surface. Consequently, CGR is likely to be lower near the edge of the CT specimen. Fractographic examination of the specimen indicates a mixed–fracture mode, i.e., predominantly intergranular fracture, with isolated regions of transgranular fracture, Fig. 38.

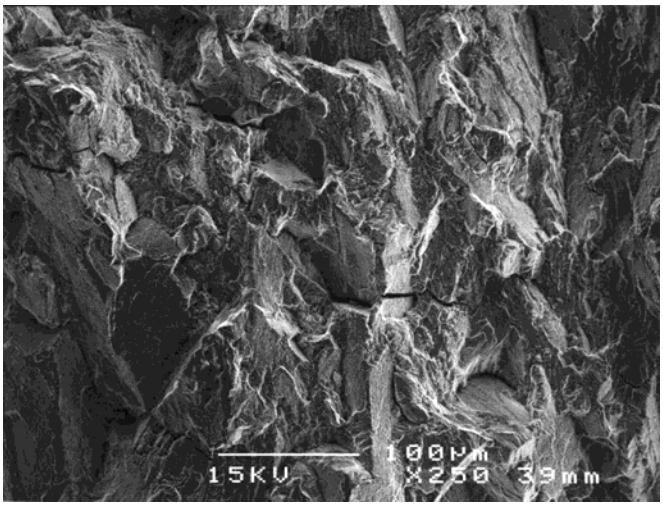


Figure 38.
Fracture morphology of 30% cold–worked Alloy 600 specimen tested at 289°C in high–purity water with ≈250 ppb dissolved oxygen.

# 6 Summary

## 6.1 Environmental Effects on Fatigue ε–N Behavior

This study has evaluated the effects of key material and loading variables, such as strain amplitude, strain rate, temperature, DO level in water, and material heat treatment, on the fatigue lives of wrought and cast austenitic SSs in air and LWR environments. Unlike carbon and low–alloy steels, environmental effects on the fatigue life of austenitic SSs are significant in low–DO water; effects on life in high–DO water are either comparable or, for some steels, less pronounced than those in low–DO water.

The mechanism of fatigue crack initiation in austenitic SSs in LWR environments has been examined. Fatigue crack initiation has been divided into two stages: an initiation stage that involves the growth of MSCs (i.e., cracks smaller than ≈200 μm), and a propagation stage that involves the growth of mechanically small cracks. Crack lengths as a function of fatigue cycles have been determined in air and LWR environments. The results indicate that decreases in the fatigue lives of these steels are caused primarily by the effects of environment on the growth of MSCs and, to a lesser extent, on enhanced growth rates of mechanically small cracks.

To characterize fracture morphology, fatigue test specimens were examined in detail by metallography. The crack morphology of the specimen surface is different in low–DO water than in air or high–DO water; cracks are always straight and normal to the stress axis in low–DO water, whereas, in air or high–DO water, they follow certain crystallographic features. However, the morphology of crack growth into the material is similar in air and water environments; during the propagation stage, well–defined fatigue striations are observed in both air and water environments. The differing crack morphology of the surface of the specimens tested in low–DO water indicates that the mechanism of crack initiation is different in the low–DO PWR environment than in air or high–DO water. The presence of well–defined striations indicates that mechanical factors are important; environmentally assisted reduction in the fatigue life of austenitic SSs is most likely caused by mechanisms such as H–enhanced crack growth.

Austenitic SSs exposed to LWR environments develop a dark, fine–grained, tightly–adherent, Cr–rich inner layer that forms by solid–state growth, and a cystalline Ni–rich outer layer composed of large– and intermediate–size particles that form by precipitation or deposition from the solution. The characteristics of the surface oxide films can influence the mechanism and kinetics of corrosion processes and thereby influence fatigue crack initiation. Exploratory fatigue tests were conducted on austenitic SS specimens that were preexposed to either low– or high–DO water and then tested in air or water environments in an effort to understand the effects of surface micropits or minor differences in the surface oxide on fatigue crack initiation. The results indicate that the presence of a surface oxide film or any difference in the characteristics of the oxide film have no effect on fatigue crack initiation in austenitic SSs in LWR environments.

## 6.2 Irradiation–Assisted Stress Corrosion Cracking of Austenitic Stainless Steel in BWRs

As neutron fluence increased to ≈2.0 x $10^{21}$ n $cm^{-2}$ (E > 1 MeV), the effect of S on the susceptibility of Types 304 and 304L SS to IASCC was more pronounced than at lower fluence levels. Heats that contain very low concentrations of S of ≤0.002 wt.% were not susceptible to IASCC, whereas heats that contain higher concentrations of S were susceptible.

In spite of high S content, a model austenitic SS alloy that contained a high concentration of Cr (≈21 wt.%) and ≈3 vol.% delta ferrite exhibited excellent resistance to IASCC after irradiation of up to ≈2.0 x $10^{21}$ n $cm^{-2}$ (E > 1 MeV). This finding can be explained well on the basis of the effect of delta ferrite on the distribution of S in the alloy. The solubility limit of S is several times higher in delta ferrite than in the austenitic phase. Therefore, during the process of ingot melting, solidification, and cooling, S atoms will migrate toward and be incorporated in the delta ferrite globules that act as trapping sites for S atoms. As a consequence, the tendency for S to concentrate on austenite grain boundaries is greatly reduced, and the susceptibility to IASCC (in the form of IGSCC along austenite grain boundaries) may be suppressed in irradiated steels that contain delta ferrite even in small volume fraction. However, if the volume fraction of delta ferrite is too great, significant embrittlement of the ferrite phase could lead to unacceptable degradation of the fracture toughness of the irradiated steel.

Fracture toughness J–R curve tests and stress corrosion crack growth tests are also being conducted on commercial heats of austenitic SSs that were irradiated to fluence levels of up to 2 x $10^{21}$ n $cm^{-2}$ (E >1 MeV) at 288°C. The current effort is focused on corrosion fatigue tests on nonirradiated specimens in high–purity water at 289°C to establish the test procedure and conditions that will be used for the tests on irradiated materials. Crack growth tests have been completed on 1/4–T CT specimens of two heats of thermally aged CF8M cast SS and a 50% CW Type 316LN SS in high–purity water at 289°C. The results show good agreement with the data obtained on 1–T CT specimens.

## 6.3 Irradiation–Assisted Cracking of Austenitic Stainless Steel in PWRs

A comprehensive irradiation experiment was initiated to obtain a large number of tensile and disk specimens irradiated under PWR-like conditions at ≈325°C to 5, 10, 20, and 40 dpa. Design of the experiment, fabrication of the specimens, and loading of the capsules, have been accomplished successfully. Irradiation in a fast breeder reactor BOR-60 is currently in progress, and 5-dpa irradiation is expected to be completed by October 2001.

## 6.4 Environmentally Assisted Cracking of Alloys 600 and 690 in LWR Water

The resistance of Ni alloys to environmentally assisted cracking (EAC) in simulated LWR environments is being evaluated. Corrosion fatigue tests are being conducted to establish the effects of alloy chemistry, material heat treatment, cold work, temperature, load ratio R, stress intensity K, and DO level on the CGRs of Ni alloys. The experimental CGRs in high–temperature, high–purity water are compared with CGRs that would be expected in air under the same mechanical loading conditions to obtain a qualitative understanding of the degree and range of conditions that are necessary for significant environmental enhancement in growth rates. The fatigue CGRs of Alloy 600 are enhanced in high–DO water; the

environmental enhancement of growth rates does not appear to depend on either the C content or heat treatment of the material. In high–DO water nearly all of the heats and heat treatment conditions that have been investigated show enhanced growth rates.

During the current reporting period, CGR tests were completed on 30% CW Alloy 600 (Heat NX131031) specimen in high–purity water under various environmental and loading conditions. The growth rates from these tests are compared with data obtained earlier on several heats of Alloy 600 tested in high–DO water under several heat treatment conditions. The environmental enhancement of CGRs of 30% CW Alloy 600 in high–DO water appears to be a factor of 2–3 lower than that observed earlier for MA material. Part of this difference may be due to a change in the CGRs in air for the CW material. Fractographic examination of the specimen indicate a mixed fracture mode, i.e., predominantly intergranular fracture with regions of transgranular fracture.

## References


1. B. F. Langer, "Design of Pressure Vessels for Low–Cycle Fatigue," ASME J. Basic Eng. 84, 389–402 (1962).

2. C. E. Jaske and W. J. O'Donnell, "Fatigue Design Criteria for Pressure Vessel Alloys," Trans. ASME J. Pressure Vessel Technol. 99, 584–592 (1977).

3. O. K. Chopra, "Effects of LWR Coolant Environments on Fatigue Design Curves of Austenitic Stainless Steels," NUREG/CR–5704, ANL–98/31 (1999).

4. Criteria of Section III of the ASME Boiler and Pressure Vessel Code for Nuclear Vessels, The American Society of Mechanical Engineers, New York (1964).

5. O. K. Chopra and W. J. Shack, "Evaluation of Effects of LWR Coolant Environments on Fatigue Life of Carbon and Low–Alloy Steels," in Effects of the Environment on the Initiation of Crack Growth, ASTM STP 1298, W. A. Van Der Sluys, R. S. Piascik, and R. Zawierucha, eds., American Society for Testing and Materials, Philadelphia, pp. 247–266 (1997).

6. O. K. Chopra and W. J. Shack, "Low–Cycle Fatigue of Piping and Pressure Vessel Steels in LWR Environments," Nucl. Eng. Des. 184, 49–76 (1998).

7. O. K. Chopra and W. J. Shack, "Effects of LWR Coolant Environments on Fatigue Design Curves of Carbon and Low–Alloy Steels," NUREG/CR–6583, ANL–97/18 (March 1998).

8. O. K. Chopra and W. J. Shack, "Overview of Fatigue Crack Initiation in Carbon and Low–Alloy Steels in Light Water Reactor Environments," J. Pressure Vessel Technol. 121, 49–60 (1999).

9. M. Higuchi and K. Iida, "Fatigue Strength Correction Factors for Carbon and Low–Alloy Steels in Oxygen–Containing High–Temperature Water," Nucl. Eng. Des. 129, 293–306 (1991).

10. G. Nakao, H. Kanasaki, M. Higuchi, K. Iida, and Y. Asada, "Effects of Temperature and Dissolved Oxygen Content on Fatigue Life of Carbon and Low–Alloy Steels in LWR Water Environment," in Fatigue and Crack Growth: Environmental Effects, Modeling Studies, and Design Considerations, PVP Vol. 306, S. Yukawa, ed., American Society of Mechanical Engineers, New York, pp. 123–128 (1995).

11. M. Higuchi, K. Iida, and Y. Asada, "Effects of Strain Rate Change on Fatigue Life of Carbon Steel in High–Temperature Water," in Effects of the Environment on the Initiation of Crack Growth, ASTM STP 1298, W. A. Van Der Sluys, R. S. Piascik, and R. Zawierucha, eds., American Society for Testing and Materials, Philadelphia, pp. 216–231 (1997).

12. O. K. Chopra and D. J. Gavenda, "Effects of LWR Coolant Environments on Fatigue Lives of Austenitic Stainless Steels," J. Pressure Vessel Technol. 120, 116–121 (1998).

13. O. K. Chopra and J. L. Smith, “Estimation of Fatigue Strain–Life Curves for Austenitic Stainless Steels in Light Water Reactor Environments,” in Fatigue, Environmental Factors, and New Materials, PVP Vol. 374, H. S. Mehta, R. W. Swindeman, J. A. Todd, S. Yukawa, M. Zako, W. H. Bamford, M. Higuchi, E. Jones, H. Nickel, and S. Rahman, eds., American Society of Mechanical Engineers, New York, pp. 249–259 (1998).

14. M. Fujiwara, T. Endo, and H. Kanasaki, “Strain Rate Effects on the Low–Cycle Fatigue Strength of 304 Stainless Steel in High–Temperature Water Environment; Fatigue Life: Analysis and Prediction,” in Proc. Intl. Conf. and Exposition on Fatigue, Corrosion Cracking, Fracture Mechanics, and Failure Analysis, ASM, Metals Park, OH, pp. 309–313 (1986).

15. H. Kanasaki, R. Umehara, H. Mizuta, and T. Suyama, “Fatigue Lives of Stainless Steels in PWR Primary Water,” Trans. 14th Intl. Conf. on Structural Mechanics in Reactor Technology (SMiRT 14), Lyon, France, pp. 473–483 (1997).

16. K. Tsutsumi, H. Kanasaki, T. Umakoshi, T. Nakamura, S. Urata, H. Mizuta, and S. Nomoto, “Fatigue Life Reduction in PWR Water Environment for Stainless Steels,” in Assessment Methodologies for Preventing Failure: Service Experience and Environmental Considerations, PVP Vol. 410-2, R. Mohan, ed., American Society of Mechanical Engineers, New York, pp. 23–34 (2000).

17. K. Tsutsumi, T. Dodo, H. Kanasaki, S. Nomoto, Y. Minami, and T. Nakamura, “Fatigue Behavior of Stainless Steel under Conditions of Changing Strain Rate in PWR Primary Water,” in Pressure Vessel and Piping Codes and Standards, PVP Vol. 419, M. D. Rana, ed., American Society of Mechanical Engineers, New York, pp. 135–141 (2001).

18. M. Higuchi and K. Iida, “Reduction in Low–Cycle Fatigue Life of Austenitic Stainless Steels in High–Temperature Water,” in Pressure Vessel and Piping Codes and Standards, PVP Vol. 353, D. P. Jones, B. R. Newton, W. J. O'Donnell, R. Vecchio, G. A. Antaki, D. Bhavani, N. G. Cofie, and G. L. Hollinger, eds., American Society of Mechanical Engineers, New York, pp. 79–86 (1997).

19. F. P. Ford, “Prediction of Corrosion–Fatigue Initiation in Low–Alloy Steel and Carbon Steel/Water Systems at 288°C,” in Proc. of the Sixth Intl. Symp. on Environmental Degradation of Materials in Nuclear Power Systems-Water Reactors, R. E. Gold and E. P. Simonen, eds., The Minerals, Metals, and Materials Society, Warrendale, PA, pp. 9-17 (1993).

20. C. E. Jaske and W. J. O’Donnell, “Fatigue Design Criteria for Pressure Vessel Alloys,” Trans. ASME J. Pressure Vessel Technol. 99, 584–592 (1977).

21. C. Amzallag, P. Rabbe, G. Gallet, H.–P. Lieurade, “Influence des Conditions de Sollicitation Sur le Comportement en Fatigue Oligocyclique D'aciers Inoxydables Austénitiques,” Memoires Scientifiques Revue Metallurgie, French Metallurgy Society, pp. 161–173 (1978).

22. O. K. Chopra and W. J. Shack, “Environmental Effects on Fatigue Crack Initiation in Piping and Pressure Vessel Steels,” NUREG/CR–6717, ANL–00/27 (May 2001).

23. D. A. Hale, S. A. Wilson, E. Kiss, and A. J. Gianuzzi, “Low Cycle Fatigue Evaluation of Primary Piping Materials in a BWR Environment,” GEAP–20244, U.S. Nuclear Regulatory Commission (Sept. 1977).

24. K. Iida, T. Bannai, M. Higuchi, K. Tsutsumi, and K. Sakaguchi, “Comparison of Japanese MITI Guideline and Other Methods for Evaluation of Environmental Fatigue Life Reduction,” in Pressure Vessel and Piping Codes and Standards, PVP Vol. 419, M. D. Rana, ed., American Society of Mechanical Engineers, New York, pp. 73–81 (2001).

25. A. Hirano, M. Yamamoto, K. Sakaguchi, K. Iida, and T. Shoji, “Effects of Water Flow Rate on Fatigue Life of Carbon Steel in High–Temperature Pure Water Environment,” in Assessment Methodologies for Predicting Failure: Service Experience and Environmental Considerations, PVP Vol. 410–2, R. Mohan, ed., American Society of Mechanical Engineers, New York, pp. 13–18 (2000).

26. E. Lenz, N. Wieling, and H. Muenster, “Influence of Variation of Flow Rates and Temperature on the Cyclic Crack Growth Rate under BWR Conditions,” in Environmental Degradation of Materials in Nuclear Power Systems – Water Reactors, The Metallurgical Society, Warrendale, PA (1988).

27. K. J Miller, “Initiation and Growth Rates of Short Fatigue Cracks,” Fundamentals of Deformation and Fracture, Eshelby Memorial Symposium, Cambridge University Press, Cambridge, U.K., pp. 477–500 (1985).

28. K. Tokaji, T. Ogawa, and S. Osaka, “The Growth of Microstructurally Small Fatigue Cracks in a Ferrite–Pearlite Steel,” Fatigue Fract. Eng. Mater. Struct. 11, 311–342 (1988).

29. D. J. Gavenda, P. R. Luebbers, and O. K. Chopra, “Crack Initiation and Crack Growth Behavior of Carbon and Low–Alloy Steels,” Fatigue and Fracture 1, Vol. 350, S. Rahman, K. K. Yoon, S. Bhandari, R. Warke, and J. M. Bloom, eds., American Society of Mechanical Engineers, New York, pp. 243–255 (1997).

30. K. Obrtlik, J. Polák, M. Hájek, and A. Vasek, “Short Fatigue Crack Behaviour in 316L Stainless Steel,” Intl. J. Fatigue 19, 471–475 (1997).

31. S. G. Sundara Raman, D. Argence, and A. Pineau, “High Temperature Short Fatigue Crack Behaviour in a Stainless Steel,” Fatigue Fract. Eng. Mater. Struct. 20, 1015–1031 (1997).

32. K. J. Miller, “Damage in Fatigue: A New Outlook,” in International Pressure Vessels and Piping Codes and Standards: Volume 1 – Current Applications, PVP Vol. 313–1, K. R. Rao and Y. Asada, eds., American Society of Mechanical Engineers, New York, pp. 191–192 (1995).

33. J. L. Smith, and O. K. Chopra, “Crack Initiation in Smooth Fatigue Specimens of Austenitic Stainless Steel in Light Water Reactor Environments,” in Operations, Applications, and Components – 1999, PVP Vol. 395, I. T. Kisisel, ed., American Society of Mechanical Engineers, New York, pp. 235–242 (1999).

34. C. M. Suh, R. Yuuki, and H. Kitagawa, “Fatigue Microcracks in a Low Carbon Steel,” Fatigue Fract. Eng. Mater. Struct. 8, 193-203 (1985).

35. W. J. Shack and T. F. Kassner, “Review of Environmental Effects on Fatigue Crack Growth of Austenitic Stainless Steels,” NUREG/CR–6176, ANL–94/1 (May 1994).

36. O. K. Chopra, W. K. Soppet, and W. J. Shack, “Effects of Alloy Chemistry, Cold Work, and Water Chemistry on Corrosion Fatigue and Stress Corrosion Cracking of Nickel Alloys and Welds,” NUREG/CR–6721, ANL–01/07 (April 2001).

37. H. Kanasaki, “Fatigue Life of Stainless Steels and Alloy 600 in PWR Environments,” presented at the PVRC Autumn Meeting of the Working Group on S–N Data, October 7–9, 1996, Columbus, OH.

38. J. Keisler, O. K. Chopra, and W. J. Shack, “Fatigue Strain–Life Behavior of Carbon and Low–Alloy Steels, Austenitic Stainless Steels, and Alloy 600 in LWR Environments,” Nucl. Eng. Des. 167, 129–154 (1996).

39. Y. J. Kim, “Characterization of the Oxide Film Formed on Type 316 Stainless Steel in 288°C Water in Cyclic Normal and Hydrogen Water Chemistries,” Corrosion 51 (11), 849–860 (1995).

40. Y. J. Kim, “Analysis of Oxide Film Formed on Type 304 Stainless Steel in 288°C Water Containing Oxygen, Hydrogen, and Hydrogen Peroxide,” Corrosion 55 (1), 81–88 (1999).

41. R. L. Tapping, R. D. Davidson, E. McAlpine, and D. H. Lister, “The Composition and Morphology of Oxide Films Formed on Type 304 Stainless Steel in Lithiated High–Temperature Water,” Corrosion Sci. 26 (8), 563–576 (1986).

42. D. H. Lister, R. D. Davidson, and E. McAlpine, “The Mechanism and Kinetics of Corrosion Product Release from Stainless Steel in Lithiated High–Temperature Water,” Corrosion Sci. 27 (2), 113–140 (1987).

43. M. Da Cunha Belo, M. Walls, N. E. Hakiki, J. Corset, E. Picquenard, G. Sagon, and D. Noel, “Composition, Structure and Properties of the Oxide Films Formed on the Stainless Steel 316L in a Primary Type PWR Environment,” Corrosion Sci. 40 (2/3), 447–463 (1998).

44. B. Stellwag, “The Mechanism of Oxide Film Formation on Austenitic Stainless Steels in High–Temperature Water,” Corrosion Sci. 40 (2/3), 337–370 (1998).

45. T. Nakayama and Y. Oshida, “Identification of the Initial Oxide Films on 18–8 Stainless Steel in High–Temperature Water,” Corrosion NACE 24 (10), 336–337 (1968).

46. M. E. Indig, J. L. Nelson, and G. P. Wozadlo, “Investigation of Protection Potential against IASCC,” in Proc. 5th Intl. Symp. on Environmental Degradation of Materials in Nuclear Power Systems – Water Reactors, D. Cubicciotti, E. P. Simonen, and R. Gold, eds., American Nuclear Society, La Grange Park, IL, pp. 941-947 (1992).

47. M. Kodama, S. Nishimura, J. Morisawa, S. Shima, S. Suzuki, and M. Yamamoto, “Effects of Fluence and Dissolved Oxygen on IASCC in Austenitic Stainless Steels,” in Proc. 5th Intl. Symp. on Environmental Degradation of Materials in Nuclear Power Systems – Water Reactors, D. Cubicciotti, E. P. Simonen, and R. Gold, eds., American Nuclear Society, La Grange Park, IL, pp. 948-954 (1992).

48. H. M. Chung, W. E. Ruther, J. E. Sanecki, A. G. Hins, and T. F. Kassner, “Effects of Water Chemistry on Intergranular Cracking of Irradiated Austenitic Stainless Steels,” in Proc. 7th Intl. Symp. on Environmental Degradation of Materials in Nuclear Power Systems – Water Reactors, G. Airey et al., eds., NACE International, Houston, pp. 1133-1143 (1995).

49. F. Garzarolli, P. Dewes, R. Hahn, and J. L. Nelson, “Deformability of High-Purity Stainless Steels and Ni-Base Alloys in the Core of a PWR,” in Proc. 6th Intl. Symp. on Environmental Degradation of Materials in Nuclear Power Systems – Water Reactors, R. E. Gold and E. P. Simonen, eds., The Minerals, Metals, and Materials Society, Warrendale, PA, pp. 607-613 (1993).

50. H. Kanasaki, T. Okubo, I. Satoh, M. Koyama, T. R. Mager, and R. G. Lott, “Fatigue and Stress Corrosion Cracking Behavior of Irradiated Stainless Steels in PWR Primary Water,” in Proc. 5th Intl. Conf. on Nuclear Engineering, March 26-30, Nice, France (1997).

51. A. J. Jacobs, G. P. Wozadlo, K. Nakata, T. Yoshida, and I. Masaoka, “Radiation Effects on the Stress Corrosion and Other Selected Properties of Type-304 and Type-316 Stainless Steels,” in Proc. 3rd Intl. Symp. Environmental Degradation of Materials in Nuclear Power Systems – Water Reactors, G. J. Theus and J. R. Weeks, eds., The Metallurgical Society, Warrendale, PA, pp. 673-680 (1988).

52. K. Fukuya, K. Nakata, and A. Horie, “An IASCC Study Using High Energy Ion Irradiation,” in Proc. 5th Intl. Symp. on Environmental Degradation of Materials in Nuclear Power Systems – Water Reactors, D. Cubicciotti, E. P. Simonen, and R. Gold, eds., American Nuclear Society, La Grange Park, IL, pp. 814–820 (1992).

53. H. M. Chung, W. E. Ruther, J. E. Sanecki, A. G. Hins, and T. F. Kassner, “Stress Corrosion Cracking Susceptibility of Irradiated Type 304 Stainless Steels,” in Effects of Radiation on Materials: 16th Int. Symp., ASTM STP 1175, A. S. Kumar, D. S. Gelles, R. K. Nanstad, and T. A. Little, eds., American Society for Testing and Materials, Philadelphia, pp. 851-869 (1993).

54. H. M. Chung, W. E. Ruther, J. E. Sanecki, and T. F. Kassner, “Grain-Boundary Microchemistry and Intergranular Cracking of Irradiated Austenitic Stainless Steels,” in Proc. 6th Intl. Symp. on Environmental Degradation of Materials in Nuclear Power Systems – Water Reactors, R. E. Gold and E. P. Simonen, eds., The Minerals, Metals, and Materials Society, Warrendale, PA, pp. 511-519 (1993).

55. J. M. Cookson, D. L. Damcott, G. S. Was, and P. L. Anderson, “The Role of Microchemical and Microstructural Effects in the IASCC of High-Purity Austenitic Stainless Steels,” ibid., pp. 573-580 (1993).

56. M. Kodama, R. Katsura, J. Morisawa, S. Nishimura, S. Suzuki, K. Asano, K. Fukuya, and K. Nakata, “IASCC Susceptibility of Austenitic Stainless Steels Irradiated to High Neutron Fluence,” in Proc. 6th Intl. Symp. on Environmental Degradation of Materials in Nuclear Power Systems – Water Reactors, R. E. Gold and E. P. Simonen, eds., The Minerals, Metals, and Materials Society, Warrendale, PA, pp. 583-588 (1993).

57. S. Kasahara, K. Nakata, K. Fukuya, S. Shima, A. J. Jacobs, G. P. Wozadlo, and S. Suzuki, “The Effects of Minor Elements on IASCC Susceptibility in Austenitic Stainless Steels Irradiated with Neutrons,” in Proc. 6th Intl. Symp. on Environmental Degradation of Materials in Nuclear Power Systems – Water Reactors, R. E. Gold and E. P. Simonen, eds., The Minerals, Metals, and Materials Society, Warrendale, PA, pp. 615-623 (1993).

58. M. Kodama, J. Morisawa, S. Nishimura, K. Asano, S. Shima, and K. Nakata, “Stress Corrosion Cracking and Intergranular Corrosion of Austenitic Stainless Steels Irradiated at 323 K,” J. Nucl. Mater. 212–215, 1509 (1994).

59. T. Tsukada and Y. Miwa, “Stress Corrosion Cracking of Neutron Irradiated Stainless Steels,” in Proc. 7th Int. Symp. on Environmental Degradation of Materials in Nuclear Power Systems – Water Reactors, NACE International, Houston, pp. 1009–1018 (1995).

60. F. Garzarolli, P. Dewes, R. Hahn, and J. L. Nelson, “In-Reactor Testing of IASCC Resistant Stainless Steels,” ibid., 1055–1065 (1995).

61. H. M. Chung, W. E. Ruther, J. E. Sanecki, A. G. Hins, N. J. Zaluzec, and T. F. Kassner, “Irradiation–Assisted Stress Corrosion Cracking of Austenitic Stainless Steels: Recent Progress and New Approaches,” J. Nucl. Mater. 239, 61 (1996).

62. J. M. Cookson, G. S. Was, and P. L. Anderson, “Oxide-Induced Initiation of Stress Corrosion Cracking in Irradiated Stainless Steels,” Corrosion 54, 299 (1998).

63. A. Jenssen and L. G. Ljungberg, “Irradiation Assisted Stress Corrosion Cracking – Postirradiation CERT Tests of Stainless Steels in a BWR Test Loop,” in Proc. 7th Intl. Symp. on Environmental Degradation of Materials in Nuclear Power Systems – Water Reactors, G. Airey et al., eds., NACE International, Houston, 1043–1052 (1995).

64. T. Tsukada, Y. Miwa, H. Nakajima, and T. Kondo, “Effects of Minor Elements on IASCC of Type 316 Model Stainless Steels,” in Proc. 8th Int. Symp. on Environmental Degradation of Materials in Nuclear Power Systems – Water Reactors, Aug. 10-14, 1997, Amelia Island, FL, S. M. Bruemmer, ed., American Nuclear Society, La Grange Park, IL, pp. 795-802 (1997).

65. Y. Tanaka, S. Suzuki, K. Fukuya, H. Sakamoto, M. Kodama, S. Nishimura, K. Nakata, and T. Kato, “IASCC Susceptibility of Type 304, 304L, and 316 Stainless Steels,” in Proc. 8th Int. Symp. on Environmental Degradation of Materials in Nuclear Power Systems – Water Reactors, S. M. Bruemmer, ed., American Nuclear Society, La Grange Park, IL, pp. 803-811 (1997).

66. H. M. Chung, W. E. Ruther, R. V. Strain, W. J. Shack, and T. M. Karlsen, "Irradiation-Assisted Stress Corrosion Cracking of Model Austenitic Stainless Steels," in Proc. 9th Intl. Conf. on Environmental Degradation of Materials in Nuclear Power Systems – Water Reactors, eds. S. Bruemmer, P. Ford, and G. Was, The Minerals, Metals, and Material Society, Warrendale, PA, pp. 931-939 (1999).

67. H. M. Chung, R. V. Strain, and W. J. Shack, "Tensile and Stress Corrosion Cracking Properties of Type 304 Stainless Steel Irradiated to a Very High Dose," Nucl. Eng. Design 208, 221 (2001).

68. H. M. Chung, W. E. Ruther, and R. V. Strain, "Irradiation Assisted Stress Corrosion Cracking of Austenitic SS," in Environmentally Assisted Cracking in Light Water Reactors, Semiannual Report, January 1999-June 1999, NUREG/CR-4667, Vol. 28, ANL-00/7, pp. 13-27 (July 2000).

69. H. M. Chung, W. E. Ruther, and R. V. Strain, "Irradiation Assisted Stress Corrosion Cracking of Austenitic SS," in Environmentally Assisted Cracking in Light Water Reactors, Semiannual Report, July–December 1999, NUREG/CR-4667, Vol. 29, ANL-00/23, pp. 17-29 (Nov. 2000).

70. H. M. Chung, D. Perkins, and R. V. Strain, "Irradiation Assisted Stress Corrosion Cracking of Austenitic SS," in Environmentally Assisted Cracking in Light Water Reactors, Semiannual Report, January 2000-June 2000, NUREG/CR-4667, Vol. 30, ANL-01/08, pp. 17-33 (June 2001).

71. H. M. Chung, R. V. Strain, and R. W. Clarke, "Irradiation Assisted Stress Corrosion Cracking of Austenitic SS," in Environmentally Assisted Cracking in Light Water Reactors, Semiannual Progress Report for January 2000-June 2000, NUREG/CR-4667, Vol. 31, ANL-01/09, pp. 22-32, (April 2002).

72. S. M. Bruemmer et al., "Critical Issue Reviews for the Understanding and Evaluation of Irradiation–Assisted Stress Corrosion Cracking," EPRI TR–107159, Electric Power Research Institute, Palo Alto, CA (1996).

73. P. L. Andresen, F. P. Ford, S. M. Murphy, and J. M. Perks, "State of Knowledge of Radiation Effects on Environmental Cracking in Light Water Reactor Core Materials," in Proc. 4th Int. Conf. on Environmental Degradation of Materials in Nuclear Power Systems – Water Reactors, NACE, pp. 1.83–1.121 (1990).

74. W. J. Mills, "Fracture Toughness of Type 304 and 316 Stainless Steels and their Welds," Intl. Mater. Rev. 42, 45–82 (1997).

75. O. K. Chopra, E. E. Gruber, and W. J. Shack, "Fracture Toughness Characterization of Type 304 Stainless Steel Irradiated in the Halden Reactor," in Proc. 8th Intl. Conference on Nuclear Engineering, 2.02 Aging and Modeling of Component Aging Including Corrosion of Metals and Welds, Paper 8301, American Society of Mechanical Engineers, New York (2000).

76. E. E. Gruber and O. K. Chopra, "Fracture Toughness J–R Test of Austenitic Stainless Steels Irradiated in the Halden Reactor," in Environmentally Assisted Cracking in Light Water Reactors, Semiannual Report, July–December 1999, NUREG/CR-4667, Vol. 29, ANL-00/23, pp. 30–38 (November 2000).

77. E. E. Gruber and O. K. Chopra, "Fracture Toughness J–R Test of Austenitic Stainless Steels Irradiated in the Halden Reactor," in Environmentally Assisted Cracking in Light Water Reactors, Semiannual Report, January 2000 – June 2000, NUREG/CR-4667, Vol. 30, ANL-01/08, pp. 34–41 (June 2001).

78. L. A. James and D. P. Jones, "Fatigue Crack Growth Correlation for Austenitic Stainless Steels in Air," Proc. Conf. on Predictive Capabilities in Environmentally–Assisted Cracking, PVP Vol. 99, R. Rungta, ed., American Society of Mechanical Engineers, New York, pp. 363–414 (1985).

79. W. J. Shack and T. F. Kassner, "Review of Environmental Effects on Fatigue Crack Growth of Austenitic Stainless Steels," NUREG/CR–6176, ANL–94/1 (May 1994).

80. W. E. Ruther, W. K. Soppet, and T. F. Kassner, "Corrosion Fatigue of Alloys 600 and 690 in simulated LWR Environments," NUREG/CR–6383, ANL–95/37 (April 1996).

81. W. E. Ruther, W. K. Soppet, and T. F. Kassner, "Environmentally Assisted Cracking of Alloys 600 and 690 in Simulated LWR Water," in Environmentally Assisted Cracking in Light Water Reactors, Semiannual Report, July 1997–December 1997, NUREG/CR–4667 Vol. 25, ANL–98/18, pp. 42–75 (Sept. 1998).

82. W. E. Ruther, W. K. Soppet, T. F. Kassner, and W. J. Shack, "Environmentally Assisted Cracking of Alloys 600 and 690 in Simulated LWR Water," in Environmentally Assisted Cracking in Light Water Reactors, Semiannual Report, January 1998–July 1998, NUREG/CR–4667 Vol. 26, ANL–98/18, pp. 25–32 (March 1999).

83. W. E. Ruther, W. K. Soppet, T. F. Kassner, and W. J. Shack, "Environmentally Assisted Cracking of Alloys 600 and 690 in Simulated LWR Water," in Environmentally Assisted Cracking in Light Water Reactors, Semiannual Report, July 1998–December 1998, NUREG/CR–4667 Vol. 27, ANL–99/11, pp. 45-54 (October 1999).

84. W. K. Soppet, O. K. Chopra, and W. J. Shack, "Environmentally Assisted Cracking of Alloys 600 and 690 in Simulated LWR Water," in Environmentally Assisted Cracking in Light Water Reactors, Semiannual Report, July 1999–December 1999, NUREG/CR–4667 Vol. 29, ANL–00/23, pp. 39-45 (November 2000).

85. O. K. Chopra, W. K. Soppet, and W. J. Shack, "Effects of Alloy Chemistry, Cold Work, and Water Chemistry on Corrosion Fatigue and Stress Corrosion Cracking of Nickel Alloys and Welds," NUREG/CR–6721, ANL–01/07 (April 2001).

86. W. K. Soppet, O. K. Chopra, and W. J. Shack, "Environmentally Assisted Cracking of Alloys 600 and 690 in Simulated LWR Water," in Environmentally Assisted Cracking in Light Water Reactors, Semiannual Report, July 2000–December 2000, NUREG/CR–4667 Vol. 31, ANL–01/09, pp. 39-48 (April 2002).

87. P. L. Andresen, T. M. Angeliu, L. M. Young, W. R. Catlin, and R. M. Horn, “Mechanisms and Kinetics of SCC in Stainless Steels,” in Proc. 10th Intl. Symp. on Environmental Degradation of Materials in Nuclear Power Systems – Water Reactors, NACE International, Houston (2001).

88. R. B. Rebak, A. R. McIlree, and Szklarska-Smialowska, “Effects of pH and Stress Intensity on Crack Growth Rate in Alloy 600 in Lithiated + Borated Water at High Temperatures,” in Proc. of the 5th Intl. Symp. on Environmental Degradation of Materials in Nuclear Power Systems-Water Reactors, American Nuclear Society, La Grange Park, IL, pp. 511-517 (1991).

89. T. Cassagne and A. Gelpi, “Crack Growth Rate Measurements on Alloy 600 Steam Generator Tubing in Primary and Hydrogenated AVT Water,” in Proc. of the Sixth Intl. Symp. on Environmental Degradation of Materials in Nuclear Power Systems-Water Reactors, R. E. Gold and E. P. Simonen, eds., The Minerals, Metals, and Materials Society, Warrendale, PA, pp. 679-685 (1993).

90. F. Vaillant, C. Amzallag, and J. Champredonde, “Crack Growth Rate Measurements of Alloy 600 Vessel Head Penetrations,” in Proc. of the 8th Intl. Symp. on Environmental Degradation of Materials in Nuclear Power Systems-Water Reactors, S. M. Bruemmer, ed., American Nuclear Society, La Grange Park, IL, pp. 357-365 (1997).